A Thesis Submitted for the Degree of PhD at the University of Warwick

Permanent WRAP URL:

http://wrap.warwick.ac.uk/102002/
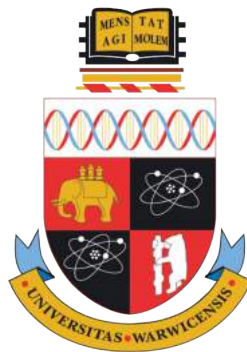
warwick.ac.uk/lib-publications

Development of a new genetically-encoded tag for correlative light electron microscopy

by

Nicholas I. Clarke

Supervisors: Stephen J. Royle and Robert A. Cross

Thesis

Submitted to the University of Warwick

for the degree of

Doctor of Philosophy

March 2018

Contents

List of Figures and Tables

Acknowledgments

First, I would like to acknowledge my supervisor, Steve Royle. For the entirety of this PhD. he has been an excellent advisor and mentor. Thank you for giving me the opportunity to work with you and learn from you. I hope, at least in some part, I can follow in your footsteps.

I would next like to thank everyone who I have had the pleasure of working with over the years. You have all helped me along the way and made this experience one I shall never forget.

A special mention to my parents. I will be forever grateful to you for always being there and giving me the opportunities to be able to pursue my passions in life, including this one.

Finally, and most of all, I thank Erikka Samuel. For everything.

Declarations

This thesis is submitted to the University of Warwick in support of my application for the degree of Doctor of Philosophy. It has been composed by myself and has not been submitted in any previous application for any degree.

The work presented was carried out by the author with exception to the computer code needed for image analysis, which was written by Stephen Royle and described in sections 2.5, 4.6, 4,7 and 4.8.

Abbreviations

3D	Three-dimensional
APX	Ascorbate peroxidase
APEX	Enhanced ascorbate peroxidase
CID	Chemically-Induced dimerization
CLEM	*Correlative* or *correlated* light and electron microscopy
DAB	Diaminobenzidine
DAPI	4',6-diamidino-2-phenylindole
DMEM	Dulbecco's modified eagle's medium
DMT1	Divalent metal ion transferase 1
DNA	Deoxyribonucleic acid
EELS	Electron energy loss spectroscopy
EM	Electron microscopy
Fab	Fragment antigen-binding
FBS	Foetal bovine serum
FKBP	FK506-binding protein
FlAsH	Fluorescein bi-arsenical hairpin-binding
FLM	Florescent light microscopy

FRB	FKBP and rapamycin binding
FTH1	Ferritin heavy polypeptide 1
FTL	Ferritin light chain
GFP	Green fluorescent protein
HIP1R	Huntingtin-interacting protein 1-related protein
HPF	High-pressure freezing
LCa	Clathrin light chain a
LM	Light microscopy
HRP	Horseradish peroxidase
MAO	Monoamine oxidase
MiniSOG	Mini Singlet Oxygen Generator
mTOR	Mammalian target of rapamycin
NA	Numerical aperture
PBS	Phosphate buffered saline
PCR	Polymerase chain reaction
PI(4,5P)$_2$	Phosphatidylinositol 4,5-biphosphate
ReAsH	bi-arsenical hairpin-binding
ROI	Region of interest
RPL5	Ribosomal protein L5
RPL22	Ribosomal protein L22
SD	Standard deviation

SDM	Site-directed mutagenesis
SNR	signal-to-noise ratio
TEM	Transmission electron microscopy
TULIP	Tunable, light-controlled interacting protein

Abstract

To understand cell biology in detail, we must explore subcellular organization in 3D and locate proteins at high resolution. To achieve this, the most popular approach is to use two complimentary imaging techniques; light and electron microscopy. Combining these techniques by *correlative* or *correlated* light and electron microscopy (CLEM) allows cellular events to be observed first by fluorescence microscopy and then the same event can be tracked and visualised at high-resolution using electron microscopy. However, a current challenge is to develop probes to precisely visualize proteins in cells using this method.

This thesis introduces FerriTag, a new genetically-encoded chemically-inducible tag for *correlative* light-electron microscopy. FerriTag is a fluorescent recombinant electron-dense ferritin particle that can specifically label target proteins rapidly and efficiently using rapamycin-induced heterodimerization. The processing protocol described for CLEM is simple yet robust and can potentially be used for tagging any protein-of-interest. FerriTag is easily distinguished from background in electron micrographs due to its high signal to noise ratio and also provides a labelling resolution of 10 ± 5 nm. These qualities make FerriTag an ideal probe for CLEM.

FerriTag can be used to perform contextual nanoscale mapping of protein location relative to a subcellular structure. This was utilised to study the distribution and conformation of huntingtin-interacting protein 1 related (HIP1R) in and around clathrin-coated pits, providing insight to the roles played by HIP1R, clathrin and actin during clathrin-mediated endocytosis.

FerriTag offers great potential for future CLEM applications and will be a useful discovery tool for cell biology.

Introduction

1.1   Correlative Microscopy

Correlative microscopy refers to the combination of more than one imaging modality, enabling the user to acquire complementary data on the same biological sample. Among the many correlative workflows available, the combination of light with electron microscopy is by far the most widely used (Müller-Reichert and Verkade, 2012).

This combination of imaging techniques is referred to as CLEM, for *Correlated Light Electron Microscopy* or *Correlative Light Electron Microscopy*. Ellisman et al. (2012) has tried to define each of these terms based on the precision of correlation. That is, in *Correlated Light Electron Microscopy* the same area within a sample is tracked, whereas in *Correlative Light Electron Microscopy*, the same sample, not exact area, is tracked. Typically the latter, is more user friendly, as it does not require absolute precision in the tracking of an individual subcellular event throughout the entire workflow and instead represents a more global approach to correlation. Whilst this thesis does make a distinction between the two definitions, it is important to realise these terms to define each correlation method is not generally accepted throughout the field and are instead used interchangeably in the literature.

Light microscopy enables the rapid screening and localization of proteins to reveal their dynamics. Though much information regarding intracellular features are hidden if they are unlabeled or fall below the diffraction limit of light. If combined with electron microscopy however, the region of interest can be imaged again, this time at increased resolution where further cellular context is also made available. CLEM

therefore facilitates the ability to determine the underlying structure of rare, transient or previously undescribed subcellular events.

In order to precisely track and correlate these events between each technique, it is essential to use a probe that can be observed for both light and electron microscopy. The sample must then be processed in a way that allows for optimal preservation, structure determination and probe visualization. Finally, correlation between light and electron microscopy is achieved through registration of the same areas or whole samples in complementary images. Typically, these three steps, probes, processing and registration, are necessary for all CLEM experiments.

1.1.1 Probes

The intracellular environment is crowded. Thousands of proteins are constantly involved in a plethora of cellular processes (Fulton, 1982; Hurtley, 2009). This intricate, dynamic yet structured behavior has been termed the 'molecular sociology of the cell' (Robinson et al., 2007; Mahamid et al., 2016). To enable the precise localization of proteins within such a complex and busy environment, highly sensitive probes for CLEM are therefore essential.

Over the past few decades, many advances have been made in the development of probes for CLEM. These can be categorized based on whether they are affinity-based or genetically encoded. Affinity-based label techniques are typically invasive, as they compromise cellular ultrastructure. In contrast genetically encoded tags are non-invasive and are therefore more desirable as samples can be processed in their native state under optimal ultrastructural preservation conditions. A brief overview of probes for CLEM can be found in Table 1.1.

Probe	FLM	EM	Spatial Resolution	HPF	Advantages	Disadvantages	References
Fluoronanogold	++	++	Excellent	Yes	Small size, good penetration into samples.	Typically requires permabilization and weak fixation. Gold/silver enhancement essential.	Takizawa and Robinson, 2000; Olmos *et al.*, 2015; Magidson *et al.*, 2016
Quantum Dots	++	+	Excellent	Yes	Small size, good penetration into samples.	Typically requires permabilization and weak fixation.	Nisman *et al.*, 2004; Giepmans *et al.*, 2005 Deerinck *et al.*, 2007
HRP	-	+	Poor Diffuse	Yes	-	Requires weak fixation.	Porstmann and Kiessig, 1992; Sosinsky *et al.*, 2007
Fluorescent Proteins	+++	-	Good when Correlated	Yes	Bright fluorescence.	Technically difficult to perform correlated procedures.	Ormo *et al.*, 1996; Shaner *et al.*, 2005
Tetracysteine	++	+	Poor Diffuse	No	Very small size.	More efficient DAB conversion probes available. Non-specific background of ligands.	Griffin *et al.*, 1998; Gaietta *et al.*, 2002; Martin *et al.*, 2005
MiniSOG	+	++	Poor Diffuse	No	Efficient photooxidiser.	Weak fluorescence. Staining protocol needs optimizing for each sample.	Shu *et al.*, 2011
APEX	-	++	Poor Diffuse	No	Enzymatic reaction, no need to photooxidise.	Staining needs optimizing for each sample.	Martell *et al.*, 2012 Lam *et al.*, 2014
Metallothionein	-	++	Excellent	Yes	Very small size. Tag density tightly focussed.	Gold very toxic. Reported to not detect some low density proteins.	Diestra *et al.*, 2009; Fernndez de Castro *et al.*, 2014
Ferritin	-	++	Excellent	Yes	Tag density tightly focussed. Iron not toxic at recommended concentration.	Direct fusion mislocalizes some proteins.	Wang *et al.*, 2011

Rows 1–3 are grouped as **Affinity-based Tags**; rows 4–9 are grouped as **Genetically-encoded Tags**.

Table 1.1 Overview of probes for light and electron microscopy. Each probe is scored based on its ability to meet essential CLEM probe criteria; general advantages and disadvantages are highlighted. (-) does not work, (+) poorly suited, (++) well suited, (+++) highly suited.

1.1.1.1   Affinity-based labels

Antibody based recognition probes are still widely used for CLEM (Griffiths and Lucocq, 2014). They take advantage of the high specificity of primary antibodies that are able to bind unique epitopes on a target protein. A secondary antibody, conjugated to a fluorescent moiety with an electron dense tag, can subsequently bind, allowing the visualization of the probe by both light and electron microscopy. The major disadvantage is that weak fixation is usually necessary to ensure suitable preservation and accessibility to epitopes, often resulting in compromised ultrastructure. Additionally pre-embedding protocols require permeabilisation of the cell membrane further compromising cellular ultrastructure and often, intracellular material and membrane constituents can be lost during sample processing. It is therefore imperative to create a careful balance between sample preservation, accessibility and retention of antigenicity. There are however, certain situations in which antibody based probes do not require permeabilisation. These protocols are classed as post-embedding.

Fluoronanogold

Fluoronanogold is a bifunctional immunoprobe consisting of an antibody (Fab′ fragment) conjugated to a fluorophore and small gold cluster, aiding in the accessibility to antigenic sites (Takizawa and Robinson, 2000). However, its size hinders its ability to be visualized by electron microscopy and it therefore requires autometallographic enhancement methods to further develop its size and contrast (Baschong and Stierhof, 1998). In these processes, metal ions in solution are reduced to a zero oxidation state which are then deposited onto Fluoronanogold, which acts as a nucleation site. However this process often results in artefacts due to difficulties in controlling the particle enhancement reaction and forming irregular sized and shaped particles. In addition, enhancement procedures can be liable to autonucleation creating non-specfic background metal deposition. Typically, deposition of gold ions is preferred to silver ions, as it provides better contrast under the electron microscope and it does not get dissolved by strong reducing agents such as osmium tetroxide, which is routinely used for

electron microscopy sample preparation as a fixative and heavy-metal staining agent. Nevertheless, a number of studies have highlighted the advantages of Fluoronanogold in CLEM applications, where these difficulties have been overcome (Takizawa et al., 2015; Olmos et al., 2015; Magidson et al., 2016).

Quantum dots

Quantum dots are small inorganic nanocrystals. They can be finely tuned enabling the ability to emit light over a broad spectrum of wavelengths facilitating imaging of multiple labels simultaneously by light microscopy. Precise correlation can then be achieved with electron microscopy due to their electron dense core (Nisman et al., 2004; Deerinck et al., 2007). However, they are not as electron dense as gold particles and thus can be difficult to see in heavily stained samples. Although mainly used in pre-embedding protocols, quantum dots interestingly have been used to tag intracellular proteins in a non-invasive manner (Giepmans et al., 2005).

1.1.1.2 Genetically encoded tags

Over recent years, there has been much interest in the development of new genetically encoded tags for CLEM. As they can be expressed within the sample itself, they can be processed in a non-invasive manner, enabling optimal preservation of cellular ultrastructure. Additionally, genetically encoded tags are highly specific and support analysis of live cellular dynamics and molecular processes by light microscopy prior to imaging at high resolution using electron microscopy.

1.1.1.2.1 Fluorescent proteins

Fluorescent proteins have revolutionized cell biology. Since the cloning of green fluorescent protein (GFP) there has been an expanding list of new fluorescent proteins that exhibit a broad range of emission wavelengths (Ormö et al., 1996; Shaner et al., 2005). This extensive palette of colors enables imaging of several proteins at once by fluorescent light microscopy.

Fluorescent proteins themselves are not electron dense. They therefore usually require the addition of a specific immunogold particle against the fluorescent protein to be readily observed by electron microscopy (Hodgson et al., 2014). Recent developments in CLEM protocol design however, have enabled the use of a fluorescent protein only, to correlate data. Usually these involve the preservation of fluorescence during processing and then fluorescent imaging can be completed on-section resulting in ultra-precise correlated imaging (Kukulski et al., 2011; Johnson et al., 2015; Avinoam et al., 2015). A recent advance in this area is the osmium-resistant fluorescent protein, Eos4. It has been specifically engineered to withstand heavy fixation and thus aids in ultrastructural preservation and electron microscopy contrast (Paez-Segala et al., 2015).

Advances in super-resolution microscopy have further supported the improvement of correlating light with electron microscopy data (Betzig et al., 2006). However, these techniques still do not provide resolution high enough to distinguish single proteins. Recently, super resolution microscopy has been combined with metal replica sample preparation to correlate proteins at the cell membrane with extremely high resolution (Sochacki et al., 2014, 2017). Though, this approach is particularly invasive, due to sample processing involving the need to produce membrane sheets. Consequently, intracellular constituents are removed, resulting in potential loss of ultrastructural information.

Fluorescent proteins are also extremely useful for correlative experiments to differentiate a specific cell-of-interest within a heterogeneous population. This is particularly useful for the quantitative study of whole cells to examine ultrastructural phenotypes at high resolution (Cheeseman et al., 2013; Hirst et al., 2015)

1.1.1.2.2 DAB-based tags

DAB-based methods are based on the principle of diaminobenzidine (DAB) oxidation by free oxygen radicals. The formation of free radical species can be generated photooxidation or during the enzymatic conversion of peroxidase. This reaction polymerizes

DAB, forming an osmiophilic precipitate that when treated with osmium tetroxide, becomes electron dense and thus easily visible by electron microscopy (Hanker, 1979; Maranto, 1982).

However, the electron density created by all DAB based tags, generates a diffuse signal that also has the possibility to drift into neighboring regions surrounding the tagged protein-of-interest (van Weering et al., 2010; Morphew et al., 2015). This limits to what can be resolved using these techniques and typically single or low-density proteins cannot be readily visualized. Furthermore, these techniques require the user to define the optimum staining conditions to generate sufficient contrast for each experiment to visualize the particular tagged protein-of-interest.

Tetracysteine tags

One of the first genetically encoded tag methodologies for CLEM was based on the ability that a small tetracysteine motif, -Cys-Cys-Xaa-Xaa-Cys-Cys-, could bind bi-arsenical derivatives. Fluorescein bi-arsenical hairpin-binding (FlAsH) and the re-sorufin derivative (ReAsH) are membrane permeable non-fluorescent molecules that upon binding tetracysteine motifs fused to a protein-of-interest, emit green and red fluorescence respectively (Griffin et al., 1998; Gaietta et al., 2002; Martin et al., 2005). The binding of trivalent arsenic atoms to endogenous thiols however is toxic in live cell applications. To overcome this, dithiols are added to minimize these effects.

Although both of these methods are ideally suited for light microscopy, it is only ReAsh that can be readily observed by electron microscopy. ReAsH benefits from also being a singlet oxygen generator and is therefore able to photoconvert DAB to form an electron dense precipitate. During this reaction, careful controls must be put in place to minimize non-specific background staining. This approach was first implemented by Gaietta et al. (2002) and was used to study the dynamics and ultrastructural properties of different ReAsH-labeled connexin43 pools within gap junctions.

A major advantage of this tagging approach is owed to its small size. Typically, most genetically encoded tags are fused to the protein-of-interest at its N or C terminus.

Tetracysteine tags have also shown to possess the ability to be incorporated within the sequence of the protein itself without disrupting normal function. This has been particularly useful for the study of viral function and infectivity(Das et al., 2009). With recent developments into CLEM probe design, there are however more efficient probes available and today, tetracysteine tags are usually not the probe of choice in DAB precipitation based CLEM experiments.

MiniSOG

MiniSOG (for mini Singlet Oxygen Generator) is a flavoprotein engineered from phototropin 2, a photoreceptor from Arabidopsis thaliana (Shu et al., 2011). It is a small non-invasive genetically encoded tag that exhibits internal fluorescence as well as enhanced singlet oxygen generation compared to ReAsH. The combined ability to fluoresce and photooxidise DAB upon blue light irradiation in the presence of oxygen, makes the tag highly desirable. A number of studies have highlighted miniSOGs success for CLEM applications (Cleyrat et al., 2014; Ludwig et al., 2013). Though, due to practical difficulties and diffuse nature of the tag, its popularity as a probe for CLEM is not widespread throughout the field.

Peroxidase based labels

Enzymatic conversion of DAB by horseradish peroxidase (HRP) conjugated to antibodies has been widely used for protein localization in electron microscopy (Porstmann and Kiessig, 1992; Sosinsky et al., 2007). In the presence of hydrogen peroxide, HRP can polymerize DAB into an electron dense precipitate. However, the active site of HRP does not form in reducing environments such as the mammalian cytosol, therefore restricting the ability to label many proteins within the cell.

To overcome the limitations of HRP, Martell et al. (2012) engineered a genetically encoded peroxidase from ascorbate peroxidase (APX) a class I cytosolic plant peroxidase, that remains active in all cellular compartments. Enhanced APX (APEX) catalyzes the hydrogen peroxide dependent polymerization of DAB to form an elec-

tron dense precipitate (Martell et al., 2012). It is noteworthy, enzymatic based DAB precipitation using APEX is much easier than that of photooxidation by miniSOG. More recently, the same group designed APEX2, which works in exactly the same way as APEX, but has significantly improved sensitivity, thereby limiting cellular toxicity (Lam et al., 2014).

APEX has proved its use in an array of protein localization studies for electron microscopy (Wong and Munro, 2014; Shvets et al., 2015; Ariotti et al., 2015). Furthermore, it can also be used as a proximity-based label for proteomic mapping and characterization of close protein-protein interactions in cells (Rhee et al., 2013). Alone however, APEX is not fluorescent and therefore needs to be fused to a fluorescent protein to be visualized by light microscopy for correlative experiments.

1.1.1.2.3 Metal-ligand based tags

The generation of metal clusters within cells to localize proteins using CLEM is highly desirable. Exogenous metal ions bind to the genetically encoded metal ligand based tag enabling the scattering of electrons, thereby generating contrast that is tightly focused for electron microscopy detection. Deposition of metal ions in this way provides a high signal to noise ratio, permitting the tag to be distinguished easily from background noise. In addition, direct detection of metal ions can be determined using electron energy loss spectroscopy (EELS).

Metallothionein

Metallothionein is a small cysteine rich metal-ion chelator that regulates metal homeostasis within the cell. It can bind a variety of metal ions including cadmium, zinc, copper and gold with high affinity and is therefore the ideal candidate protein to be used as a genetically encoded tag for electron microscopy. Diestra et al. 2009 showed by directly fusing metallothionein to a protein-of-interest, the cysteine rich metallothionein in the presence of gold salts can build metal nanoclusters of up to 1 nm in diameter, in bacteria. The cluster provided sufficient density to localize the protein-

of-interest in unstained resin sections (Diestra et al., 2009; Fernndez de Castro et al., 2014). Further work optimized this labeling approach to specifically localize proteins in mammalian cells with high sensitivity and resolution (Risco et al., 2012). Note, for use as a genetically encoded tag for CLEM, metallothionein must also be fused to a fluorescent protein.

However, toxicity of gold salt incubation in cells was a major concern, both for cell viability and ultrastructure preservation. To overcome this, Morphew et al. (2015) further optimized the process in which binding of gold to metallothionein could be achieved. Interestingly, metallothionein retains its ability to bind gold after cryo-immobilization. Therefore gold addition was achieved post processing on-section or during freeze substitution, resulting in electron dense clusters that could be distinguished by electron microscopy (Morphew et al., 2015). It should be noted however, this study highlighted the inability to distinguish low abundant proteins from background noise in electron micrographs. Low staining conditions during processing are also necessary in order to not mask the electron density of the small tag. This limits the user from distinguishing other cellular ultrastructure information.

Bacterial ferritin

Wang et al. developed a genetically encoded tag for cryo-electron tomography based on a iron storage protein called ferritin. Bacterial ferritin (FtnA) was directly fused to a protein-of-interest where it could form a covalently attached electron dense ferritin particles under iron rich conditions in bacterial cells (Wang et al., 2011). The use of iron is preferable to gold as for metallothionein, due to lower toxicity to cells. The authors do highlight however, that certain proteins will mislocalize due to the multi-valent nature of the recombinant ferritin particle. To assess potential mis-localization issues, a fluorescent protein should be tagged to the protein-of-interest also, so it can be visualized first by light microscopy. While used in bacteria, this direct ferritin tagging methodology is technically demanding and has not yet been reported to work in mammalian cells.

1.1.2 Processing

There is no universal protocol to process samples for CLEM. Due to the diverse array of goals made available for CLEM, many different protocols have been developed and the path taken depends on the scientific question being addressed. Furthermore, not all probes are compatible with all processing workflows and therefore the probe used also influences the pathway taken. Collectively, processing of samples for CLEM can be divided into two main categories:

- Pre-embedding CLEM

- Post-embedding CLEM

General workflows for pre-embedding and post-embedding CLEM are shown in Figure 1.1. Correlating data from both modalities in either approach permits the pre-identification of cellular events first by light microscopy, providing an exact focus point for high-resolution electron microscopy acquisition. This ability to pre-identify regions of interest is highly valuable as it minimizes the challenge of locating specific events within such a complex and crowded intracellular environment.
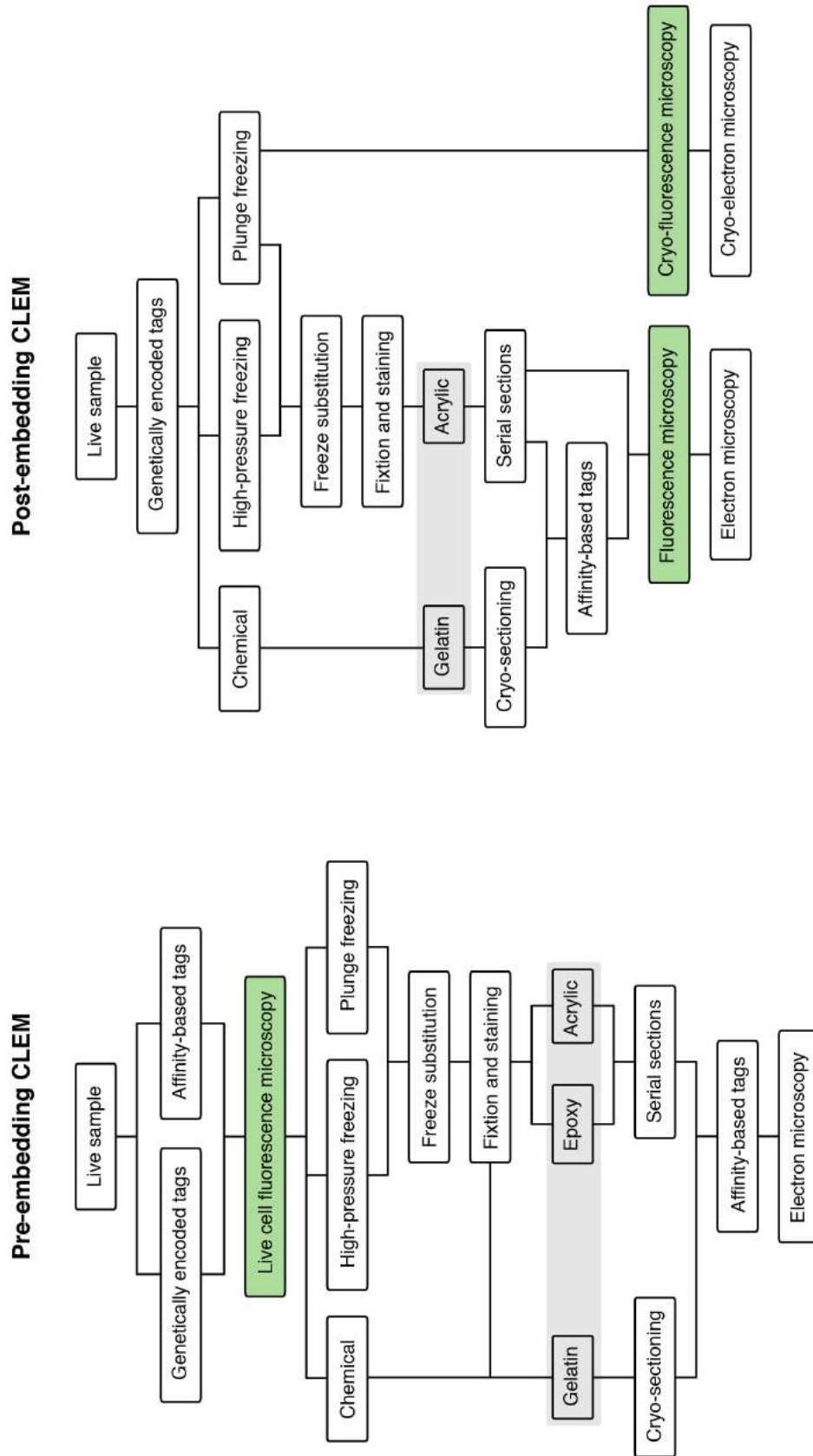
Figure 1.1 Overview of general pre-embedding and post-embedding CLEM workflows. Light microscopy is highlighted in green and embedding procedures in grey, to highlight the point at which imaging is acquired.

Pre-embedding CLEM

Samples being processed for pre-embedding CLEM are imaged by light microscopy prior to fixation and embedding for correlation with electron microscopy. This approach is particularly useful if live cell imaging is required to study dynamic events. Fluorescent proteins guide their identification and enable precise tracking of the event through time. In addition, pre-embedding CLEM is especially useful to discern transiently expressing cells within a heterogeneous population for correlative experiments. Once the position and recording of the event or object has been acquired by light microscopy, samples are immediately fixed and processed for electron microscopy.

Optimal fixation of the sample is key for accurate correlation of the event between imaging modalities. Cryo-immobilization provides superior ultrastructure preservation compared to chemical fixation (Moor and Mühlethaler, 1963). For biological materials, this is routinely achieved by either plunge freezing or high pressure freezing (Medalia et al., 2002; Moor, 1987). Though, the time delay between imaging and fixation may potentially lead to loss of event correlation. However, recent technical advances have been developed to aid in this transition, minimising these concerns. The rapid transfer system (RTS) permits the easy transport and loading of carriers between imaging and loading of samples for high pressure freezing (McDonald et al., 2007). The cryocapsule is a small cell culture tool which was manufactured to fit directly into the high pressure freezer, simplifying sample preparation (Heiligenstein et al., 2014). MAVIS (Microscopy and Vitrification Integrated System) is an integrated system that combines a light microscope with a plunger freezer. Imaging can be performed immediately before freezing, vastly improving time resolution of event correlation down to a time frame of seconds (Koning et al., 2014).

The major drawback to pre-embedding procedures is that resolution along the z-axis is much worse for light microscopy compared to the required thickness of resin sections for electron microscopy. This consequently only produces an approximation-based correlation for correlated techniques.

A distinct advantage of using duel fluorescent and electron dense tags for pre-

embedding CLEM is that precise correlated data is not critical for localizing proteins at the nanoscale. More simple correlative light electron microscopy procedures can be used instead, as tagged proteins can be readily distinguished in both modalities. Though, if a single specific event needs to be tracked, correlated methods are essential.

Post-embedding CLEM

Samples being processed for post-embedding CLEM are imaged by light microscopy following fixation and embedding for correlation with electron microscopy. The fluorescent signal is preserved during sample processing, which enables fluorescent light microscopy to be performed on-section. Electron microscopy is then performed on the same section delivering the most exact correlation possible, due to high z-axis resolution. This approach has been implemented in a number of studies facilitating the localization of proteins with high precision (Kukulski et al., 2011; Johnson et al., 2015; Avinoam et al., 2015).

In order to be compatible for the preservation of fluorescence, certain processing steps must be optimized, including choice of resin, fixation, dehydration and heavy metal staining. Acrylic resins must be used for sample embedding due to their hydrophilic nature and their ability to interact with fluorophores favorably to preserve fluorescence. Chemical fixation for post-embedding CLEM is only possible if weak crosslinking reagents are used, otherwise fluorescent proteins become denatured. Cryo-immobilization by plunge freezing or high-pressure freezing is often used instead. Fluorescent proteins may quench over prolonged exposure to solvent during dehydration in some samples (Peddie et al., 2014). Faster procedures for substitution have been developed to negate these effects (McDonald and Webb, 2011). Additionally, fluorescent proteins can also be quenched due to over-exposure to certain heavy metals. The loss of heavy metals during sample processing results in low contrast and ability to visualize ultrastructure in electron microscopy. Low amounts of uranyl acetate or tannic acid are often used during substitution, resulting in fluorescence preservation and electron contrast (Kukulski et al., 2011; Johnson et al., 2015). Furthermore, osmium-resistant

fluorescent proteins have recently been engineered to aid in this problem (Paez-Segala et al., 2015).

An alternative approach for post-embedding CLEM using chemical fixation uses cryo-sectioning of frozen embedded gelatin samples (Tokuyasu, 1973). Here, thawed cryo-sections are imaged first by fluorescent light microscopy before being imaged at high resolution by electron microscopy. Due to mild fixation, antigenicity is preserved remarkably well and therefore immunogold procedures are often performed inline with fluorescent light microscopy correlation for ultra-precise protein localization (Hodgson et al., 2014).

1.1.3   Retracing and Registration

The final step in the CLEM workflow involves reliable and precise retracing and registration between light and electron microscopy data. Both *correlative* and *correlated* procedures absolutely require accurate retracing of the sample being imaged. It is only correlated workflows however that involve registration, to be able to track exact regions within a sample. Whist the process of registering light with electron micrographs for *correlated* experiments is challenging, software tools such as TrakEM2 (Cardona et al., 2012) and ec-CLEM (Paul-Gilloteaux et al., 2017) can assist greatly. The way in which retracing and registration is achieved depends on whether pre or post-embedding CLEM is performed.

Pre-embedding procedures use specific sample holders, finder cell-culture grids, laser marks or pattern recognition to accurately track each sample throughout the entire CLEM workflow (de Boer et al., 2015). To perform *correlated* registration, serial stacks are first acquired using fluorescence light microscopy. The slice that best matches the electron micrograph is used to correlate and overlay both images. This typically results in inaccurate correlation due to limitations in z-axis resolution. Moreover, shrinkage during sample processing, sample distortion from resin sectioning and small time delays during fixation further restrict the ability to accurately correlate data.

Re-tracing for post-embedding CLEM involves picking up sections onto finder grids.

The finder grid is visible by both light and electron microscopy and therefore, fluorescent regions of interest can be retraced during the transfer of grids between both imaging modalities. Post-embedding registration is far more precise than pre-embedding techniques as light microscopy and electron microscopy is performed on the same section, thereby overcoming z-axis resolution limitations. Fiducial markers aid in precise registration and correlation, as they are visible by both light and electron microscopy (Kukulski et al., 2011). They therefore act as position co-ordinates to guide the user towards the exact region of interest when at high resolution.

Recent advances in technology have further improved the ability to precisely correlate data for post-embedding CLEM. Integrated light and electron microscopes perform imaging sequentially without the need to move the sample (Peddie et al., 2014). This enables precise correlation through the automated overlay of both images without the need for finder grids or fiducial markers. Additionally, cryo-fluorescence stages allow fluorescent light microscopy to be performed on whole frozen samples (Schorb et al., 2017). As the sample is then immediately imaged by cryo-electron microscopy it makes retracing and registration particularly user-friendly.

1.2 Cell Biology

1.2.1 Clathrin-mediated endocytosis

Endocytosis describes the process by which vesicles are produced from the plasma membrane, facilitating the internalisation of extracellular molecules, plasma membrane proteins and lipids into the cell. Multiple endocytic trafficking pathways exist and can be broadly categorized by whether they are mediated by clathrin or not (Doherty and McMahon, 2009).

Clathrin is a triskelion-shaped scaffold protein, composed of three heavy and three light chains. As well as playing a fundamental role in membrane trafficking it also moonlights in mitosis, aiding in the stabilization of microtubules in kinetochore fibres (Royle, 2013). Clathrin-coated structures where first observed in mosquito embryos by electron microscopy and have been of great interest for decades (Roth and Porter, 1964). Yet, the mechanisms by which clathrin-mediated endocytosis operates and how the process is regulated are still being unraveled. In brief, a complex network of proteins coordinates the timely progression through four defined stages, illustrated in Figure 1.2. This begins with event initiation and is followed by vesicle maturation, scission and finally uncoating. A high-resolution study has imaged these key steps using high-precision *correlated* light electron microscopy and shown how the plasma membrane is remodelled during the entire process (Kukulski et al., 2012). Briefly, *Saccharomyces cerevisiae* strains expressing various fluorescently tagged clathrin-mediated endocytic proteins were high-pressure frozen and prepared for post-embedding CLEM by preserving fluorescence in-resin. Each strain was then imaged by light microscopy and the fluorescent signal was tracked to the electron microscope where the ultrastructure was observed at high resolution. This work highlights the power of CLEM for the study of cell biology and specifically clathrin-mediated endocytosis.

A well studied example of a cargo molecule that is constitutively internalised in this way, is an iron-binding protein called transferrin. Iron-bound transferrin binds to its receptor on the cell surface, where it is rapidly internalized by invagination

of clathrin-coated pits. Inside the cell, it is trafficked to early endosomes, releases bound iron and is then recycled back to the cell surface. Uptake of transferrin takes around 10 minutes and is recycled out by 15 minutes (Motley et al., 2003). The uptake of fluorescently labelled transferrin is widely used to study normal clathrin-mediated endocytic function.
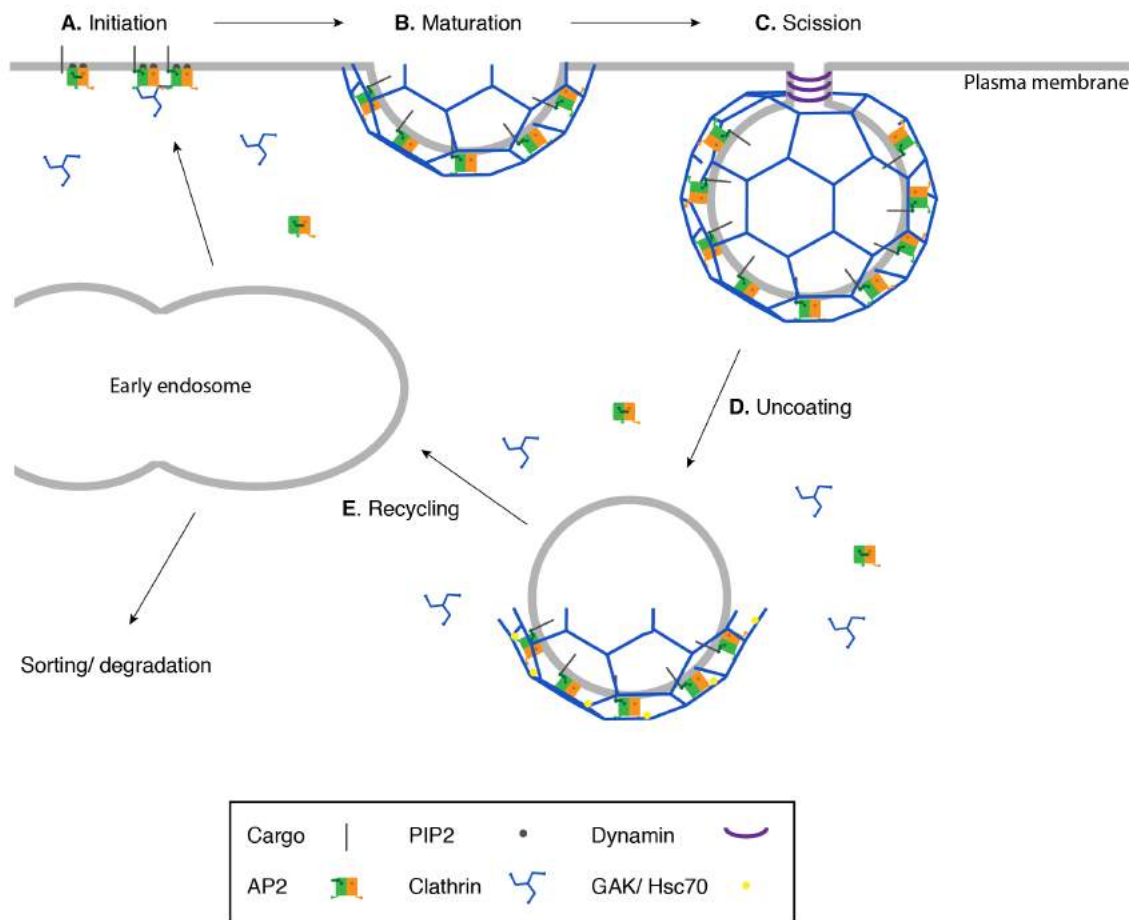
Figure 1.2 Schematic diagram of clathrin mediated endocytosis.
(A) AP-2 binds PI(4,5)P$_2$ at the plasma membrane followed by recruitment of clathrin.
(B) The clathrin coat assembles during invagination of the vesicle.
(C) Dynamin is recruted to the neck permitting scission of the clathrin-coated vesicle.
(D) Once, the vesicle has pinched off from the plasma membrane, the clathrin coat is dissasembled, aided by GAK/Hsc70.
(E) Uncoated vesicles fuse with early endosomes where cargo is sorted ether for degradation or recycled to the plasma membrane.

Initiation

Due to the complexity of the molecular machinery involved, a unified model for initiation has not emerged (Godlee and Kaksonen, 2013). Though, essential adaptor and accessory proteins clearly have fundamental roles in the timely order of protein assembly during initiation.

While clathrin is the main component of the endocytic machinery, it is unable to directly bind to the plasma membrane or to cargo. To initiate clathrin-mediated endocytosis therefore, adaptor proteins that bind plasma membrane and cargo are needed to provide the necessary link to which clathrin can subsequently bind. Among the first to arrive is AP-2 (Loerke et al., 2011). AP-2 can bind specifically to various partners including clathrin, endocytic motifs present on cargo receptors and the membrane-specific lipid phosphatidylinositol 4,5-biphosphate ($PI(4,5P)_2$). Localization of AP-2 to the membrane is thought to be PIP2 dependent. It is this recruitment of AP-2 guided by $PI(4,5)P_2$ localization at the plasma membrane that is generally viewed as the essential initiator sequence for clathrin-mediated endocytosis (Kelly et al., 2011).

Furthermore, there is an emerging role of the location site playing a role in clathrin-coated pit initiation. While the degree and significance of spatially regulating endocytosis at specific sites remains unclear, several studies have observed that multiple nucleations can occur at the same location (Nunez et al., 2011; Li et al., 2015). These highly productive areas of initiation have been termed hotspots (Keen et al., 1999). Recent work using super-resolution microscopy has shown that at a single hotspot, in 3.6% of cases, more than 5 nucleation events can occur (Li et al., 2015). Whilst initiation is not solely restricted to hotspot locations, they do provide a mechanism to spatially organize clathrin-mediated endocytosis at certain locations within the cell.

Maturation

Following initiation, the plasma membrane must invaginate and continue to assemble the clathrin coat, to eventually form a vesicle. Whether this transition occurs by clathrin polymerization during membrane invagination or by membrane reshaping

where clathrin has already recruited remains controversial (Dannhauser et al., 2015; Heuser, 1980). Though clathrin has been shown to possess an increased affinity for curved membranes (Pucadyil and Holkar, 2016), substantial evidence has been generated that supports the latter model. Avinoam *et al.* used correlated light electron microscopy to image endocytic sites and determine clathrin coats and membrane profiles during invagination. Interestingly, the clathrin coat surface remained almost constant throughout, which would not occur if clathrin polymerization were to occur. The curvature of the clathrin coat also increased as invagination proceeded, further supporting the latter model.

Several endocytic accessory proteins have demonstrated membrane-bending properties. The PIP2 binding proteins epsin, CALM and amphiphysin all contain amphiphatic helices that insert into the plasma membrane inducing positive curvature towards the insertion. This facilitates maturation of early clathrin-coated initiation sites into a deeply invaginated pit (McMahon and Boucrot, 2011).

Actin recruitment at endocytic sites occurs early during invagination, generating a propulsive force that promotes vesicle maturation (Kaksonen et al., 2006). Actin and actin-associated factors are recruited and enriched in more than 50% of clathrin-mediated endocytosis events and disruption to the actin cytoskeleton leads to impaired maturation efficiency as well as distinct morphological changes to the neck of deeply invaginated pits in mammalian cells (Taylor et al., 2011, 2012). Furthermore, a positive correlation between clathrin coated pit lifetime and amount of actin recruited exists (Grassart et al., 2014). Although, actin is not essential for clathrin-mediated endocytosis in cultured mammalian cells, there is evidence that actin recruitment is necessary when membrane tension is high (Boulant et al., 2011). Consistent with this, actin is essential for endocytosis in yeast (Engqvist-Goldstein and Drubin, 2003). As their membrane tension is high, a greater force needs to be generated by actin polymerization to internalize membranes during endocytosis.

Actin coupling to clathrin-coated pits is regulated by HIP1R. HIP1R has the ability to bind membranes, clathrin light chain and actin and is found in more than 90%

of clathrin-mediated endocytic events (Taylor et al., 2011). It can also exist in two confirmations: extended and kinked (Engqvist-Goldstein et al., 2001; Wilbur et al., 2008). Though, how HIP1R links the clathrin machinery to actin during maturation of the vesicle is not particularly well understood. Three models have been proposed, outlined in Figure 1.3. First, immunogold electron microscopy on unroofed cells suggested HIP1R is restricted to the rim of clathrin-coated pits (Engqvist-Goldstein et al., 2001). Second, HIP1R was proposed to bind the clathrin coat exclusively towards the vesicle neck providing an anchor site to which actin can bind (Le Clainche et al., 2007). Third HIP1R was predicted to be distributed throughout the pit and distal regions of the membrane where it could adopt different confirmations (Wilbur et al., 2008). The conformational change enabled different actin binding properties. In its extended state, HIP1R can bind actin with much higher affinity than when found in its closed confirmation. Extended HIP1R was predicted to bind the plasma membrane and specifically localize at the neck of a budding vesicle while its closed weaker state bound clathrin and decorates the pit itself. Although all three models highlight key findings regarding HIP1R structure and localization, only the second model remains feasible for efficient vesicle production as it is the only model to show actin being linked to clathrin. Without this, sufficient force to internalize clathrin-coated vesicles by actin polymerization is not achieved. However, their work did not include ultrastructural localization of HIP1R. So we do not know how HIP1R structure relates to its function and in turn, how this is related to ultrastructure.
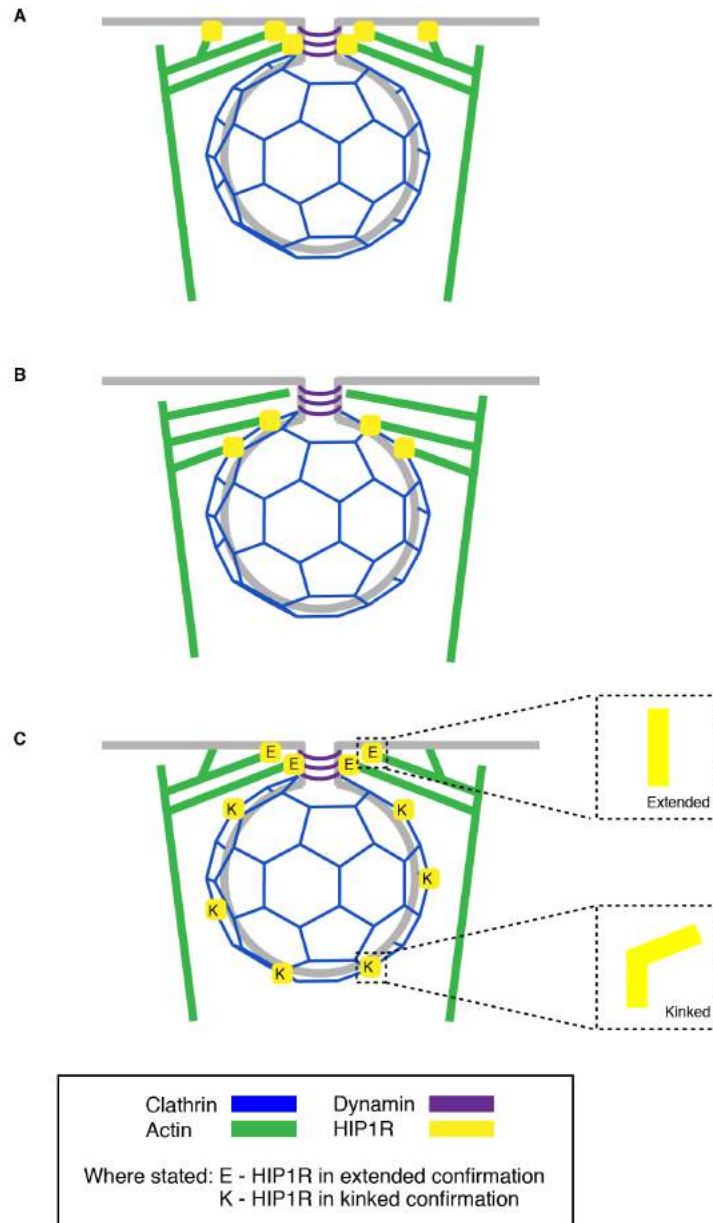
Figure 1.3 Current models for HIP1R localization during clathrin mediated endocytosis.
(A) Model outlined by Engqvist-Goldstein et al., (2001). HIP1R is restricted to the rim of clathrin-coated pits.
(B) Model outlined by Le Clainche et al., (2007). HIP1R binds the clathrin coat exclusively towards the vesicle neck providing an anchor site to which actin can bind.
(C) Model outlined by Wilbur et al., (2008). HIP1R exists in two states, extended (E) or kinked (K). In its extended state, HIP1R binds actin at the neck with much higher affinity than when found in its shorter, kinked confirmation around the rim of clathrin-coated pits.

38

Scission

Scission of the mature clathrin-coated vesicle is dependent on the mechanochemical enzyme dynamin. Dynamin is a large GTPase that assembles into helical polymers around the neck of deeply invaginated pits. Dynamin is recruited to the neck by BAR domain-containing proteins, such as amohiphysin and endophilin. These proteins have a strong binding preference for curved membranes and also contain amphipathic helices that may also help to bend the membrane, facilitating scission (Daumke et al., 2014). Constriction of the dynamin ring is induced by GTP-hydrolysis promoting a conformational change that results in vesicle fission (Srinivasan et al., 2016). Without dynamin, vesicle formation is arrested (Ferguson and De Camilli, 2012).

Vesicle uncoating

The final step involves the uncoating of clathrin from vesicles. This disassembly from lattice to triskelia is achieved by the recruitment of auxillin (or GAK in non-neuronal cells). Following scission, auxillin binds the clathrin coat, specifically localizing beneath the hub of neighbouring triskelia. This enables the heat shock protein 70 (Hsc70) to subsequently bind whereby uncoating is then initiated (Greener et al., 2000).

Furthemore, auxillin can bind specific membrane lipids that have been synthesized from PIP2 by the phosphatase synaptojanin. Changing the phosphoinositide composition of clathrin-coated vesicles in this way controls the timing of auxillin binding restricting its arrival to peak dynamin activity and thus assists uncoating (Guan et al., 2010). Following uncoating, the clathrin machinery is released into the cytoplasm where it can be reused in other rounds of clathrin-coated vesicle formation.

1.2.2 Chemically-induced dimerization

Chemically-Induced dimerization (CID) is a powerful tool for controlling protein function in cell biology. It has been widely used in the study of clathrin-mediated endocytosis, to force protein-protein interaction (Zoncu et al., 2007; Nakatsu et al., 2010; Brach et al., 2014; Manna et al., 2015) or relocate target proteins to specific cellular compartments (Robinson et al., 2010; Willox and Royle, 2012; Hirst et al., 2015).

Conditional regulation of two proteins is induced by small molecules that promote their association into a high-affinity interaction. The first naturally occurring CID system was described by Liu et al. 1991, in which the immunospressant drug FK506 was shown to simultaneously bind FKBP12 and calcineurin, resulting in the inhibition of T-cell receptor-mediated signalling. Building on this work, a semi-synthetic ligand named FK1012, formed by linking two FK506 molecules, was prepared that could dimerize FKBP12, without binding calcineurin (Spencer et al., 1993). Whilst FK1012 was the first CID system to induce the close association of two proteins, the system is limited to proteins dependent on homodimerization. Several years later, the synthesis of heterodimerizing molecules capable of specifically dimerizing two different proteins were reported (Belshaw et al., 1996; Licitra and Liu, 1996; Rivera et al., 1996). Among these, was the small molecule, rapamycin.

Rapamycin is the most widely used chemical heterodimerizer in cell biology (Figure 1.4A) (Putyrski and Schultz, 2012). Rapamycin first binds the FKBP domain of FKBP12. This complex then binds and inhibits the FRB (FKBP and rapamycin-binding) domain of the kinase Target of Rapamycin (mTOR) with extremely high affinity (2 nM) (Figure 1.4A). In cells, two proteins genetically fused to FKBP and FRB can be inducibly dimerized upon the addition of rapamycin, resulting in them being brought within close proximity with one another. Due to the small molecular size of rapamycin, it readily enters cells inducing the heterodimerization within a timescale of seconds.

A potential limitation of using rapamycin to induce heterodimerization, is its natural inhibitory effect on mTOR. Over substantial time periods, rapamycin has been

shown to inhibit downstream mTOR signaling pathways that regulate cell metabolism, growth, proliferation and survival (Laplante and Sabatini, 2009). Because of theses effects, non-immunosuppressive rapamycin analogs (Rapalogs) have been developed. The most widely used, AP21967 is able to specifically bind a mutant FRB domain (FRB T2098L) but is too bulky to bind the FRB domain of endogenous mTOR (Figure 1.4 B) (Putyrski and Schultz, 2012).

Recent work has introduced a new promising CID system using the plant hormone Gibberellin (Miyamoto et al., 2012). Here, Miyamoto *et al.* synthesised a modified form of Gibberellin, GA3-AM, which first binds it receptor gibberellin insensitive dwarf1 (GID1). The GA3-AM-GID1 complex can then dimerize with gibberellin insensitive (GAI) (Figure 1.4 B). Whilst the kinetics of this system to reach maximum dimerization does not quite act as fast as rapamycin-induced dimerization (approximately 60 seconds for GA3-AM, compared to less than 10 seconds for rapamycin), it is still useful for the effective perturbation of many cellular processes.
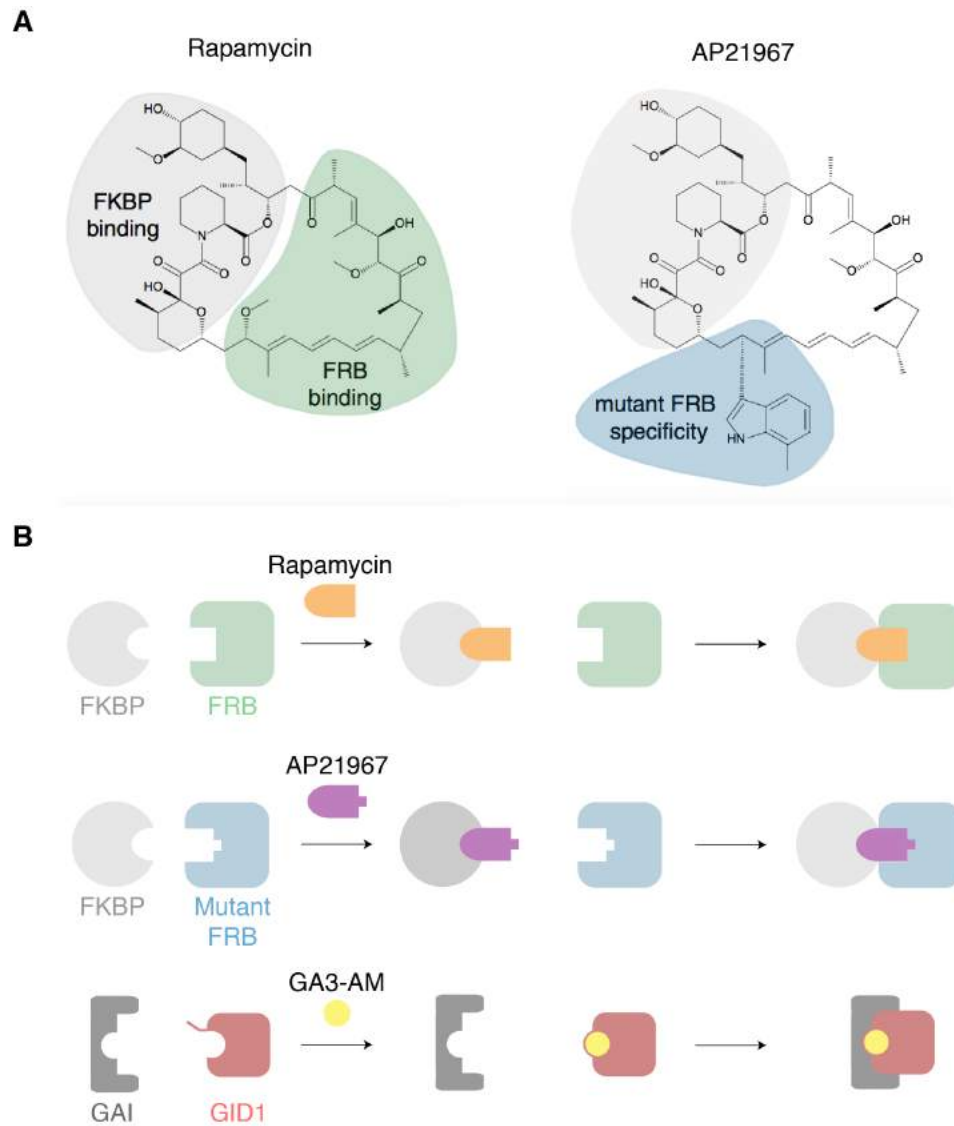
Figure 1.4. Protein dimerization systems.
A) Chemical structures of rapamycin and its most commonly used analog AP21967. Binding surfaces to FKBP, FRB and mutant FRB are highlighted. B) Rapamycin or AP21967 first binds FKBP and the complex then binds FRB (or mTOR). The bulky adduct of AP21967 ensures it cannot bind endogenous FRB, making it specific to mutant FRB (T2098L). Modified gibberellin (GA3-AM) first binds gibberellin insensitive dwarf1 (GID1) inducing a confirmational change, allowing the GA3-AM-GID1 complex to dimerize with gibberellin insensitive (GAI).

1.3 Motivation for this project

Combined together, light and electron microscopy can provide unprecedented information about the complex network of proteins involved in the many processes within the cell. However, there are drawbacks in current probes available to perform highly accurate correlation down to single protein localization. The ideal probe for CLEM must therefore meet these essential criteria:

- It should be genetically encoded and thus non-invasive.

- It should be non-toxic and non-disruptive to any cellular processes.

- The tag must be fluorescent so it is visible by light microscopy and also electron-dense so it can be distinguished again by electron microscopy.

- The electron density must be tightly focused and have good signal:noise ratio so it can be readily distinguished from background in electron micrographs.

- The methodology should be robust, reliable and not dependent on user optimizing the staining conditions for each protein-of-interest.

- It should be compatible with high pressure freezing and thus allow samples to be optimally preserved for imaging.

In order to study intracellular proteins involved in crowded and complex processes such as clathrin-mediated endocytosis, it is fundamental that a new probe should be developed that satisfies all these criteria.

1.4   Published work

The work presented in this thesis regarding the development of a new genetically encoded tag has been preprinted (Clarke and Royle, 2016) and is currently under review at a journal.

In addition to this, I have also collaborated on several other papers which have now been published (Auckland et al., 2017; Nixon et al., 2017; Wood et al., 2017). My contribution to these are summarized in the appendices.

Materials and Methods

2.1 Molecular biology

RPL5-mCherry-FRB was made by amplifying human ribosomal protein L5 (RPL5, IMAGE clone 5736022) by PCR and inserting into pMito-mCherry-FRB (made available from previous work; see Cheeseman et al. 2013) via *Eco*RI-*Age*I. RPL22-mCherry-FRB was made by amplifying human ribosomal protein L22 (RPL22, IMAGE clone 5109124) by PCR and inserting into pMito-mCherry-FRB via *Eco*RI-*Bam*HI. FRB-mCherry-FTH1 was made by amplifying human ferritin heavy polypeptide 1 (FTH1, IMAGE clone: 3459353) by PCR and inserting into pFRB-mCherry via *Xho*I-*Eco*RI. The mitochondrial target sequence TOM70p from pMito-mCherry-FRB was subcloned into FRB-mCherry-FTH1 via *Bsr*GI-*Xba*I, to make pMito-mCherry-FTH1. To make FTL only, human ferritin light chain (FTL, IMAGE clone 2905327) was amplified by PCR and inserted into pEGFP-C1, removing EGFP, via *Age*I-*Xho*I. GFP-FKBP-LCa was available from previous work (Cheeseman et al., 2013). FKBP-GFP-Myc-MAO was a kind gift from Sean Munro (MRC-LMB, Cambridge; see Wong and Munro 2014). FRB-mCherry-FTH1 (T2098L) was made using a site-directed mutagenesis (SDM) method based on the QuikChange protocol (Wang and Malcolm, 1999) to introduce a T2098L mutation. CD8-GFP-FKBP was made by amplifying CD8α from CD8-mCherry-FRB (made available from previous work; see Wood et al. 2016) by PCR and inserting into pEGFP-FKBP-N1 via *Nhe*I-*Age*I. HIP1R-GFP-FKBP was made by amplifying HIP1R from Addgene plasmid 27700 by PCR and inserting into pEGFP-FKBP-N1 via *Xho*I-*Age*I.

2.2 Cell biology

HeLa cells (HPA/ECACC #93021013) were cultured in Dulbecco's Modified Eagle's Medium (DMEM, Gibco) supplemented with 10% fetal bovine serum (FBS) and 100 U/ml penicillin/streptomycin at 37 °C and 5% CO_2. Cells would reach 80-100% confluency before they where passaged. Cells where kept no longer than a total of 25 passages following initial thawing. Cells grown in iron-rich conditions were supplemented with $FeSO_4 \cdot 7\,H_2O$ to a final concentration of $1\,\text{mM}$ in full DMEM, 16 hours prior to imaging.

Transfection was performed using Genejuice (Novagen). Cells seeded in 3.5 cm wells where grown to around 70% confluency, 24 hours prior to transfection. To perform transfection, $3\,\text{µl}$ of Genejuice was added to $100\,\text{µl}$ of DMEM without additives and incubated at room temperature for 5 minutes. A total of $1.5\,\text{µg}$ of DNA was added to the Genejuice/ DMEM mixture and incubated for a further 15 minutes at room temperature. The DNA/ Genejuice/ DMEM mixture is then added to each well containing full DMEM and left for 12-16 hours overnight. Transfection media was washed off the following morning and replaced with full DMEM and cells were imaged or fixed 2 days following transfection. The total amount of DNA for each plasmid transfected in FerriTag experiments, was $750\,\text{ng}$ of the GFP-FKBP tagged protein-of-interest and $750\,\text{ng}$ FerriTag (mixture of FTL only vector and FRB-mCherry-FTH1). The ratio of transfected FerriTag plasmids is stated for each experiment. Optimal FerriTag expression is performed by transfecting $600\,\text{ng}$ FTL only vector and $150\,\text{ng}$ of FRB-mCherry-FTH1 (i.e. 4:1).

Cell viability was performed using the trypan blue exclusion assay. HeLa cells were grown in 12-well plates and incubated in full DMEM containing different concentrations of $FeSO_4 \cdot 7\,H_2O$. At certain time points, cells where detached from each well using trypsin and resuspended in full DMEM. A 1:1 dilution of cell suspension with 0.4% Trypan Blue solution (ThermoFisher) was prepared for each suspension. Following brief incubation at room temperature, a total of 500 cells for each condition where

counted under a microscope. Non-viable cells appear blue and viable cells are unstained (clear).

2.3 Light microscopy

Fixed cell experiments were performed in transiently transfect HeLa cells attached to glass coverslips. Cells were fixed with 3% paraformaldehyde, 4% sucrose in PBS at 37 °C, washed in PBS and mounted in Mowiol containing DAPI. Imaging was performed on a Nikon Ti epifluorescence microscope with standard filtersets, equipped with a heated environmental chamber (OKOlab) and CoolSnap MYO camera (Photometrics) using NIS elements AR software.

Live-cell microscopy of FerriTag kinetics was performed in HeLa cells plated on fluorodishes (WPI) expressing GFP-FKBP-LCa and either FerriTag (FTL:FRB-mCherry-FTH1, 4:1) or rapalog compatible FerriTag (FTL:FRB-mCherry-FTH1 T2098L, 4:1). Cells were kept in Leibovitz L-15 CO_2-independent medium (Sigma) supplemented with 10% FBS and kept at 37 °C during acquisition. Imaging was captured on a spinning disc confocal microscope (Ultraview Vox, Perkin Elmer) with a 100x 1.4 NA oil-immersion objective taking frames every 2 seconds using a dual camera system (Hamamatsu ORCA-R2) after excitation with 488 nm and 561 nm lasers.

Transferrin uptake analysis was performed in HeLa cells cultured on glass coverslips, expressing GFP-FKBP-LCa and FerriTag (FTL only: FRB-mcherry-FTH1, 1:4). 48 hours post-transfection, cells were serum-starved for 30 minutes in serum-free DMEM and then rapamycin was added in test conditions to induce FerriTagging. Control conditions had no rapamycin added. Hypertonic sucrose solution (0.45M in serum-free DMEM) was added 15 minutes into serum starvation. Following 2 minutes rapamycin addition, Alexa647-conjugated transferrin (Invitrogen) was added directly to all cells for 10 minutes. Cells were washed in warm PBS and fixed in 3% paraformaldehyde + 4% sucrose for 15 minutes. Coverslips were washed in PBS and dH_2O before mounting onto glass slides with Mowiol containing DAPI.

In all experiments rapamycin (Alfa Aesar) was added by pipetting in a concentrated

solution in appropriate media at $37\,^{\circ}C$ to a final concentration of $200\,nM$. The same approach was used to add AP21967 at a final concentration of $1\,\mu M$.

2.4   Correlative light electron microscopy

HeLa cells transfected with a GFP-FKBP tagged protein-of-interest and FerriTag (FTL: FRB-mCherry-FTH1. 4:1), were plated onto gridded glass culture dishes (P35G-1.5-14-CGRD, MatTek Corporation, Ashland, MA, USA). Iron-rich media was added 16 hours prior to imaging (with the exception of the experiment shown in figure 4.4 C). Light microscopy was performed on a Nikon Ti epifluorescence microscope (described above; see 2.3. Cells were kept at $37\,^{\circ}C$ in Leibovitz L-15 CO_2-independent medium supplemented with 10% FBS during imaging. Using the photo-etched coordinates on each grid, the location of each cell-of-interest was recorded using brightfield illumination at 20x for future reference. The same cell was then relocated and fluorescent live cell imaging was then acquired at 100x. During imaging, unless otherwise stated, rapamycin was added and once sufficient FerriTagging had been achieved, cells were immediately fixed in 3% glutaraldehyde, 0.5% paraformaldehyde in $0.05\,M$ phosphate buffer pH 7.4 for $1\,h$. Following fixation, free aldehydes were quenched in $50\,mM$ glycine solution and cells washed several times in $0.05\,M$ phosphate buffer. Cells were post-fixed in 1% osmium tetroxide (Agar) for $1\,h$, washed in distilled water and then dehydrated through an ascending series of ethanol (30, 50, 70, 80, 90, 100, 100%. 5 minutes each). Cells were then infiltrated in epoxy resin (TAAB) using a 2:1 ratio of ethanol:resin for 30 minutes, 1:2 ratio of ethanol:resin for 30 minutes and then resin only for a further 60 minutes. Fresh full resin was then added and a gelatin capsule containing resin was placed over the grid containing the cell-of-interest. Resin was then left to polymerize at $60\,^{\circ}C$ for 48 hours. Coverslips attached to the polymerized resin block were removed by briefly plunging into liquid nitrogen. The cell-of-interest was then located by correlating grid coordinates imprinted on the resin block with previously acquired 20x brightfield images. The resin around the cell-of-interest was trimmed away using a glass knife and serial, ultrathin sections of $70\,nm$ were then taken using a diamond

knife on an EM UC7 (Leica Microsystems) and collected on uncoated hexagonal 100 mesh grids (EM resolutions). Electron micrographs were recorded using a JEOL 1400 TEM operating at 100 kV using iTEM software. See figure 2.1.

All CLEM experiments were processed in this way, with the exception of section 4.3 in which *en bloc* uranyl acetate staining was performed before ethanol dehydration at a concentration of 0.5% in 30% ethanol for 1 hour.
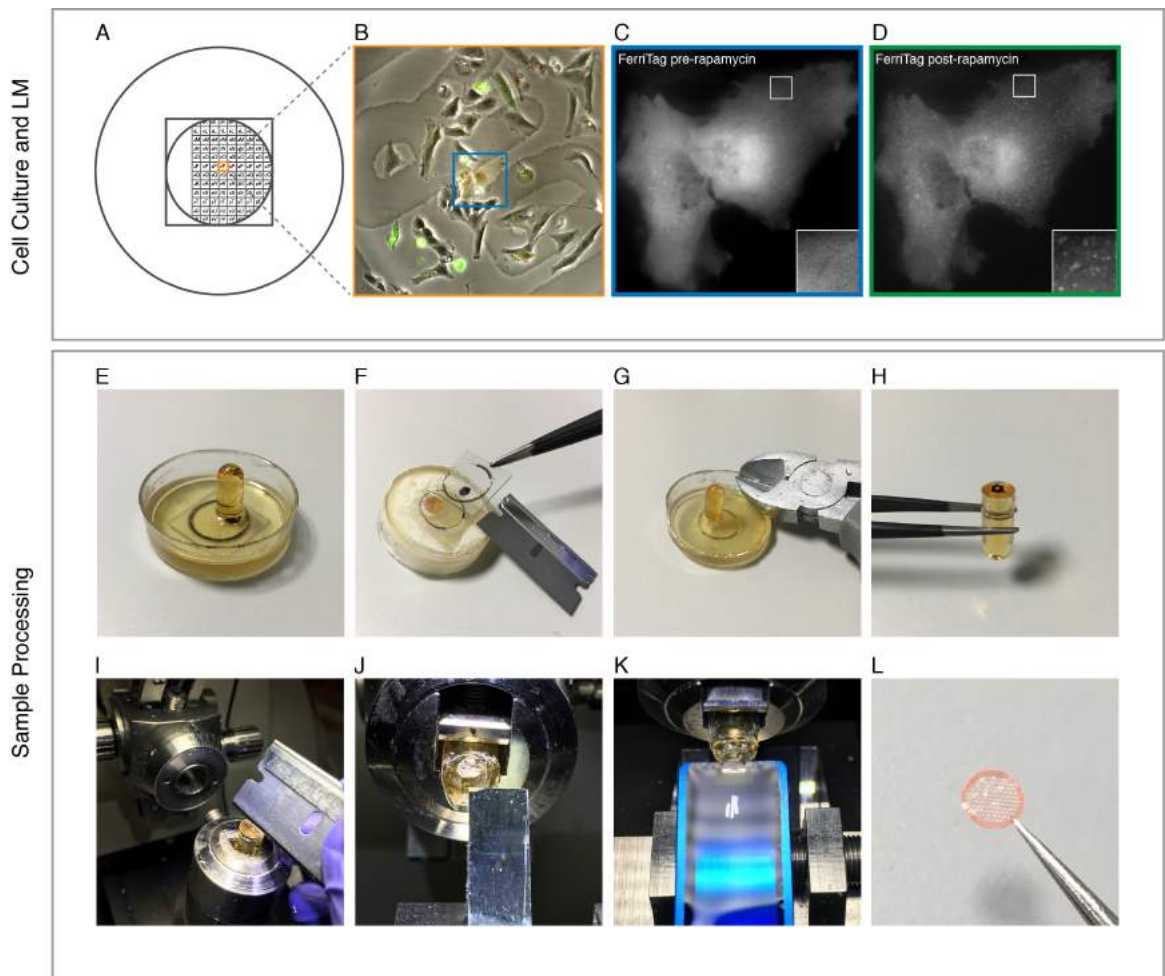
Figure 2.1 CLEM workflow using FerriTag. (A) Gridded glass MatTek dishes are used to track cells throughout the entire workflow. (B) Cells-of-interest are located using the photo-etched coordinates on each grid and a brightfield image is taken at 20x magnification for future reference. (C) The same cell is then imaged using fluorescent live cell imaging at 100x magnification. (D) Rapamycin is added and the protein-of-interest is FerriTagged. (E) Once FerriTaggining has occurred the sample is immediately fixed and processed for electron microscopy. Briefly, each sample is post-fixed and stained with osmium tetroxide and embedded in resin, in which a gelatin capsule filled with resin is placed over the cell-of-interest. (F) Once the resin has polymerized, the surface containing the glass coverslip is placed into liquid nitrogen and the coverslip is removed using a razor blade. (G) The resin-filled gelatin block is then excised by removing the plastic dish and excess resin using pliers. (H) The imprinted grid containing the cell-of-interest on the block is then located and marked using a pen. (I) Excess resin around the marked grid is then trimmed away using a razor blade. (J) A 350 µm square around the cell-of-interest is then trimmed away using a glass knife. (K) Serial 70 nm sections are then taken using a diamond knife and picked up onto uncoated 100 mesh hexagonal copper grids (L). Sections can then be imaged by TEM.

2.5   Image analysis

Kinetics were measured using particle detection on binarized image stacks. Particles were used as a mask to collect mean pixel densities from green (LCa) and red (FerriTag) channels. The ratio of background-subtracted intensities was taken for each particle and the median value (set to 0) used for averaging across multiple cells. As a control, the red channel was spatially randomized and analyzed in the same way, giving no response. Pearson's correlation coeffcient was calculated from red and green fluorescent channels in `IgorPro 7.01`.

For analysis of transferrin uptake, images were thresholded in the far red channel to isolate vesicular structures. Using the `ImageJ` plugin, *analyse particles*, a mask showing particles of 0.03 - 0.8 µm and circularity of 0.3 - 1.0 for each image was created. Pixels over threshold within each cell were measured and values used as the basis for quantification.

Measurement of fluorescence intensity was calculated from background subtracted integrated densities for the whole cell in `ImageJ`.

Sections 4.6, 4.7 and 4.8 contain full details of the determination of the labeling resolution of FerriTag, the signal-to-noise ratio calculation and the automated particle detection, respectively. The synthetic images generated for section 4.7 were made using two images. The first, an 8-bit random noise which is then blurred, and the second is black background. A 3x3 pixel white square is then put at random positions (same location in the two images). The first image is then blurred with Gaussian blur.

For contextual mapping of HIP1R using FerriTag, electron micrographs in TIFF format were imported into `IMOD` and the plasma membrane and location of electron dense FerriTag particles were manually segmented. The coordinates corresponding to contours and objects were fed into `IgorPro 7.01` using the output from `model2point`. Custom-written procedures (available at `https://github.com/quantixed/FerriTag`) processed these data. First, the coordinates were scaled from pixels to real-world values, and the closest distance (proximity) to the plasma membrane was recorded. Then, the

predicted beginning and end of the clathrin-coated pit were defined manually in a graphical user interface. The contour length of the pit was determined and the contour length between the start of the pit and the point of closest approach for each particle was calculated. Using the ratio of these two lengths, a spatially normalized view of particle location in relation to an idealized clathrin-coated pit was plotted. Particles located at distal, uncoated regions and particles inside the pit were plotted separately.

All figures were made in `ImageJ` or `IgorPro 7.01` and assembled in Adobe Illustrator.

All code for image analysis in this thesis was written by Stephen Royle and is available at `https://github.com/quantixed/FerriTag`.

Construct	Vector	Insert	Restriction Sites	Primers	Source/ reference
pMito-mCherry-FTH1	pMito-mCherry-FRB	FTH1	BsrGI, XbaI	-	FTH1 cDNA IMAGE clone: 3459353
RPL5-mCherry-FRB	pMito-mCherry-FRB	RPL5	EcoRI, AgeI	NIC017, NIC018	RPL5 cDNA IMAGE clone: 5736022
RPL22-mCherry-FRB	pMito-mCherry-FRB	RPL22	EcoRI, BamHI	NIC011, NIC012	RPL22 cDNA IMAGE clone: 5109124
FRB-mCherry-FTH1	FRB-mCherry	FTH1	XhoI, EcoRI	NIC055, NIC056	-
FTL only	pEGFP-C1	FTL	AgeI, XhoI	NIC019, NIC020	FTL cDNA IMAGE:2905327
GFP-FKBP-LCa	-	-	-	-	Cheeseman *et al.* 2013
FRB-mCherry-FTH1 (T2098L)	FRB-mCherry-FTH1	-	-	SJR348, SJR 349	-
GFP-FKBP-Myc-MAO	-	-	-	-	Wong *et al.* 2014
CD8-GFP-FKBP	pEGFP-FKBP	CD8α	NheI, AgeI	-	-
HIP1R-GFP-FKBP	pEGFP-FKBP	HIP1R	AgeI, NotI	-	-

Table 2.1 Table of DNA constructs used in this thesis. Listed in order of use.

Primer	Sequence
NIC011	TCAGCGGAATTCCCACCatggctcctgtgaaaaagcttgtggtgaagggg
NIC012	TCAGCGGGATCCGGatcctcgtcttcctcctcttcttcgtcctggtt
NIC017	TCAGCGGAATTCCCACCatggggtttgttaaagttgttaagaataag
NIC018	TCAGCGGGACCGGTGCgctctcagcagcccgctcctgagctctgag
NIC019	TCAGCCACCGGTGGCCACCatgagctcccagattcgtcagaattattcca
NIC020	TCAGCCCTCGAGCTATTAgtcgtgcttgagagtgagcctttcgaagag
NIC055	gcgcCTCGAGccatgacgaccgcgtccacctcgcaggtgcgc
NIC056	caggGAATTCggttagctttcattatcactgtctcccagggt
SJR358	ggaatgtcaaggacctcCTccaagcctgggacctc
SJR359	gaggtcccaggcttggAGgaggtccttgacattcc

Table 2.2 Table of oligos used in this thesis. 5' to 3' sequence of all primers used for sub-cloning or site-directed mutagenesis. Usage cross referenced with Table 2.1.

Development of FerriTag and implementation for light microscopy

---

3.1   Introduction

Genetically encoded probes are essential tools for CLEM that enable specific proteins-of-interest to be visualized at high resolution. As defined in section 1.4, available probes do not meet all of the criteria for an ideal CLEM probe. Therefore, the development of a new genetically-encoded probe for CLEM, is highly desirable. The probe must generate sufficient contrast that is tightly focused in order to be readily visualized by electron microscopy. Therefore, the genetically encoded tag must itself be electron dense or it should have the capability to bind exogenous metal ions to scatter electrons. Furthermore it should be small enough so it can access the target protein and should also be free to diffuse throughout the cytoplasm, otherwise it may interfere with normal cellular processes. Two candidates that are known to be electron dense and are easily distinguishable from background by electron microscopy are ribosomes and ferritin. We wondered if either could be engineered to function as a probe for CLEM.
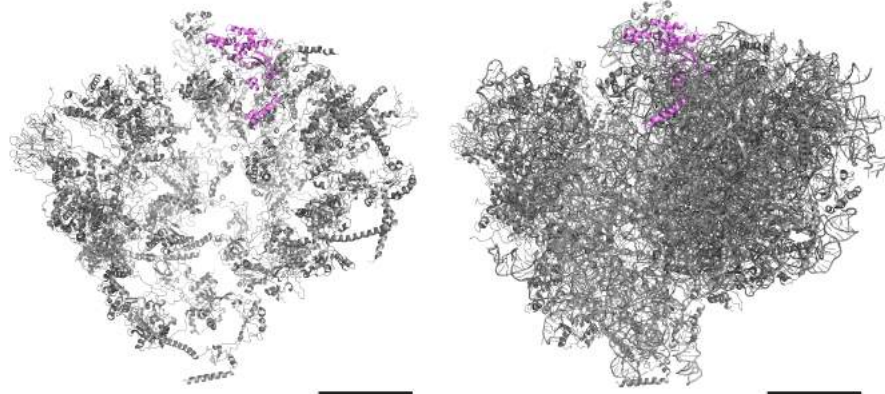
Ribosome

The ribosome catalyzes protein synthesis within the cell. A network of ribosomal proteins form two subunits that link together, which both have distinct functions (Figure 3.1 A). Together they translate the sequence of codons on messenger ribonucleic acid directing the synthesis of a polypeptide chain where it can then form a functional pro-

tein. Ribosomes are found in the cytoplasm or bound to the endoplasmic reticulum. The Eukaryotic ribosome is relatively large in size (approximately 20nm) and generates sufficient contrast to be clearly visualized within the cell by electron microscopy (Leeson and Leeson, 1965).

Ferritin

Ferritin is a small naturally occurring biological complex that acts to regulate iron levels in cells and is found in almost all living organisms. It is made up of 24 polypeptide subunits that form a spherical protein cage approximately 12 nm in diameter (Figure 3.1 B). Subunits consist of heavy-chains (FTH1) that contain the ferroxidase center and light-chains (FTL) that facilitate the mineralization of Fe^{3+}. The Light and Heavy-chain stoichiometry making each cage varies between different tissues (Wilkinson et al., 2006). Within the central ferritin core interior, it has the ability to store up to 4500 iron atoms (Jutz et al., 2015). This high iron content confined within its 7.5 nm core makes ferritin very electron dense and thus can be readily visualized by electron microscopy (Masuda et al., 2010). In fact, ferritin-conjugated antibodies where the first probes to localize proteins by electron microscopy (Singer, 1959). Previous work has highlighted the use of (bacterial) ferritin as a genetic tag for cryo-electron tomography (Wang et al., 2011). However, no work has been undertaken in mammalian cells using a ferritin-based genetic tag for CLEM.

A Ribosome
RPL5

RPL22
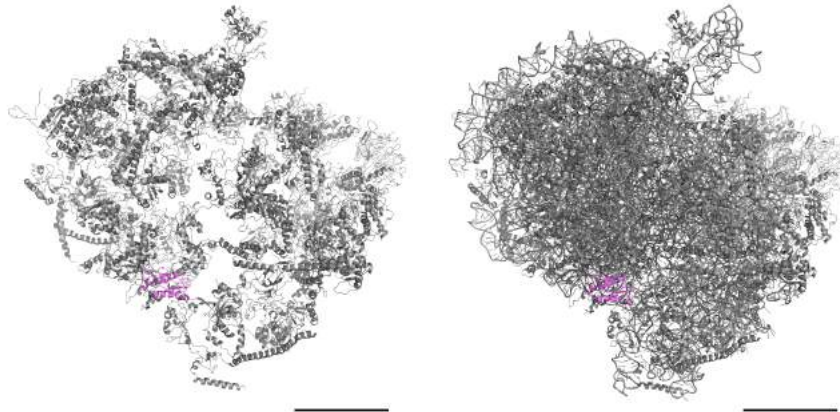
B Ferritin
FTH1
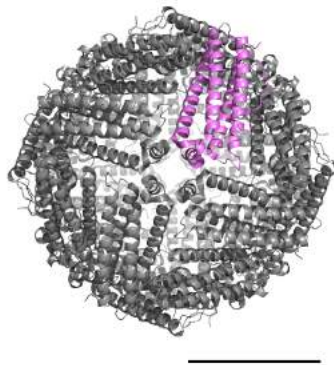
Figure 3.1. Molecular structure of electron dense proteins.
A) Human ribosome (PDB: 5LKS). Ribosomal proteins L5 and L22 that are within the 60S subunit complex of the ribosome are highlighted in pink. Ribosome including RNA also shown to the right.
B) Human ferritin (PDB: 3AJO). Ferritin heavy chain FTH1, is highlighted pink.

Scale bar 5 nm.

Results

3.2 Direct fusion of ferritin results in aggregation

The first attempt to use ferritin as a genetic tag for CLEM in mammalian cells aimed to build upon previous work, by directly fusing ferritin to a protein-of-interest (Wang et al., 2011). A mitochondrial target sequence (Tom70p) fused to mCherry and human ferritin heavy chain (FTH1) was expressed in HeLa cells and imaged by fluorescent light microscopy. However, it was clear this direct fusion resulted in severe aggregation and mislocalization of the mitochondria (Figure 3.2A). This was most likely due to the multivalent nature of the ferritin cage as illustrated in figure 3.2B. It was clear this approach would not work. On this basis we did not try the direct fusion of a ribosomal subunit to a protein-of-interest as we did not want to interfere with normal protein synthesis.
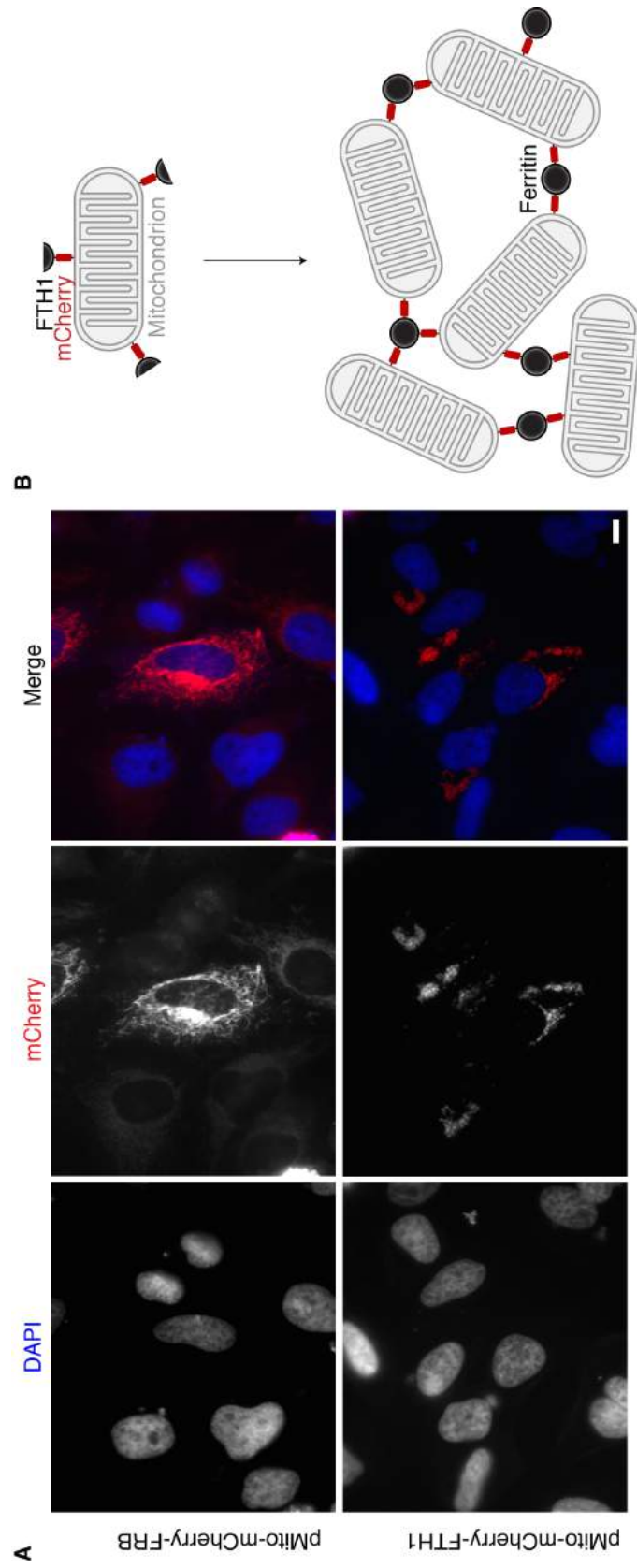
Figure 3.2. Direct fusion of ferritin results in aggregation of mitochondria.
A) Representitive widefield micrographs to show HeLa cells expressing mCherry-FRB and mCherry-FTH1 fused to the mitochondrial targeting sequence of Tom70p. Direct fusion on FTH1 disrupts mitochondria localization (Red, middle), as compared to control where normal mitochondrial morphology is seen in pMito-mCherry-FRB expressing cells. DNA staining using DAPI shown in blue (left) and merge of red and blue (right). Scale bar 10 μm.
B) Schematic diagram illustrating how aggregation is thought to be caused by the multivalent nature of ferritin i.e. multiple mitochondrial target sequences bound to a single ferritin cage leads to aggregation of mitochondria. Note, for for illustrative purposes, only a few mCherry-FTH1 subunits are shown. Theoretically there could be up to 24 in a single ferritin cage.

3.3 Engineering an inducible electron dense particle

As the direct fusion to either ferritin or to the ribosome was not feasible, the idea of inducibly adding them to a protein-of-interest was explored. This would mean each protein can perform its normal cellular function prior to induction. To do this, a rapamycin-induced protein dimerization system was used (Figure 1.4).

Ribosome

Ribosomal proteins that were exposed to the outer surface of the Eukaryotic 60S ribosomal subunit complex were selected (Myasnikov et al., 2016). Ribosomal protein L5 (RPL5) and L22 (RPL22) were suitably positioned, each extending their C-terminus away from the complex exterior (Figure 3.1A). It was thought by expressing a single ribosomal protein with mCherry-FRB fused at their C-terminus, a recombinant 60S subunit complex would form that could be inducibly targeted to an FKBP-tagged protein-of-interest. To test this idea, HeLa cells expressing a recombinant ribosomal complex as well as GFP-FKBP tagged monoamine oxidase (MAO) that localizes to mitochondria, where fixed and processed for fluorescence light microscopy. Before the addition of rapamycin, ribosomal complexes appeared homogeneously distributed in the cytoplasm. However, following rapamycin addition neither RPL5 (Figure 3.3 A) or RPL22 (Figure 3.3 B) relocalized to the mitochondria. It was concluded that without further optimization, ribosomes cannot work as inducible electron dense tags for CLEM.
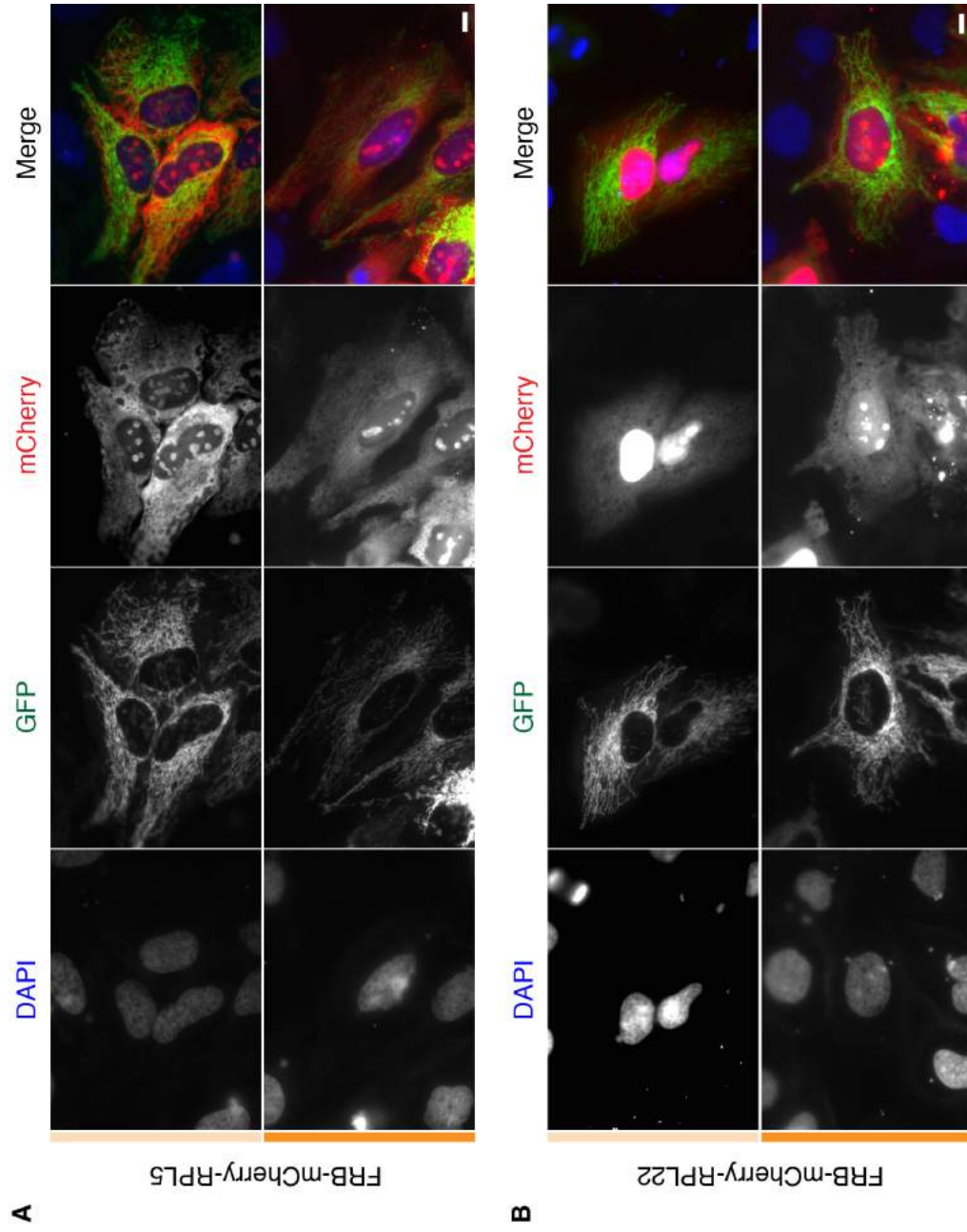
Figure 3.3. Inducible labeling of proteins of interest by ribosomes is not feasible. Representive widefield micrographs to show HeLa cells expressing **A)** FRB-mCherry-RPL5 (Red) or **B)** FRB-mCherry-RPL22 (Red), with GFP-FKBP-Myc-MAO (green), does not result in ribosomes labeling the mitochondria following the addition of rapamycin. DNA staining using DAPI shown in blue. Rapamycin addition is indicated by filled orange bar. Scale bar 10 μm.

63

Ferritin

The same rationale used for ribosomal labelling was applied to engineering an inducible recombinant ferritin cage. FRB-mCherry was fused to the N-terminus of FTH1, allowing the tag to be exposed to the exterior of the recombinant ferritin cage (Figure 3.1B). It is essential FRB-mCherry is exposed to the exterior of the cage, as to not bury the tag inside the core of of the ferritin particle, which may interfere with its dimerization properties or its ability to bind iron. HeLa cells expressing FRB-mCherry-FTH1 as well as GFP-FKBP tagged MAO, where fixed and processed for fluorescence light microscopy. Whilst ferritin appeared to label the target protein following rapamycin addition, it did result in the mislocalization and aggregation of mitochondria. Furthermore, ferritin aggregated with itself prior to rapamycin addition (Figure 3.4). This was likely due to the multivalent nature of ferritin. Therefore, for it to be effectively used as an inducible electron dense tag for CLEM, further optimization was needed.
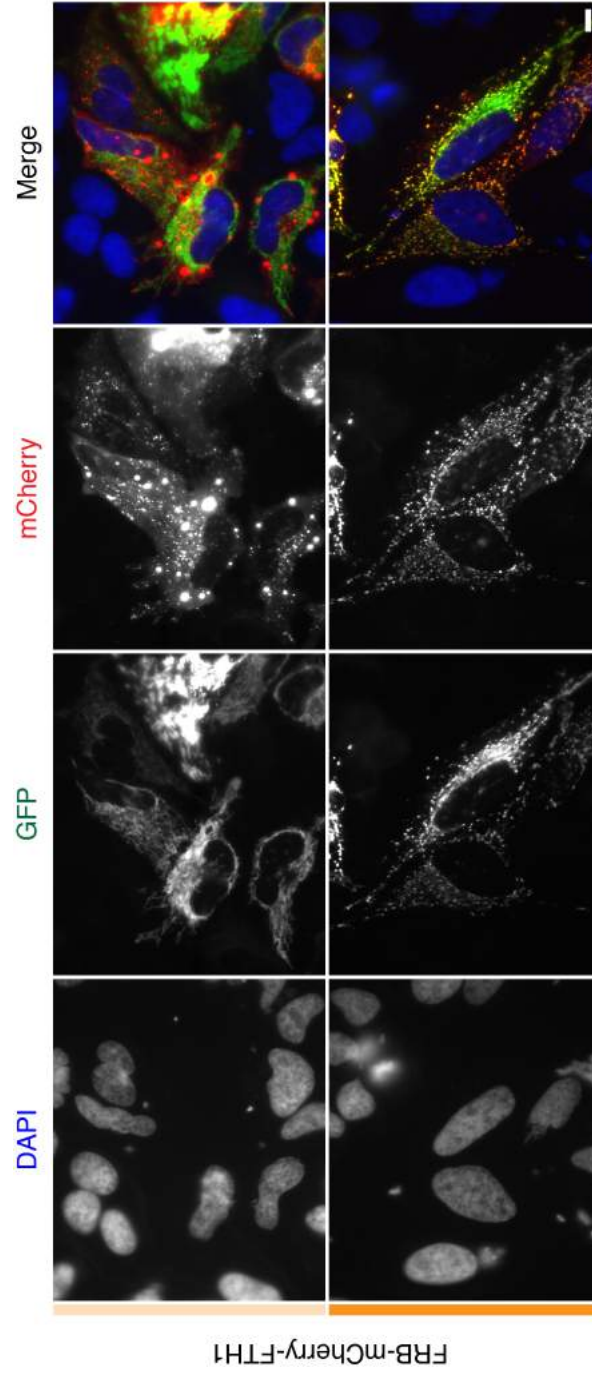
Figure 3.4. Rapamycin-induced labeling of proteins of interest by FRB-mCherry-FTH1 only, is not feasible. Expressing FRB-mCherry-FTH1 only (red) with GFP-FKBP-Myc-MAO (green), results in aggregation of ferritin before rapamycin addition. Inducing FKBP:FRB heterodimerization by adding rapamycin results in labeling, however the mitochondria become mislocalized and aggregated. DNA staining using DAPI shown in blue. Rapamycin addition is indicated by filled orange bar. Scale bar 10 µm.

65

3.4 Optimization of recombinant ferritin for inducible tagging

It was thought that reducing the number of FRB-mCherry subunits per ferritin cage would minimize aggregation issues during recombinant ferritin cage assembly. To test this idea, the number of FRB-mCherry tagged FTH1 subunits were co-expressed with a higher ratio of untagged FTL subunits. HeLa cells expressing FRB-mCherry-FTH1 and FTL at different ratios of (1:2. 1:4 or 1:8) were expressed together with GFP-FKBP-MAO and imaged by fluorescence light microscopy (Figure 3.5). In general a 1:2 ratio still resulted in aggregation of the recombinant ferritin particle whilst 1:8 did not provide sufficient expression of tagged FTH1. Diluting the amount of tagged FTH1 subunits to 1:4 however resulted in the homogeneous distribution of recombinant ferritin prior to rapamycin addition and effectively labelled the protein-of-interest after application without any mislocalization or aggregation issues. We therefore determined this as the optimal condition for expression in HeLa cells and we named this optimized genetically encoded recombinant ferritin particle *FerriTag*. Using this subunit dilution approach with the direct ferritin tag was not seen feasible as we still have limited control over how many tagged and untagged subunits are expressed. It is therefore likely that if the 24 subunit ferritin cage had two or more tagged subunits within its structure, the protein-of-interest would still aggregate and/ or mislocalise.
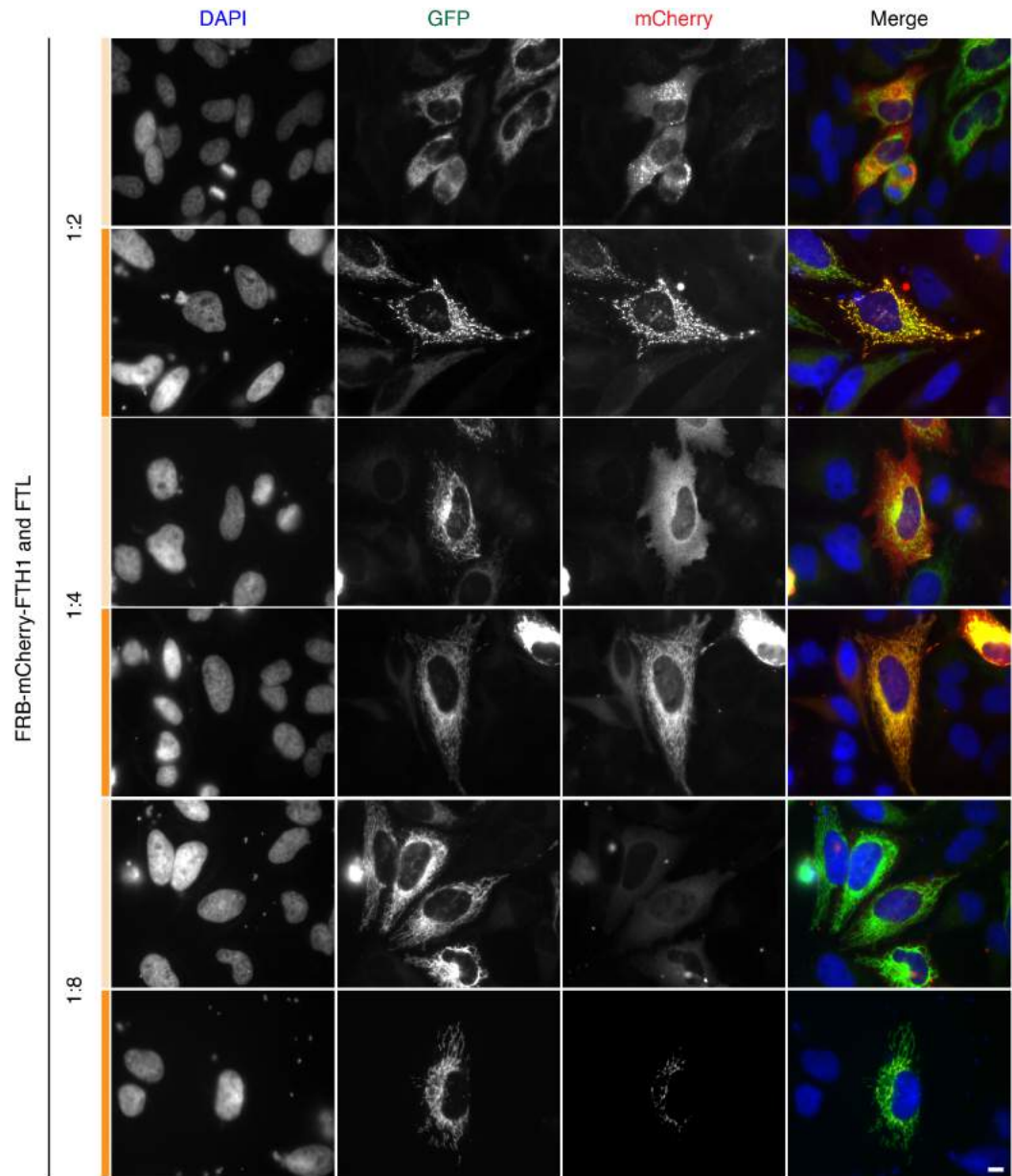
Figure 3.5. FerriTagging results in successful labelling of mitochondria.
Representive widefield micrographs showing HeLa cells expressing FerriTag (FRB-mCherry-FTH1 and FTL) (red) at differant ratios and GFP-FKBP-Myc-MAO (green). No aggregation of either FerriTag (red)or mitochondria (green) is seen before or after the addition of rapamycin with a ratio of 1:4. We therefore determine this is the optimal ratio of FRB-mCherry-FTH1 and FTL when expressed in HeLa cells. DNA staining using DAPI shown in blue. Rapamycin addition is indicated by filled orange bar. Scale bar 10 μm.

67

3.5   Temporal resolution of FerriTagging

Our current model for FerriTag is shown in Figure 3.6. FerriTag assembles in cells by expressing FRB-mCherry-FTH1 and FTL at a ratio of 1:4. At the same time a GFP-FKBP-tagged protein-of-interest is expressed. Prior to the addition of rapamycin, FerriTag is free to diffuse throughout the cytoplasm and the GFP-FKBP-tagged protein-of-interest performs its normal cellular function. Upon the addition of rapamycin, the heterodimerization of FKBP and FRB domains is induced resulting in FerriTag labelling the protein-of-interest. This labelling event is referred to as *FerriTagging*. As both FerriTag and the protein-of-interest are fluorescently labelled, FerriTagging can be observed by light microscopy. This means we can study the dynamics of an event and then correlate this with electron microscopy. It is therefore essential that an inducible system provides rapid labelling of the protein to be able to capture such an event.

To assess the temporal resolution of FerriTagging, HeLa cells expressing FerriTag and GFP-FKBP-LCa where imaged using fast dual camera imaging by spinning disk confocal light microscopy, capturing frames every 2 seconds (Figure 3.7 A). The kinetics of FerriTag appeared to show a very fast labelling phase followed by a much slower accumulation of fluorescence. To look at the on-time of FerriTagging, the time to reach half maximum ($T_{1/2}$) was used as a metric. In the case of labelling clathrin, FerriTagging reaches half maximum within a few seconds following the addition of rapamycin (Figure 3.7 B, C and D). However, due to artefactual "spikes" in fluorescence (discussed below), these values may not be completely accurate and the half maximum on-time of FerriTagging is probably slower. To look into this, FerriTag fluorescence in the cytoplasm was assessed and shown that the time taken to reach half maximum reduction is longer ($T_{1/2} = 17.93$ seconds) which represents a more realistic value. The time taken to reach complete labelling is much slower. This is quantified by the time taken to reach maximum labelling, taking almost 5 minutes (Figure 3.7 B, C and D). These data suggest FerriTagging occurs over two pools, an initial fast pool

and a much slower secondary pool. For all of these experiments, manual addition of rapamycin resulted in artefactual "spikes" in fluorescence during image acquisition. This prevented the fit of curves to data to assess the speed of the fast and slow phases of FerriTagging. Future experiments will use a flow chamber and rapid solution switching to apply rapamycin without disrupting fluorescence measurements.
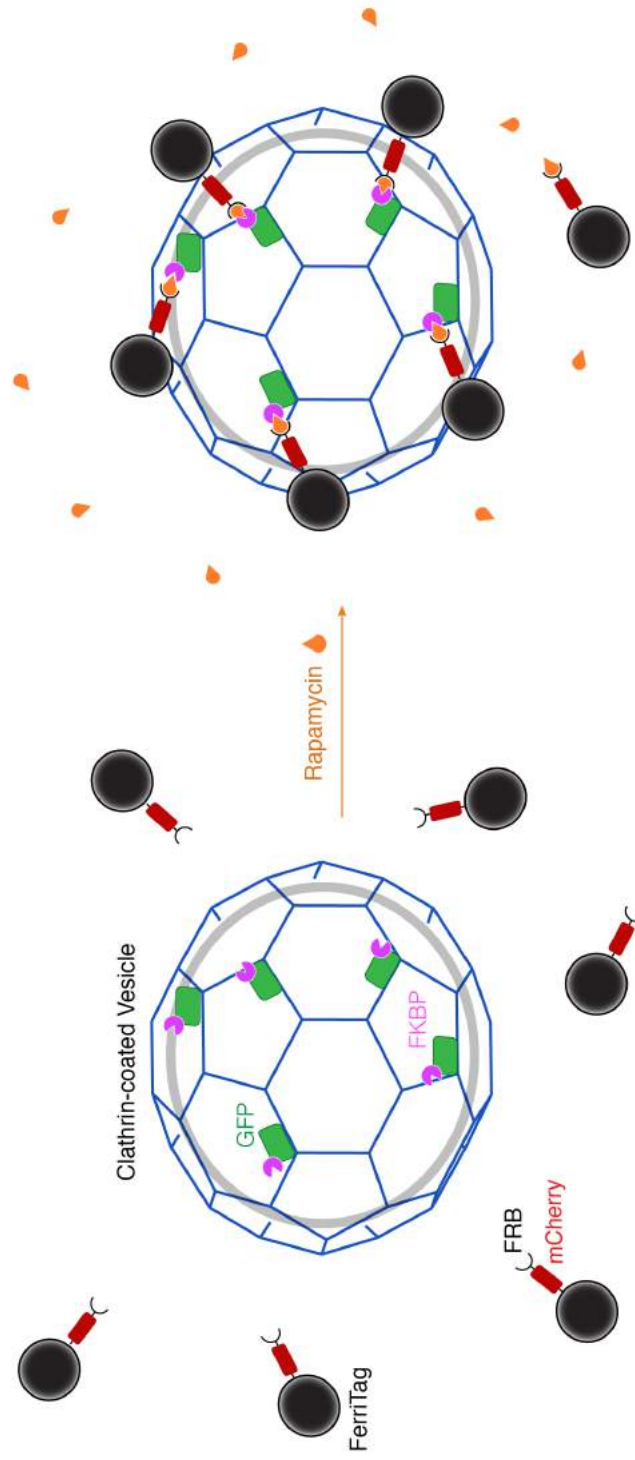
Figure 3.6. Schematic diagram of FerriTagging.
Expression of FerriTag (FRB-mCherry-FTH1 : FTL, 1:4) and GFP-FKBP-tagged LCa. Before rapamycin addition, FerriTag is homogenously distributed in the cytoplasm and LCa performs its normal function. Addition of rapamycin induces the FKBP:FRBheterodimerization resulting in FerriTagging of LCa in a clathrin-coated vesicle. FerriTagging of any GFP-FKBP tagged protein of interest follows this rationale.

70
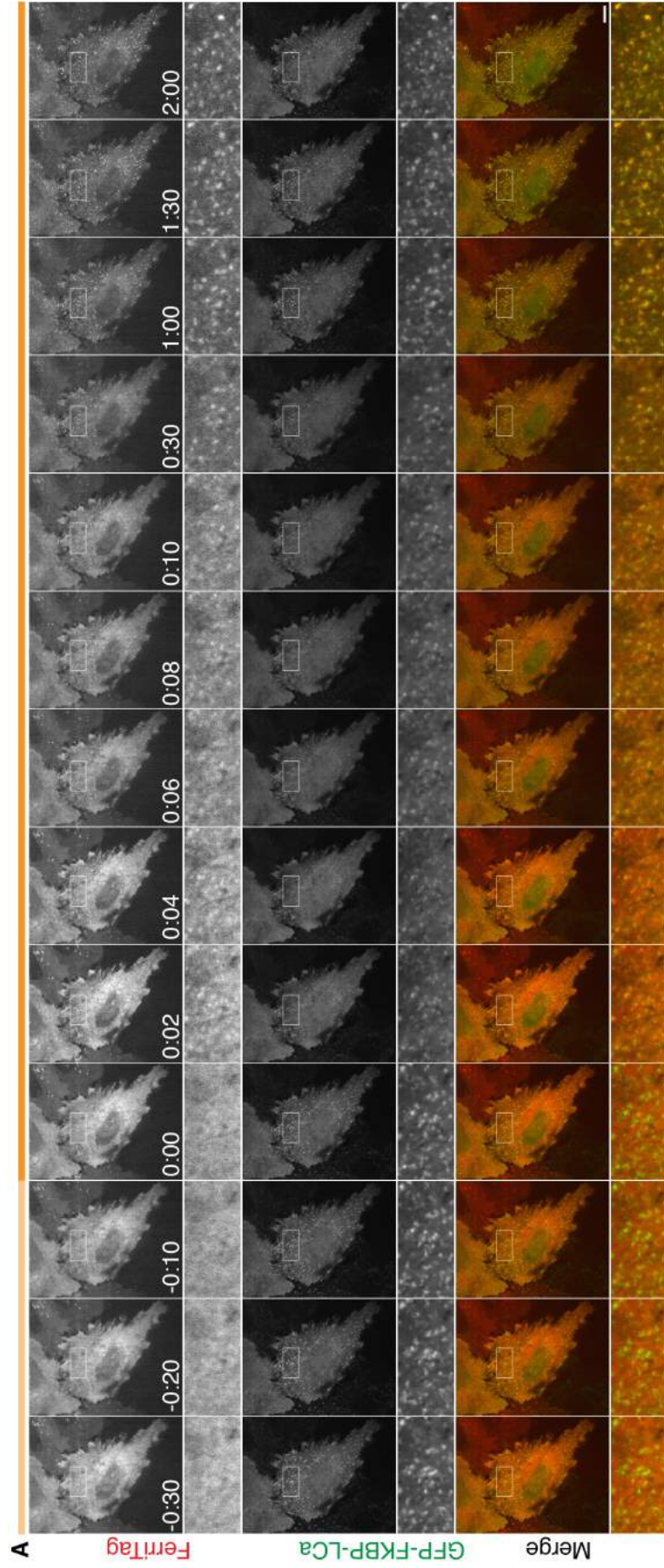
Figure 3.7. FerriTagging has fast temporal resolution.

Figure continued over page.
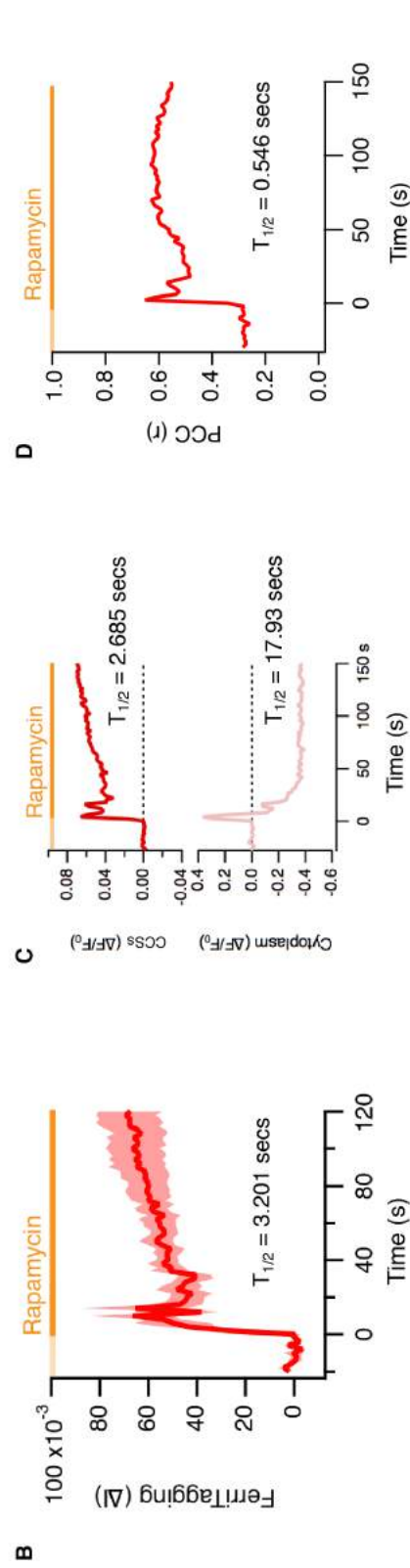
Figure 3.7. FerriTagging has fast temporal resolution.

A) Stills from live-cell imaging of HeLa cells expressing FerriTag (FRB-mCherry-FTH1:: FTL, 1:4) (red) and GFP-FKBP tagged LCa (green). Rapamycin added at time point zero, as indicated by filled orange bar. Imediate, specific and rapid labeling of clathrin by FerriTag can be observed. Zooms show 4x expansion. Time, min : sec, scale bar 10 μm.

B) Quantification of FerriTag (mCherry, red) fluorescence in GFP-FKBP-LCa positive (green) spots as a function of time. Red trace and shading indicate mean ± s.e.m. for 5 cells. Maximum labeling was acheived after 270 seconds.

C) Quantification of FerriTag (mCherry) fluorescence in clathrin-coated structures (CCSs, red) and in the cytoplasm (pink) over time during the experiment shown in A. Maximum labeling of CCSs was achieved after 270 seconds and maximum reduction in cytoplasm was acheived after 262 seconds.

D) Pearson correlation coefficient (PCC,r) calculated from both florescent channels in A, plotted as a function over time. Maximum labeling was achived after 100 seconds.

Rapamycin added at time point zero, as indicated by filled orange bar. Plots inducate the time at which half maximum ($T_{1/2}$) intensity is reached following rapamycin treatment. Note these values were calculated for the whole aquisition (270 secs).

3.6   FerriTagging does not perturb the function of clathrin

For many experiments FerriTagging will occur, dynamics will be observed and the sample will be immediately fixed and processed for electron microscopy. However there are cellular processes that occur on a longer timescale and it is therefore important to assess whether FerriTagging perturbs normal protein function in such cases. An example is clathrin-mediated encocytosis (section 1.2.1).

Therefore, to assess whether FerriTagging inhibits clathrin-mediated endocytosis, transferrin uptake was compared in cells expressing FerriTag and GFP-FKBP-LCa in the presence or absence of rapamycin (Figure 3.8 B). Rapamycin was added for 2 minutes prior to the addition of transferrin, ensuring all LCa was Ferritagged (Figure 3.8 A). Transferrin uptake was left to proceed in both conditions for 10 minutes, permitting sufficient time for its internalization (Figure 3.8 A). Quantification of transferrin uptake showed no difference between LCa Ferritagged cells and cells where no rapamycin was added, suggesting FerriTagging does not inhibit clathrin-mediated endocytosis (Figure 3.8 C). Inhibition of clathrin-mediated endocytosis could readily be detected by pre-treatment of the cells with hypertonic sucrose (0.45 M) (Figure 3.8).
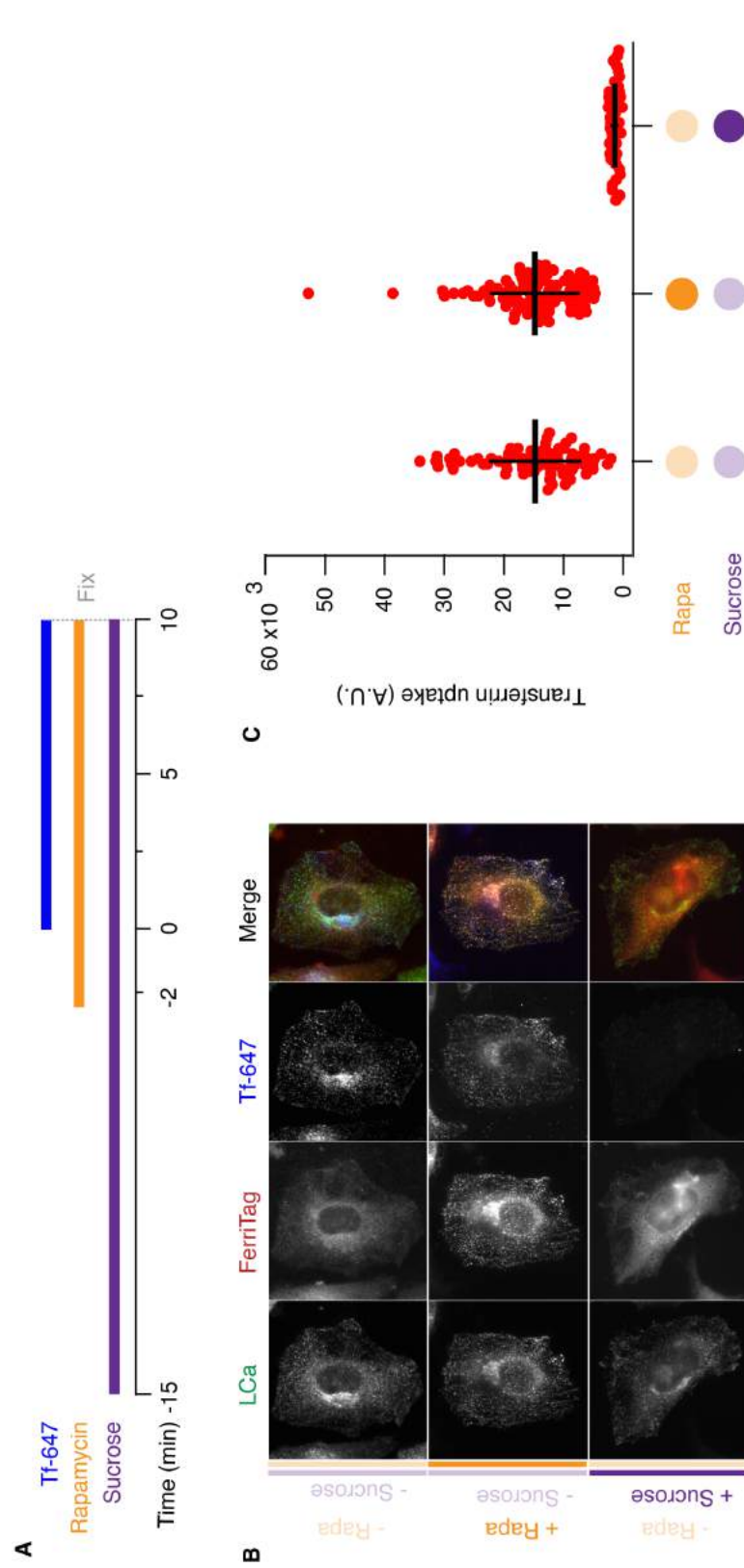
Figure 3.8. FerriTagging does not perturb normal clathrin function.
A) Timeline of experiment shown indicating when transferrin (Tf-647), rapamycin (200 nm) or sucrose (0.45M) was added.
B) Representitive widefield micrographs showing transferrin uptake (Tf-647, blue) in HeLa cells expressing FerriTag (red) and GFP-FKBP tagged LCa (green) following the addition (filled orange bar) or absence (transparent orange bar) of rapamycin. Negative control of hypertonic sucrose to block clathrin-mediated endocytois and thus transferrin uptake is shown (filled purple bar). Scale bar 10 μm.
C) Corresponding scatter dot plot of transferrin uptake. Each dot represents a measurement from an individual cell, bars show the mean (± S.D) from two independent experiments.

75

3.7 Rapamycin analogs are compatible with FerriTagging

A potential limitation of using rapamycin to induce heterodimerization for FerriTagging, is its natural inhibitory effect on mTOR. FerriTagging occurs with in seconds (section 3.5), so over short imaging periods ($<$ 10 minutes), rapamycin will have no effect on mTOR function. However, as suggested in section 3.6, there may be applications where imaging will need to be acquired over longer periods following FerriTagging. To alleviate this issue we assessed whether FerriTag could be engineered to be compatible with rapamycin analogs to induce labelling following the addition of AP21967 (section 1.2.2). Threonine 2098 was mutated to a leucine in the FRB domain of FRB-mCherry-FTH1 to create a rapalog compatible FerriTag. HeLa cells expressing FerriTag (FRB-mCherry-FTH1 T2098L: FTL, 1:4) and GFP-FKBP-LCa where imaged by spinning disk confocal light microscopy, and assessed for FerriTagging following the addition of AP21967 (1 µM) (Figure 3.9 A). FerriTagging occurred immediately following AP21967 treatment (Figure 3.9 B) and specifically labelled clathrin-coated structures, similar to inducing heterodimerization by rapamycin (Figure 3.7).
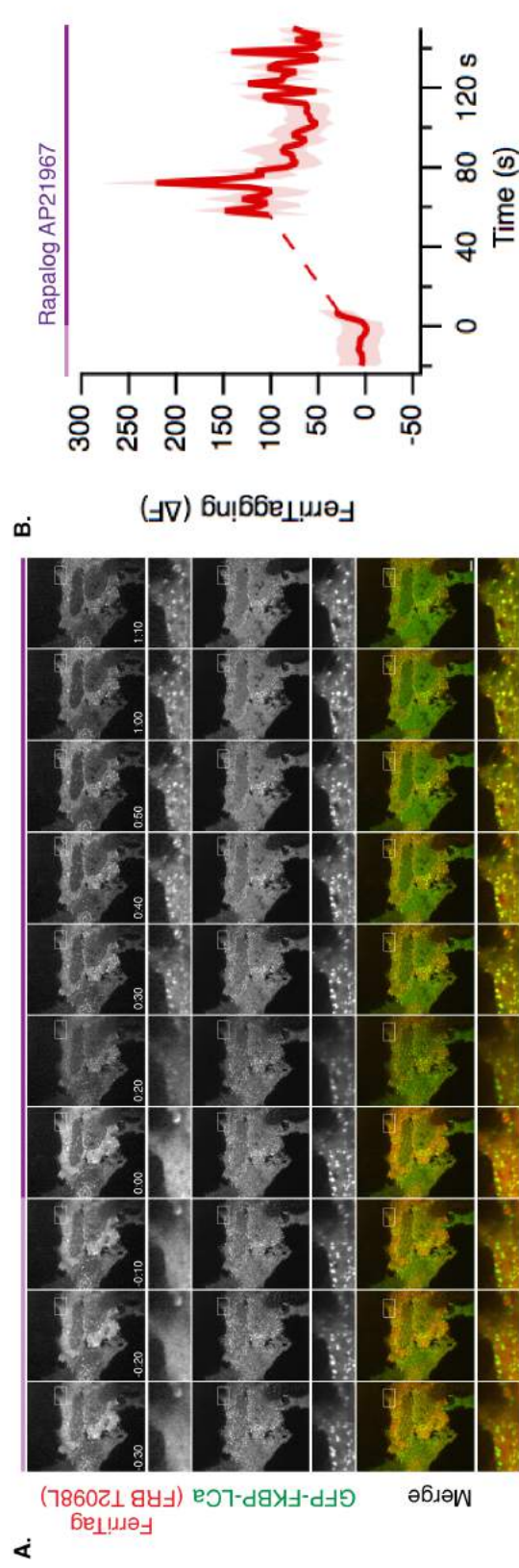
Figure 3.9. Rapamycin analogs can be used for FerriTagging.

A) Stills from live-cell imaging of HeLa cells expressing rapamycin analog compatible FerriTag (FRB-mCherry-FTH1 T2098L:: FTL, 1:4) (red) and GFP-FKBP tagged LCa (green). Rapalog AP21967 addition (1 μM) added at time point zero, as indicated by filled purple bar and specific, rapid labeling of clathrin (green) by FerriTag (FRB T2098L) (red) can be observed. Zooms show 4x expansion. Time, min : sec; scale bar 10 μm.

B) Quantification of FerriTag T2098L (mCherry, red) fluorescence in GFP-FKBP-LCa positive (green) spots as a function of time during the experiment shown in A. Red trace and shading indicate mean ± s.e.m. Rapalog AP21967 addition added at time point zero, as indicated by filled purple bar. The dotted line represents image frames that were not used for analysis due to focus drift during image acqusition, which obscured quantification.

3.8   Discussion

This chapter introduces FerriTag, a new genetically encoded tag for CLEM. The development and implementation of the method had been achieved for light microscopy.

Initial optimization focused on circumventing issues associated with the use of genetically-encoded ferritin. By expressing a mixture of untagged human ferritin light chain (FTL) with a lower concentration of FRB-mCherry tagged human ferritin heavy chain (FTH1), we can build an inducible recombinant ferritin cage (FerriTag) that does not aggregate with itself, or the target protein, before the addition of rapamycin. Following the addition of rapamycin, FerriTag rapidly labels the protein-of-interest with high specificity. No aggregation of Ferritagged proteins-of-interest was seen for those we tested. Furthermore, we show that FerriTagging does not interfere with normal clathrin function. This is important for experiments where Ferritagged proteins will be imaged for longer periods. However, the impact of FerriTagging on normal protein function for other experiments would need to be assessed, case-by-case.

The temporal resolution data suggests FerriTagging occurs within two pools (Section 3.5). An initial fast pool labels the target structure quickly following rapamycin addition. The resulting slow pool then continues to FerriTag the target protein but over a much slower time-scale. These two pools likely reflect how FerriTag can label structures within close proximity quickly following rapamycin addition but once FKBP binding sites on the protein-of-interest get taken up, the amount of FerriTag binding events become less frequent. Taken together, these data suggests the kinetics will permit the use of FerriTag to localize proteins involved in dynamic cellular processes but restricted to events that occur on a time-scale that last at least 20 seconds or more. This is further discussed in section 5.

Currently there is limited control over how many FRB-mCherry tagged FTH1 subunits are expressed with untagged FTL subunits when FerriTag is made in cells. Whilst expressing tagged and untagged subunits at a ratio of 1:4 gives good expression of FerriTag with no adverse aggregation issues, using transient transfection of two separate

plasmids to do this may sometimes result in some cells not expressing, or expressing to much or too little of one plasmid. To circumvent this, it is possible to make a bicistronic vector containing an internal ribosome entry site (IRES) to ensure both transgenes are expressed. As the expression efficiency of the IRES is not as strong as a cytomegalovirus (CMV) promoter, the correct expression ratio of tagged and untagged ferritin subunits can be achieved (Kuzmich et al., 2013). In addition, a chimeric fusion incorporating multiple ferritin subunits can be engineered. It has previously been reported that the fusion of FTL and FTH1 using a flexible linker is possible to express ferritin in mammalian cells that advantageously also has enhances the iron-loading properties of ferritin (Iordanova et al., 2010). It is therefore plausible a similar construct can be engineered for FerriTag i.e. FRB-mCherry-FTH1-FTL, that may help control subunit stoichiometry when expressed.

A potential limitation of FerriTagging is the use or rapamycin. We show FerriTagging is compatible with rapalogs that can dimerize with exogenous FRB domains but do not interfere with mTOR signalling pathways.

As endogenous FKBP is a highly abundant cytosolic protein, it can potentially out-compete exogenous FKBP for FRB binding, thereby decreasing heterodimerzation efficiency. This may be problematic when studying low abundant proteins using FerriTag, as lower levels of exogenous FKBP are expressed. In such cases, we would deplete endogenous FKBP, which has been shown to improve efficiency of rapamycin-induced dimerization (Ballister et al., 2014). Similarly, exogenous FKBP-rapamycin complexes can bind endogenous mTOR. Consequently, endogenous mTOR would bind the target protein instead of FerriTag. If this proves problematic, we would combine endogenous FKBP knockdown with rapalog compatible FerriTag.

Future improvement to the FerriTag methodology may look to other CID systems to improve labelling efficiency and dynamics. Although rapamycin-induced dimerization using FerriTag has fast temporal resolution it may be that other techniques are quicker. The plant hormone, gibberellin, has recently been shown to trigger the interaction between a gibberellin insensitive dwarf1 (GID1) and a gibberellin insensitive (GAI)

domain for CID experiments (Figure 1.4 C). As this system is completely orthogonal it may result in faster labelling dynamics compared to rapamycin. Furthermore it will not interfere with endogenous cellular processes (Miyamoto et al., 2012).

In conclusion, we begin to meet the essential criteria for the ideal CLEM probe that are discussed in section 1.3 and with this method now working well by light microscopy, we now wanted to visualize FerriTagging by electron microscopy to localize proteins at the nanoscale.

Characterization and application of FerriTag using correlative light electron microscopy

4.1 Introduction

In the previous chapter we showed that FerriTagging works effectively as assessed by light microscopy. We saw how FerriTag could be attached to a protein-of-interest upon addition of rapamycin. We next wanted to characterise FerriTagging by electron microscopy. Key questions are whether the genetically-encoded proteins assemble to form a particle which can bind iron and whether these particles are specifically attached to proteins-of-interest. We also wanted to determine the resolution of FerriTagging. If FerriTag works well as a CLEM probe, we should be able to use it to address a real problem in cell biology.

Results

4.2 Loading FerriTag with iron is non-toxic to HeLa cells

In order to visualize FerriTag by electron microscopy, it must bind enough iron to provide sufficient contrast to be distinguished from background noise. An iron-loading step during cell culture is therefore required. We reasoned the greater amount of iron the cell can take up, the greater the amount of iron FerriTag can bind and thus appear more electron dense. The concentration of iron used must be non-toxic to cells. Previous work, has shown that incubating HeLa cells for 72 hours in iron-rich culture medium containing 500 ug/ml of iron (3.3 mM $FeSO_4$) has adverse effects on cell viability and ultrastructure (Jauregui et al., 1975). Determining the optimal culture time and concentration needed for loading cells with iron was therefore essential for FerriTagging.

HeLa cells where incubated in varying concentrations of iron-rich media over periods of up to 48 hours. Cell viability was determined using the trypan blue exclusion assay at various time points up to 48 hours for each concentration (Figure 4.1). Whilst cell viability decreases over time at increasing iron concentrations, minimal toxicity was observed in cells cultured for 16 hours in media supplemented with $1\,\text{mM}$ $FeSO_4$ (98.5%). This was seen acceptable compared to control (99.87%), whereas increased concentrations at the same time point significantly reduced cell viability i.e. $3\,\text{mM}$ $FeSO_4$, 93%. Thus, $1\,\text{mM}$ $FeSO_4$ for 16 hours was used during CLEM sample preparation to load FerriTag with iron.
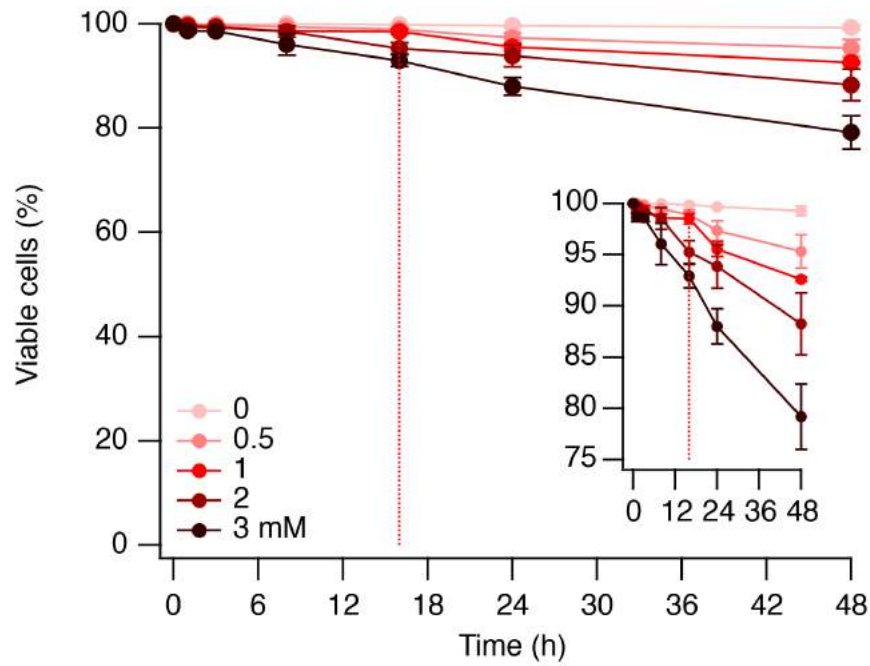
Figure 4.1. Quantification of cell viability in iron-supplemented media. HeLa cells were supplemented with the indicated concentrations of $FeSO_4$ and cell viabilty was assessed by trypan blue exclusion at various time points. Markers indicate mean ± SD from three experiments. Dashed red line indicates the 16 hour time point. 1 mM $FeSO_4$ for 16 hours was the chosen condition for FerriTagging. Inserted graph shows zoomed in region at this concentration to better visualise cell viability between each condition.

4.3 Optimization of sample processing using FerriTag for CLEM

For FerriTag to be effectively used for CLEM, the electron density generated from its iron-loaded core must not be masked by over-staining samples during processing for electron microscopy. However, samples must be stained by heavy metals so cellular ultrastructure can be visualized. Finding the correct balance is therefore essential.

Initial optimization of sample processing was performed in a correlative manner (section 1.1). HeLa cells were transfected with FerriTag (FRB-mCherry-FTH1: FTL, 1:4) and a GFP-FKBP-tagged protein-of-interest and plated on to gridded-glass culture dishes in order to track cells throughout the entire workflow. Prior to imaging, cells are incubated in media supplemented with 1 mM $FeSO_4$ for 16 hours (section 4.2). Fluorescent light microscopy is then performed and cells expressing both FerriTag and the GFP-FKBP-tagged protein-of-interest are selected. Rapamycin (200 nM) is added and FerriTagging is observed. Once sufficient tagging has been achieved, cells are fixed chemicaly. Samples are then post-fixed and stained in 1% osmium tetroxide for 1 hour and prepared for embedding in plastic resin prior to imaging by transmission electron microscopy (TEM) (figure 4.2 A).

Routine heavy metal staining for electron microscopy generally uses en-bloc uranyl acetate and on-section uranyl acetate and lead citrate staining (Graham and Orenstein, 2007). However, we found these masked the electron density of FerriTag and were therefore omitted from the protocol (figure 4.2 B). The final optimized workflow for processing Ferritagged samples for correlative light electron microscopy using chemical fixation is shown in figure 4.2 and is used for all following CLEM experiments herein.

It should be noted that there may be other processing protocols or techniques that are more suited for the better visualization of FerriTag, including those that better preserve cellular ultrastructure such as high pressure freezing and freeze substitution. These workflows are discussed in chapter 5.

A

Prep
Transfect FerriTag & protein-of-interest → Seed cells onto gridded dishes → Iron-rich media
⌐ 16 h

LM
Live-cell microscopy → Add rapamycin (200 nM) → Fix cells

EM
Post-fix, stain 1% OsO$_4$ —1 h→ Processing, Ultrathin sectioning → TEM imaging of unstained sections

B

en bloc UA   No *en bloc* UA
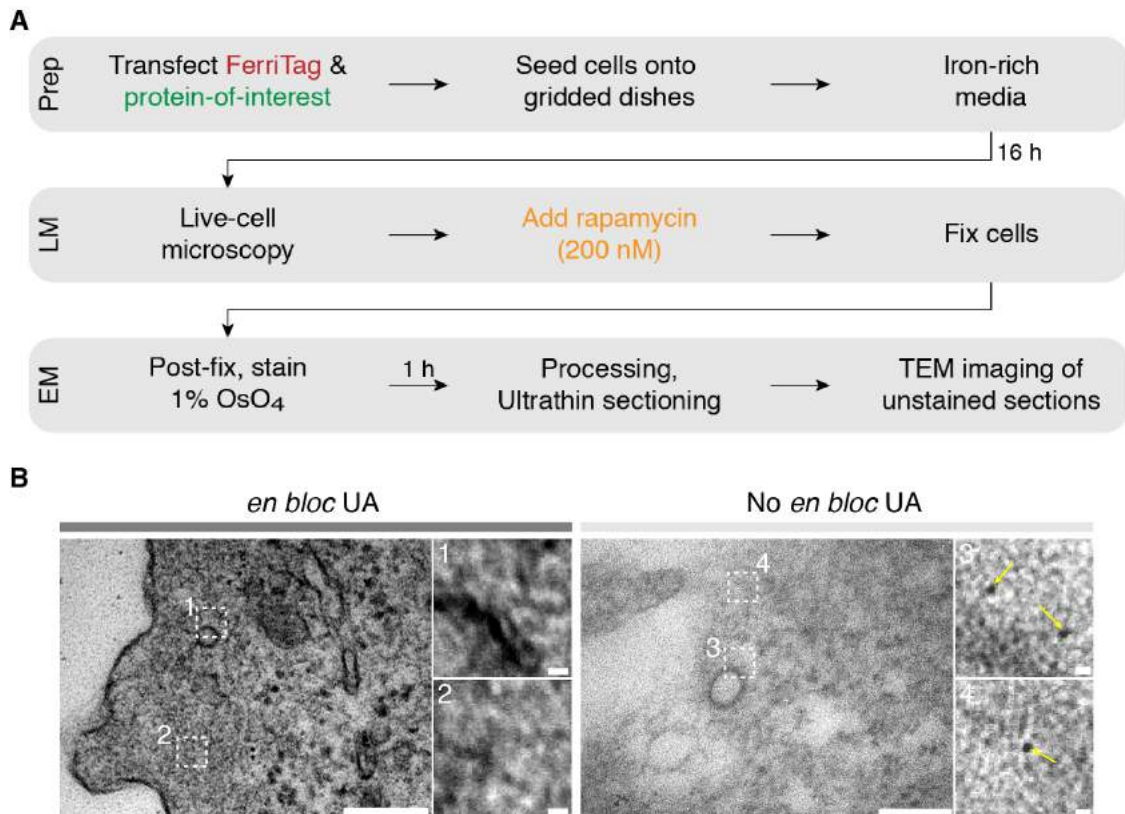
Figure 4.2. Sample processing using FerriTag for CLEM.
A) Optimized workflow outlining steps for sample processing to correlate light with electron microcopy using FerriTag.
Preparation (Prep): Cells are first transfected with FerriTag and a GFP-FKBP tagged protein of interest. They are then seeded onto gridded glass culture dishes for tracking. Iron-rich media is added to increase the electron density of FerriTag.
Light microscopy (LM): Cells expressing transfected proteins are imaged by live-cell fluorescent microscopy. Rapamycin induces the heterodimerization of FKBP and FRB, resulting in FerriTagging of the protein-of-interest. Once sufficient labelling has been observed, cells are immediately chemically fixed.
Electron microscopy (EM): Fixed cells are post-fixed and stained in 1% osmium tetroxide (OsO$_4$), dehydrated in grade series ethanol and embedded in epoxy resin. Ultrathin serial sections containing the same cell imaged by light microscopy are taken and then imaged by transmission electron microscopy (TEM).
B) Representitive electron micrographs to show comparison of sample staining conditions, with and without uranyl acetate (UA). Addition of UA masks electron density of FerriTag. Removal of UA enables clear visualization of FerriTag particles (yellow arrows) and ultrastructure can still be seen. Scale bar 200 nm for non-zoom image and zoom (x5) 10 nm.

4.4 FerriTag can be used to localize intracellular proteins using CLEM

We next wanted to assess whether FerriTag could be used to localize intracellular proteins at the nanoscale following the optimized correlative workflow outlined in section 4.3. To do this, two different proteins in disparate locations were selected that could be easily distinguished in the cell by electron microscopy.

- Monoamine oxidase (MAO) an outer mitochondrial membrane protein

- Clathrin light chain a (LCa), part of the clathrin triskelion (Section 1.2.1)

Each protein was tagged with GFP-FKBP, expressed in HeLa cells with FerriTag (FRB-mCherry-FTH1: FTL, 1:4) and imaged by live-cell fluorescent light microscopy (figure 4.3). The grid coordinate containing each cell-of-interest were noted for tracking of the same cell throughout the CLEM workflow. Prior to rapamycin addition, FerriTag is homogeneously distributed throughout the cell and both the mitochondria and clathrin do not aggregate or mislocalise. Rapamycin addition induced the heterodimerization of both FKBP and FRB resulting in FerriTag specifically labelling each protein-of-interest rapidly. Following fixation and processing, ultrathin sections of the same cell imaged by light microscopy were imaged by electron microscopy. Electron dense FerriTag particles, the correct size of the interior core of human ferritin (7 nm), could be easily distinguished from background noise in electron micrographs. Furthermore, the ultrastructure of the cell is also visible. Specifically, electron dense FerriTag particles can be seen decorating the mitochondrial membrane in GFP-FKBP-Myc-MAO cells and clathrin-coated pits and vesicles in GFP-FKBP-LCa cells, where each protein-of-interest is normally located.
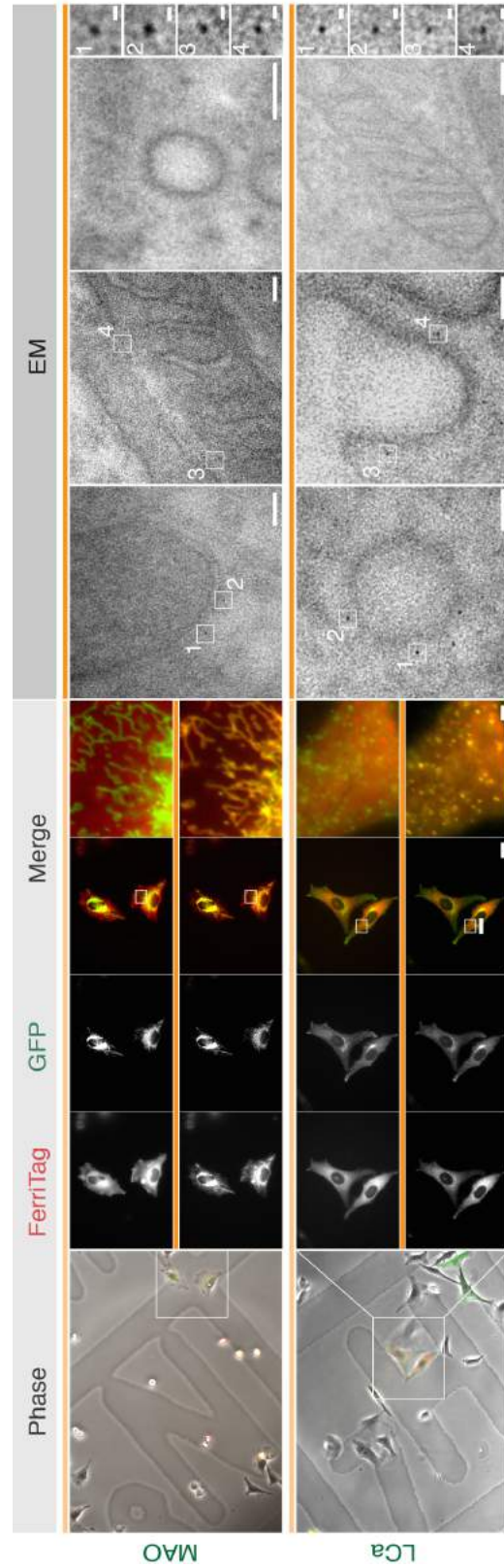
Figure 4.3. Visualizing FerriTagged proteins by light and electron microscopy.

Light and electron micrographs of HeLa cells co-expressing FerriTag (FRB-mCherry-FTH1: FTL, 1:4) (red) with either GFP-FKBP-Myc-MAO (green, top) or GFP-FKBP-LCa (green, bottom).

Light grey: Stills from live-cell imaging. Cells first imaged at low magnification to aquire location co-ordinates on gridded dishes for tracking (Phase). Cells then imaged by fluorescent light microscopy at high magnification to observe FerriTagging each protein-of-interest following rapamycin addition indicated by filled orange bar. The last frame is shown before the cell was fixed and processed for electron microscopy (EM).

Dark grey: The same cell imaged by light microscopy is relocated and imaged by EM. Electron dense particles of approximately 7 nm can be seen decorating the mitochondrial membrane in GFP-FKBP-Myc-MAO cells and clathrin-coated pits and vesicles in GFP-FKBP-LCa cells, where each protein-of-interest is localized. Two particles per micrograph are shown expanded to the right. Internal controls show that FerriTag particles are specific to the target protein and not found at other regions.

Light microscopy scale bar 10 μm and zoom (x12) 1 μm.

Electron micrograph scale bar 50 nm and zoom (x7.25) 10 nm.

4.5 FerriTagging is specific to the target protein

Whilst we could observe electron dense particles in the vicinity of the target protein that consistent with size and shape as ferritin (Figure 4.4 A), we needed direct evidence that they were FerriTag. Three control experiments using different sample preparation conditions were set up that would determine their identity and test the specificity of FerriTagging.

First, samples prepared in section 4.4 could be used as internal controls (Figure 4.4 B). That is we checked to see the density of labelling at non-target sites. No particles were seen decorating clathrin-coated structures in cells where MAO was Ferritagged. Similarly, no particles were seen on the mitochondrial membrane in cells where LCa was Ferritagged.

Second, HeLa cells where prepared for CLEM as before (Section 4.3) but without the addition of rapamycin (Figure 4.4 C). FerriTag particles still form in absence of rapamycin, but without heterodimerization between FKBP and FRB, no FerriTagging of the protein-of-interest occurs. This results in no obvious particles in the vicinity of the target organelle in samples expressing FerriTag with either GFP-FKBP tagged MAO or LCa. Note, FerriTag can be seen within the cytoplasm.

Finally, HeLa cells where prepared for CLEM as before (Section 4.3) but were cultured in normal media and not under iron-rich conditions (Figure 4.4 D). Whilst FerriTag could label the protein-of-interest by light microscopy, no obvious particles (compared to iron-loaded cells 4.4 A) were observed in rapamycin treated cells that had no iron preincubation. In some cases, particles that may be FerriTag could be partially visualised. However, they were much less dense (shown by comparing representative line scans from Figure 4.4 A and D) suggesting cells needed to be iron-loaded to enhance particle contrast.

The number of FerriTag particles found in the cytoplasm and labelling the target membrane are counted in 4.4. Particles within a 15 nm membrane-proximal region for MAO were counted i.e. the maximum length state of FerriTag calculated in section

4.6 and a 50 nm region for LCa i.e. maximum length state plus clathrin coat (approximately 35 nm (Wood et al., 2016)). It is clear the number of FerriTag particles at target membrane increases following the addition of rapamycin to induce FerriTagging. However a much more quantitative approach is needed to fully assess the efficiency of labelling.

Together, these experimental conditions provide strong evidence the electron dense particles observed decorating the protein-of-interest are FerriTag and that FerriTagging is specific to the target protein. Furthermore, it also shows an excess of iron is needed to provide sufficient electron density for it to be readily visualised by electron microscopy.
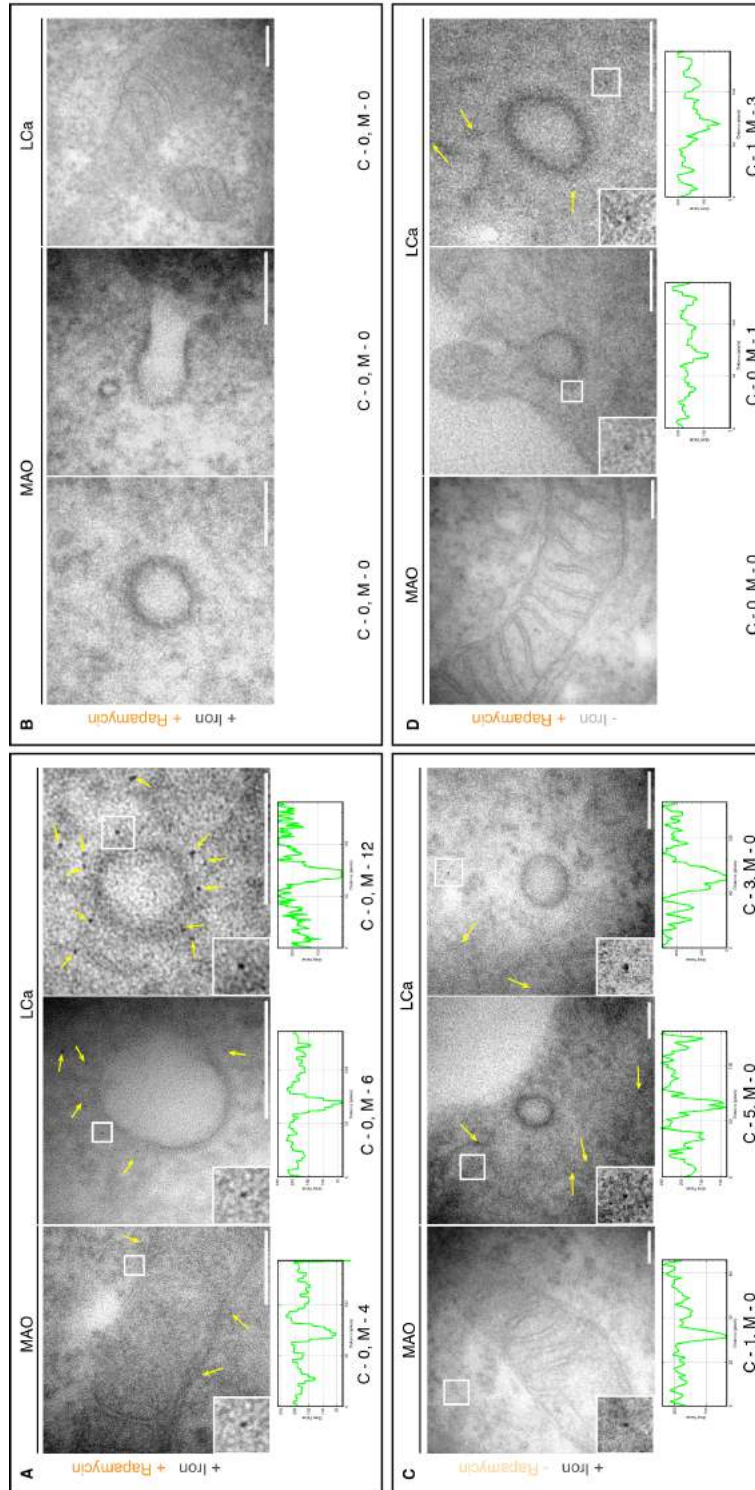
Figure 4.4. Identity of FerriTag particles and specificity of FerriTagging.
Representitive electron micrographs to show four independent control experiments. FerriTagging was of the indicated construct, GFP-FKBP-Myc-MAO (MAO) or GFP-FKBP-LCa (LCa). Rapamycin treatment and/ or iron loading is stated. Yellow arrows indicate FerriTag particles. Where FerriTag particles can be seen in each electron micrograph, a zoomed image is shown, with its density profile plotted showing peaks at positions corresponding to location of FerriTag. The number of FerriTag particles in the cytoplasm (C) and at target site membrane (M) are shown.
A) FerriTagging of mitochondria and clathrin-coated structures can be clearly seen in cells treated with rapamycin and iron.
B) Internal controls. No labeling of clathrin-coated structures in cells where MAO had been FerriTagged and no labeling of mitochondria in cells where clathrin had been FerriTagged.
C) No labeling of either the mitochondria or clathrin-coated structures in the absence of rapamycin. Note, some FerriTag particles can be seen in the cytoplasm.
D) No labeling of either the mitochondria or clathrin-coated structures when rapamycin had been added but iron-loading was carried out.
Scale bar 100 nm.

4.6 The labelling resolution of FerriTag is on the order of 10 nm

We define labelling resolution as the measurement of accuracy that defines how precise the detected position of a particle corresponds to the location of a labelled protein. This is calculated by how far the particle is relative to its target. Theoretically, this distance could be up to 22 nm for FerriTag (Figure 4.5 A). This prediction is based on the sum of lengths estimated from co-linearly aligning the structures of all the components in a Ferritagged complex i.e. -GFP-FKBP-Rapamycin-FRB-mCherry-Ferritin. However, flexibility in the linkers between each domain in the complex means it may adopt a different conformation that would reduce the distance between the target protein and FerriTag. Moreover, the tag itself is mobile and could be in a number of poses relative to its target.

To experimentally determine the labelling resolution, CD8a, a transmembrane protein was Ferritagged. This gave a clear surface from which to measure particle distances. HeLa cells expressing FerriTag (FRB-mCherry-FTH1: FTL, 1:4) and GFP-FKBP-CD8α were imaged by live-cell fluorescent light microscopy and following FerriTagging of CD8α, cells where processed for electron microscopy as described in section 4.3 (figure 4.5 B). Electron micrographs show FerriTag decorating CD8α at the plasma membrane. The perpendicular distance from the centre of the FerriTag particle to the inner side of the plasma membrane was measured for 458 particles which gave a median distance of *9.5 nm* (figure 4.5 C).

To interpret the shape of the experimental distribution, computer simulations were carried out that modelled the detection of FerriTag particles in electron micrographs. To do this, the origin of each particle was set on an xy plane at z = 0, and FerriTag was modelled as a ball-and-chain. The length state, pose, sampling and error was then built into each simulation. The first simulation modelled FerriTag at a fixed length of 22 nm, due to this being its maximum theoretical length state (Figure 4.5 A). However it was clear this distribution did not fit the experimental data (Figure 4.5 C i). Due to

flexibility in the linkers of the domains between the ferritin particle and target protein, it is likely that FerriTag exists at distances shorter than 22 nm. The second simulation therefore modelled FerriTag where it could exist over a number of length states between 6.5 and 22 nm i.e. the minimum and maximum theoretical length state, respectively. The simulation that best fit experimental data was where FerriTag could exist in a number of length states from 7 to 18 nm (Figure 4.5 C ii). The median value was calculated to be *10.5 nm*, which was in line with experimental data. Furthermore, the simulation indicates the observed distance in electron micrographs underestimates the length state by around 11% to 13% (Figure 4.5 D).
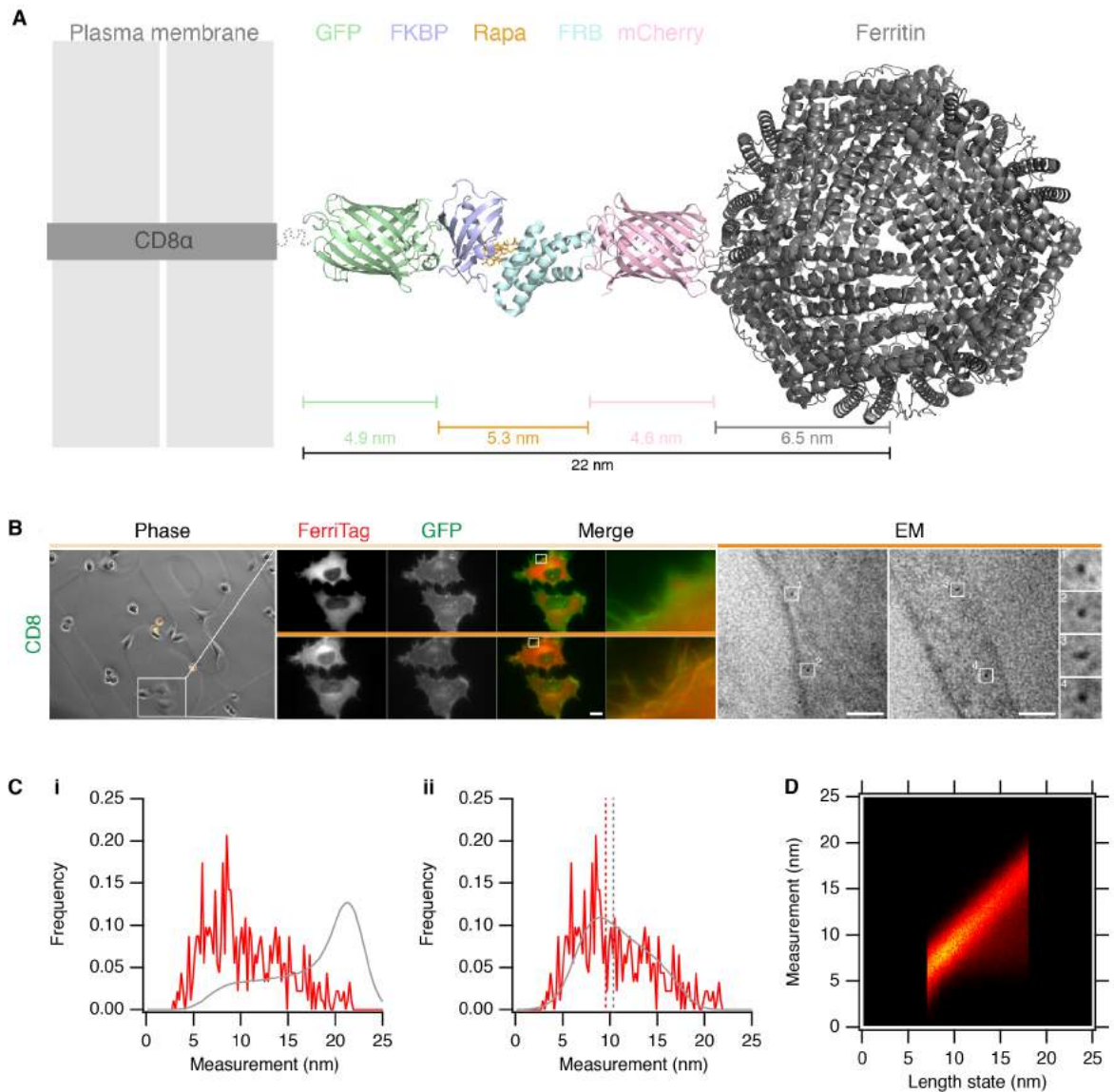
Figure 4.5. The labelling resolution of FerriTagging is approximately 10 nm.

A) Schematic to show the maximum distance FerriTag can be away from the target protein. FerriTag (FRB-mCherry-FTH1:FTL, 1:4) is shown bound to CD8α-GFP-FKBP by rapamycin. Protein domains are organized co-linearly with their long-axis, giving a maxmium length of 22 nm to the centre of the Ferritin particle.

B) Micrographs from FerriTagged CD8α cells which were processed for CLEM. HeLa cells expressing FerriTag (FRB-mCherry-FTH1:FTL, 1:4) (red) and CD8α-GFP-FKBP (green) were first imaged by light microscopy. Rapamycin addition indicated by filled orange bar. The same cell is imaged by electron microscopy and FerriTag particles can be seen decorating the plasma membrane.Two particles per micrograph are shown expanded to the right. Light microscopy scale bar 10 μm and zoom x12. Electron micrograph scale bar 50 nm and zoom x7.25.

C) Histogram of experimental observations (red) with a density function of simulated values overlaid (gray). Distance from the centre of the ferritin particle to the inner membrane was measured. Dotted line indicates the median of the experimental dataset (9.8 nm, $N_{particle}$ = 458). **i)** 22 nm stiff neck simulation. **ii)** Flexible length state simulation. Median value indicated by dashed line (experimental red, Flexible simulation grey).

D) Heat map of the measured distance of FerriTag particle from the plasma membrane as a function of FerriTag length state in the simulation shown in Cii. The median simulated observation underestimates the true length by 11% (mean, 13%).

94

4.7 FerriTag has a high signal-to-noise ratio

The signal-to-noise ratio (SNR) is a measure of sensitivity that compares the level of a desired signal to the level of background noise. For electron microscopy, good SNR is difficult to achieve since heavy-metal staining during sample processing masks the electron density provided by the probe. Samples can be processed without staining, however this compromises the ability to visualize cellular ultrastructure. A CLEM probe that provides high SNR is therefore highly desirable.

To determine the SNR of FerriTag, images taken to measure the labelling resolution from section 4.6 were used, since it was the largest dataset available. The XY coordinates for each FerriTag particle in all electron micrographs were determined. Using these, a 21x21 pixel box centred on each particle was excised (figure 4.6 A) and the image was fitted with a 2D Gaussian function,

$$f(x,y) = z_0 + Aexp\left[\frac{-1}{2(1-cor^2)}\left(\left(\frac{x-x_0}{\sigma_x}\right)^2 + \left(\frac{y-y_0}{\sigma_y}\right)^2 - \frac{2cor(x-x_0)(y-y_0)}{\sigma_x.\sigma_y}\right)\right]$$

where the cross-correlation term, $cor \in [-1, 1]$ (figure 4.6 B). A total of 441 particles were analysed and values for the width in X and Y of each are shown in figure 4.6 C. On average a FerriTag particle was approximately 10 nm in size (figure 4.6 C, red) and had a peak density of around 85 arbitrary units (figure 4.6 C, grey). This information was used to calculate the SNR. SNR is defined as,

$$SNR = \frac{\mu_{signal}}{\sigma_{background}}$$

To calculate μ_{signal}, a 5x5 pixel ROI centred on the x_0 and y_0 values from each fit was used. From the same electron micrograph, $\sigma_{background}$ was calculated from a region that was around 400x400 pixels on average. The background region-of-interest (ROI) was selected mostly inside the cell but also included membrane and some extracellular areas. Grid bars were avoided completely (Figure 4.6 C).

The calculation revealed that FerriTag, using the current processing protocol for CLEM (section 4.3) and manual selection of particles, gives a SNR of approximately 8.7:1 (figure 4.6 F).
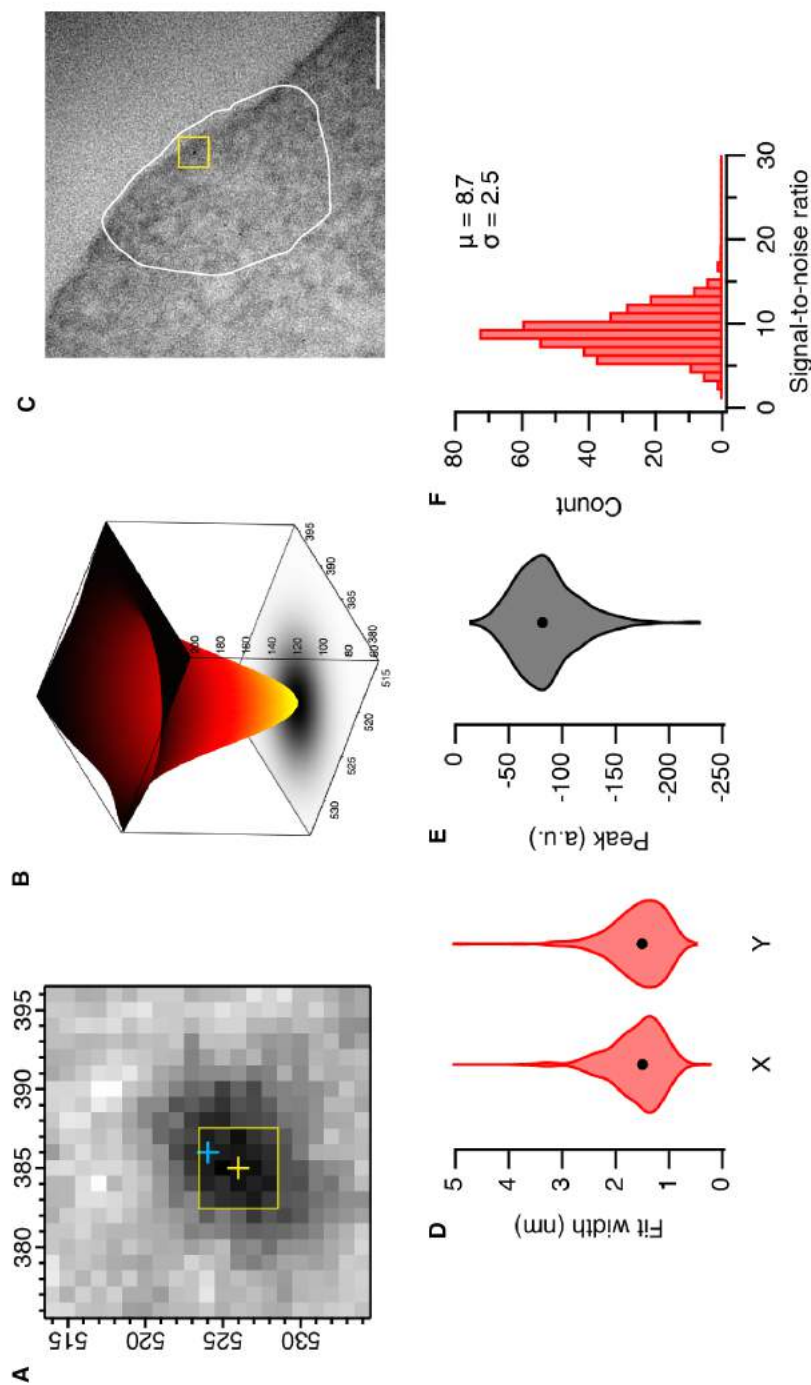
Figure 4.6. Automated fitting in FerriTag images and determination of SNR.
A) A 21x21 pixel excerpt from an electron micrograph containing a ferritin particle in a cell where CD8α was FerriTagged from section 4.5. The location of the centre of the particle was detected manually (blue cross). The X_0 and Y_0 values from each fit (yellow cross) define the centre of an ROI used for measuring the signal of the particle (yellow box). **B)** 3D representation of a 2D Gaussian function that was fitted to the particle shown in A, note the offset of the peak relative to the center of the XY plane. Note, interpolation is used to find the centre of each particle only (yellow arrow) and SNR is calculated from raw pixels. **C)** Representative electron micrograph showing an example background ROI (white outline) from which the SNR was calculated. FerriTag particles shown labeling CD8α at the plama membrane (yellow box). Scale bar 100 nm.**D)** Violin plot showing the fitting of 389 particles. The width in X and Y was approximately 1.6 nm. **E)** Violin plot of the density of the peak of the fit, which was on average -85 arbitrary units. **F)** Histogram of the SNR measured from 389 ferritin particles.

97

4.8 FerriTagging is highly efficient

We now wanted to determine the efficiency of FerriTagging. Prior to the addition of rapamycin, FerriTag is homogeneously distributed throughout the cytoplasm. Induction of heterodimerization by the addition of rapamycin results in FerriTag labelling the protein-of-interest. Whilst we visualize this by light microscopy, we cannot assume that all FerriTag is labelling all of the protein-of-interest. An unbiased quantitative study is therefore required that can assess what concentrations of FerriTag are localised to the target region compared to the non-target region, before and after the addition of rapamycin, in electron micrographs. Since FerriTag provides high SNR (section 4.7, it can be automatically detected by a computer.

Method for automatic detection of FerriTag

First, each electron micrograph is inverted and a 20 pixel mean filtered version is subtracted (Figure4.7 A and B). This removes any background inhomogeneity and equalizes particle detection across the whole image. Particles with a SNR of 3 and a size of 5 are then automatically detected using the `ImageJ` plugin, `ComDet v0.3.5.`However, these basic parameters detected parts of the image that did not look to be true particles. More stringent detection parameters resulted in particles being missed. Further classification was therefore needed to discriminate real particles from spurious detection.

The Z-score of mean intensity of each detection was calculated and its mean intensity was used as the basis for discrimination (Figure 4.7 C). Z score is defined as,

$$z = \frac{x - \mu}{\sigma}$$

where x is the mean intensity of an individual detection, μ and σ are the average

and standard deviation of the intensity of all detections in the image, respectively. In parallel, each micrograph is segmented into three regions (Figure 4.7 D),

1. A membrane zone (white), defined below the plasma membrane, where we would expect bound FerriTag to localise to the target protein,

2. A cytoplasmic zone (grey), where unbound FerriTag would localise,

3. Outside of the cell (black), where no FerriTag should be present.

Therefore, based on the expected localisation of particles, the maximum Z-score of detections outside the cell was used as a lower limit for acceptance and the maximum Z-score of detections in the membrane was taken as the upper limit for acceptance (Figure 4.7 E). This means that all detections outside the cell was excluded and everything intracellular through to the darkest particle at the membrane was kept. The relative densities of accepted particles were then used to calculate the efficiency of FerriTagging by comparing cytoplasmic and membrane regions.

To test the performance of this workflow, a synthetic dataset of randomly distributed particles in an image was generated (Figure 4.7 F). Automatic detection was carried out and the data was plotted (Figure 4.7 G-I). It shows that the workflow can reliably detect particles in images far beyond the number of particles we encounter in real electron micrographs. We can therefore assume each particle is being correctly detected.
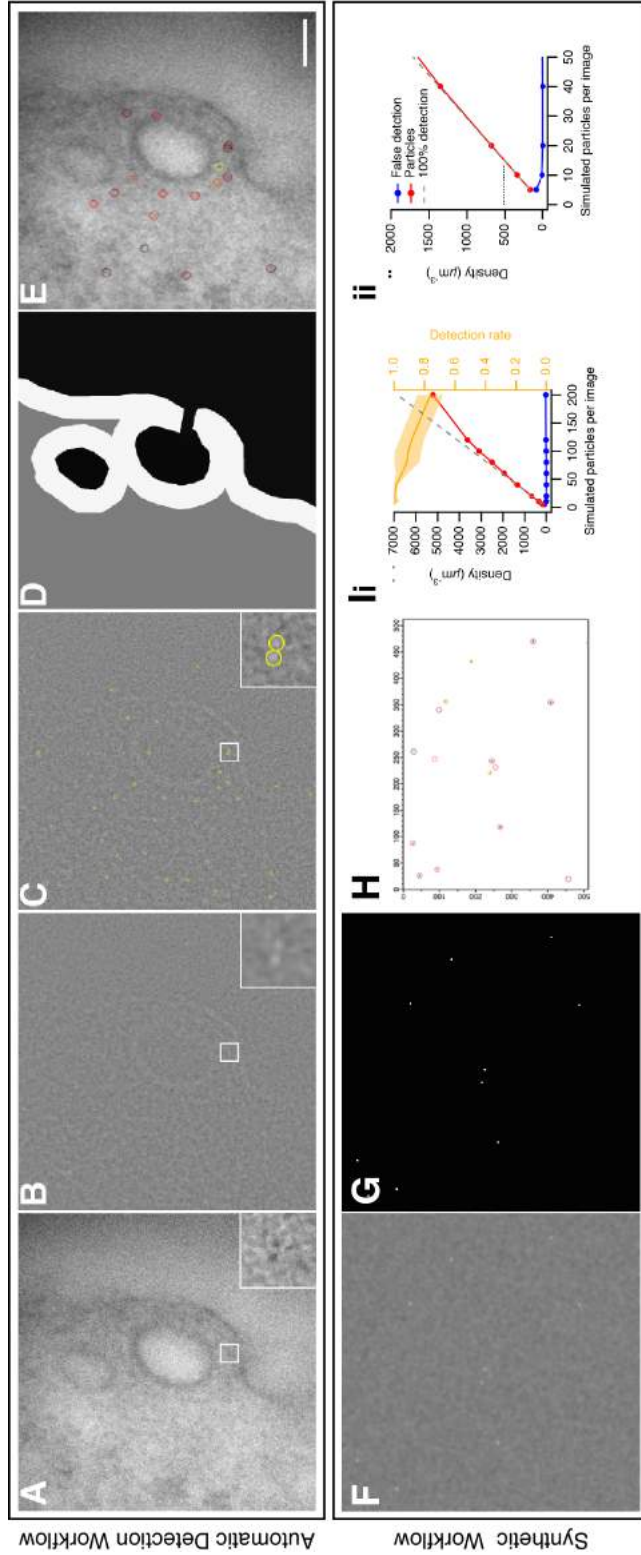
Figure 4.7. Workflow for automatic detection of FerriTag particles in electron micrographs.
A) Representitive electron micrograph of FerriTag at a clathrin-coated pit.
B) Image is inverted and filtered.
C) Detection of particles using ComDet ImageJ plugin with a SNR of 3 and size of 5.
D) The same image is segmented into three regions. A membrane zone (white), cytosol (gray), and cell exterior (black).
E) Discrimination of real particles from spurious detection. Particles accepted as real by the program remain in the image and are color-coded according to the confidence of assignment (black-red-yellow, low-mid-high confidence). Scale bar, 100 nm.
F) Example synthetic image of randomly distributed particles.
G) Ground truth images, highlighting real location of spots.
H) Detection of particles using ComDet ImageJ plugin.
I) Performance testing of automated detection in images with synthetically generated particles. **i)** Density of particles detected (red) is shown as a function of actual particles in the image. Grey broken line indicates perfect detection. False detection (blue) indicates a type I error. Detection rate (orange, right axis) shows the mean ± SD from 12 repetitions for each simulation point. **ii)** an expanded view of the plot to show that a typical image with 500 particles per nm³ (dotted line) is well within the region of optimal detection. Dots show individual particles and bars, mean ± SD.

100

Determining the efficiency of FerriTag

To measure the efficiency of FerriTagging, we compared two datasets to assess the relative density of particles at the membrane and the cytoplasm. For this, we used electron micrographs from cells expressing GFP-FKBP-LCa and FerriTag, with and without (control) the addition of rapamycin, respectively (Figure 4.8 A).

Automatic detection was performed as described above for each dataset. A 50 nm membrane region was used for segmentation to account for the clathrin-coat (approximately 30 nm) and the maximum possible length of a Ferritagged complex (approximately 22 nm). In control samples, a total of 318 particles per μm^3 were detected in the cytoplasm and 592 per μm^3 in the membrane, giving a 1.9 fold enrichment (Figure 4.8 C). In Ferritagged samples, a total of 348 particles per μm^3 were detected in the cytoplasm and 1493 per μm^3 in the membrane, giving a 4.3 fold enrichment. This data gives some indication that FerriTagging of a protein-of-interest represents real labelling, and that unbound FerriTag does not interfere with detection of genuine FerriTag particles. However, It should be realised this software in its current state does pick out many false detections meaning it is still needs work to be used routinely. Furthermore, it is puzzling why more FerriTag particles are being detected in the cytoplasm in plus rapamycin samples compared to control where no rapamycin has been added, despite FerriTag florescence being very similar on average before the addition of rapamycin in both conditions (Figure 4.8 B). This is discussed in section 4.10.
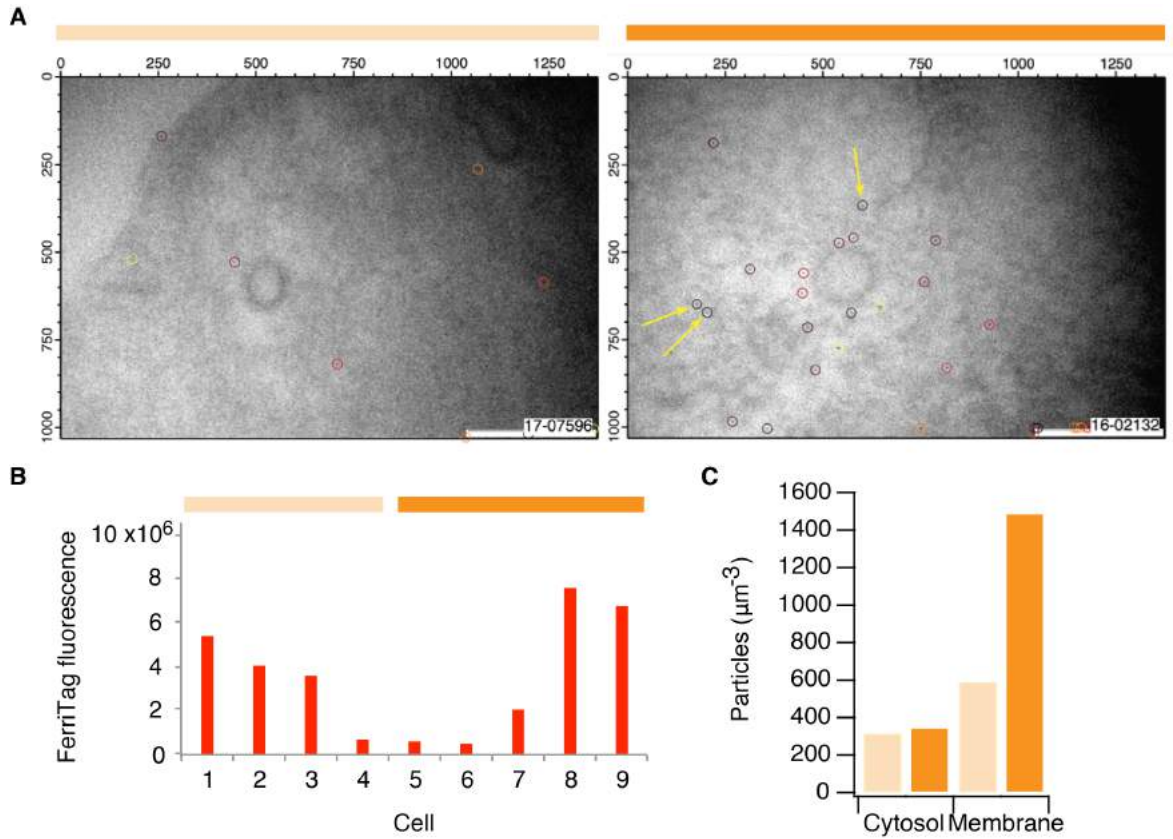
Figure 4.8. Automated detection of FerriTag particles in electron micrographs
A) Representitive electron micrographs to show automatic detection of FerriTag particles in cells expressing GFP-FKBP-LCa and FerriTag. Addition (filled orange bar) or absence (clear orange bar) of rapamycin represents test and control samples respectively. Accepted particles are circled in each image, coloured according to z-score. Likely false detections are highlighted (yellow arrows).
B) FerriTag expression in cells used to perform automated detection of FerriTag particles from A). Intensity calculated from background subtracted integrated density for the whole cell. Mean intensities for no rapamycin (clear orange bar) and plus rapamycin (filled orange bar) are 3.4×10^6 and 3.5×10^6, respectively.
C) Automated quantification of particles at the membrane versus cytosol. No rapamycin addition is shown in clear orange, while rapamycin-treated is shown in dark orange. The densities are taken from the sum of 52 micrographs.

4.9 Contextual nanoscale mapping of HIP1R

We had now developed and characterized FerriTag for CLEM and wanted to apply FerriTagging to a cell biological question. The localization of HIP1R during maturation of a vesicle in clathrin-mediated endocytosis is not well understood, with three competing models presenting different ideas (figure 1.3). To determine its true localization we used FerriTag to perform contextual nanoscale mapping of HIP1R using CLEM.

HeLa cells expressing FerriTag (FRB-mCherry-FTH1: FTL, 1:4) and HIP1R-GFP-FKBP were imaged by live-cell fluorescent light microscopy. Rapamycin induced the heterodimerization of FKBP and FRB domains resulting in FerriTagging of HIP1R. Cells were then processed for electron microscopy as described in section 4.4 and electron micrographs of Ferritagged HIP1R on clathrin-coated pits were acquired (figure 4.9 A). Each micrograph was segmented to highlight the location of each FerriTag particle as well as the plasma membrane profile of the pit. The edges of the pit were also defined, enabling mapping of FerriTgged HIP1R distal to the pit, i.e. in adjacent areas of uncoated plasma membrane (figure 4.9 B). Spatial averaging was then used to plot the distribution of all particles symmetrically about an idealized clathrin-coated pit for visualization (figure 4.9 C).

This revealed three key findings regarding the distribution of HIP1R. 1) HIP1R is homogeneously distributed over the entire crown of the clathrin-coated pit (figure 4.9 C), 2) HIP1R also localizes to distal uncoated regions of the plasma membrane, albeit at a lower density (figure 4.9 C and D), 3) Finally, the distance from Ferritagged HIP1R particles to the plasma membrane was greater at the pit compared to distal uncoated regions, a difference of 10 nm on average (figure 4.9 E). As the C-terminus of HIP1R is Ferritagged and the N-terminus binds the plasma membrane, differences in distance to the membrane most likely correspond to conformational changes of the molecule. This therefore suggests HIP1R, when bound at the pit is in its extended form and in its kinked form at distal uncoated regions of the membrane.
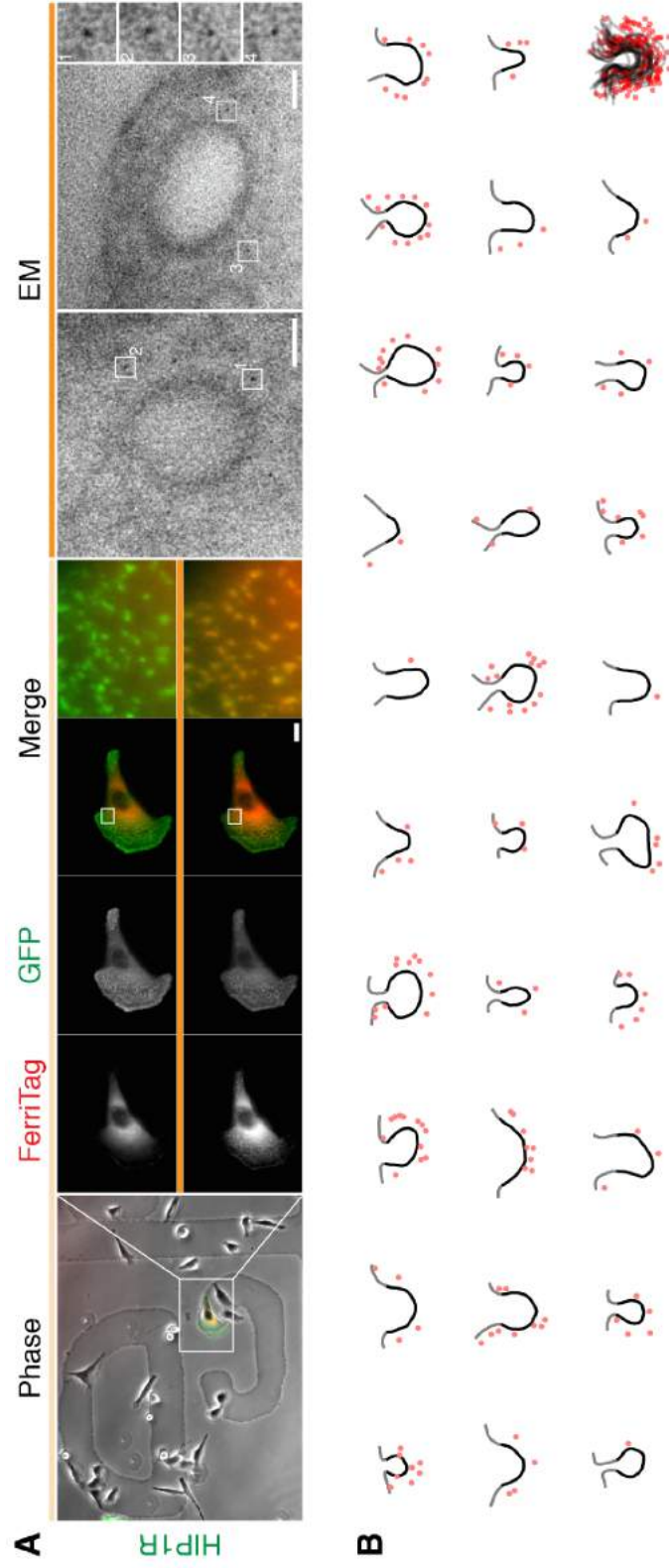
Figure 4.9. Nanoscale mapping of HIP1R

Figure continued over page.
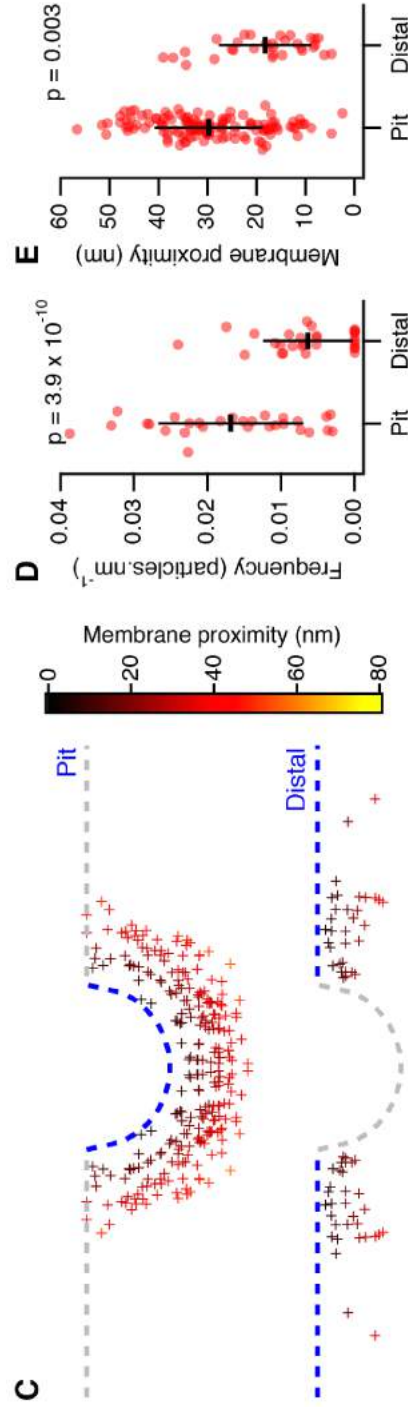
Figure 4.9. Nanoscale mapping of HIP1R

A) Micrographs from FerriTagged HIP1R cells which were processed for CLEM. HeLa cells expressing FerriTag (FRB-mCherry-FTH1:FTL, 1:4) (red) and HIP1R-GFP-FKBP (green) were first imaged by light microscopy. Rapamycin addition indicated by filled orange bar. The same cell is imaged by electron microscopy and FerriTag particles can be seen decorating the clathrin-coated pits. Two particles per micrograph are shown expanded to the right. Light microscopy scale bar 10 μm and zoom x12. Electron micrograph scale bar 50 nm and zoom x7.25.

B) Manually segmented membrane profiles (Black - pit, Gray - distal) and FerriTag particles (red) from HIP1R FerriTag electron micrographs. An aligned overlay of all profiles is shown in the bottom right corner.

C) Spatially averaged representation of HIP1R bound to an idealized clathrin-coated pit (100 nm diam.) determined by position of FerriTag particles in electron micrographs. FerriTag locations are marked by crosses, color-coded by the distance to the plasma membane. Note, that the distribution is symmetrically presented, i.e. each particle appears twice.

D) Scatter dot plot comparing the frequency of FerriTagged-HIP1R particles in the pit or at distal regions. Bars show mean ± SD.

E) Scatter dot plot of the frequency comparing the proximty of FerriTagged-HIP1R particles in the pit or at distal regions. Bars show mean ± SD.

4.10   Discussion

In this chapter, FerriTag was optimised for *correlative light electron microscopy*. We developed a CLEM protocol using FerriTag that is simple and robust. This protocol was applied to a novel cell biological question.

Our approach to load FerriTag with iron under iron-rich conditions had minimal effects on cell viability in HeLa cells. In addition, we believe expression of FerriTag itself will likely buffer the iron supplementation and offset any adverse effects. In other cell types or tissue that are more sensitive to iron levels cell viability will need to be assessed. If iron-loading cells decreases their viability FerriTagging may not be possible.

Using the optimised protocol for CLEM outlined in section 4.3, FerriTag can be used to acutely label proteins with high efficiency and specificity. FerriTag provides electron density that is tightly focussed enabling it to generate a high SNR (8.7:1 (Section 4.7) so it can be easily detected from background in electron micrographs. The SNR was calculated using a large background ROI that contained around 160,000 pixels on average and included cellular structures such as membrane as well as some extracellular area. When a smaller background ROI was used that contained 10,000 pixels and restricted to cytoplasmic areas only, the SNR was 10.8:1, which seemed artificially high. Using a larger ROI therefore gives a more realistic value. A reason why the SNR of FerriTag is high, is due to the minimal staining conditions used in the CLEM protocol (Section 4.3). The heavy metal staining during sample processing was optimised to enable clear visualization of both FerriTag and cellular ultrastructure. This is important to bring context to the localisation of a tagged protein-of-interest and is something other metal-ligand based tags have failed to achieve (Wang et al., 2011; Risco et al., 2012; Morphew et al., 2015). However, more routine processing protocols implement other heavy-metal staining such as uranyl acetate to further increase the contrast of ultrastructure. However this was shown to mask the visualization of FerriTag (Section 4.3). Other processing protocols that have not yet been explored may enhance the better visualisation of FerriTag and are discussed in chapter 5.

The labelling resolution of FerriTag is on the order of 10 nm. This exceeds the capabilities of standard immunogold techniques (approximately 16 nm) (Amiry-Moghaddam and Ottersen, 2013) and methods that use DAB precipitation which have inherent low labelling resolutions due to the diffuse nature of the precipitate they form (Shu et al., 2011; Martell et al., 2012; Lam et al., 2014; Ariotti et al., 2015). Whilst, super-resolution microscopy typically has a spatial resolution of around 10-20 nm it has further error in labelling resolution (depending on the labelling methodology) (Huang et al., 2009; Ma et al., 2017). Though in some specialized cases super-resolution microscopy has reached sub 5 nm and will likely get even better in the future (Schnitzbauer et al., 2017). Although difficult to compare methods directly, FerriTag does have the added benefit of being able to see all structures in the cell whereas super-resolution microscopy is limited to visualizing fluorophores only. This said, super-resolution microscopy does allow thousands of events in many sample to be captured per experiment, where in comparison electron microscopy has very low throughput.

FerriTag can be automatically detecting by a computer using the workflow outlined in section 4.8. However, whilst we can confidently show enrichment of FerriTag particles in plus rapamycin samples compared to control, the computer detection workflow is still very much a work in progress and needs major improvement. The software is prone to error, finding many false detections in electron micrographs that do not represent true FerriTag particles. This limitation is highlighted by the fact we demonstrate detection of more particles in the cytoplasm in plus rapamycin samples compared to control, where instead we would expect to see a decease (Figure 4.7 C). The only other explanation is 1) cytoplasmic clathrin is being Ferritagged which would represent true labelling or 2) more FerriTag has been expressed in plus rapamycin samples and more background is observed. It is hard to prove point 1), as clathrin by itself cannot be visualised directly in-resin by itself, so discerning whether Ferritagged cytoplasmic clathrin represents true labelling is not possible. Fluorescence was calculated in Images used for particle detection to measure FerriTag expression (Figure 4.7 B). Interestingly, the mean values for minus and plus rapamycin samples where very sim-

ilar, suggesting the amount of FerriTag being expressed in cells was also similar. It may therefore be the automated analysis pipeline just detecting more false results in plus rapamycin cells compared to controls. It is clear more development is needed to provide truly accurate, reliable and unbiased detection in this way. Future work will also determine actual false background detections by performing automated analysis on untransfected cells, where no FerriTag is expressed and no detections are expected. This was something that had not been implemented in this work as *correlative* samples were processed in a way where only the cell-of-interest is tracked throughout the entire workflow and no untransfected cells are seen in-resin to image. False detection may also be corrected using *in vitro* approaches. FerriTag could be purified from cells and then blotted on electron microscopy sections that have been processed for CLEM with FerriTagging. An initial image would be taken prior to blotting purified FerriTag and a second image following blotting. Automated analysis would then proceed and the detections from each image compared. FerriTag particles in-resin that do not match the parameters met by blotted FerriTag would be determined false and omitted. In hindsight, a more classical stereological approach should have been implemented to assess the efficiency of FerriTagging, prior to the development of an automated detection pipeline. Briefly, stereology refers to the spatial interpretation of sections to determine the relative labelling intensities confined within set compartments. By counting the amount of FerriTag particles within cytoplasmic and target labelling site areas in electron micrographs, high accuracy comparisons can be made with good statistical accuracy. From this, the amount of FerriTag particles per μm^3 can be estimated and would show how many more particles are found in each compartment between plus and minus rapamycin samples. Following this, segmentation of whole cell volumes could be performed to determine detailed analysis of individual 3D compartments. Whilst this would provide a full representation of the relative labelling intestines throughout the whole sample, this would require much more work than stereological analysis as serial sectioning of whole cells would have to be performed.

It is important to highlight why the SNR parameter (3) for automatic detection is

lower than the calculated SNR value (11) from section 4.7. When a SNR of 11 was used in the automatic detection work flow, the program failed to detect any particles. This was likely due to particles in the the mean filtered version of the image not having a SNR this high. Instead, we found using a size of 5 and SNR of 3 gave reliable detection of true particles and some false positives. Future directions in FerriTag optimisation to create more dense particles, as well as improvements to image analysis will hopefully result in the ability to detect all true particles only. Work is ongoing in the lab to improve computer detection towards this goal.

The high efficiency, specificity, SNR and resolution of FerriTag make it ideal for mapping protein distribution at the nanoscale. We used FerriTag to perform contextual nanoscale mapping of HIP1R in HeLa cells. Three models for its localization and conformation during clathrin-mediated endocytosis have been described (figure 1.3). We propose a model that combines aspects from these previous findings (Figure 4.10 B). We show that HIP1R localizes across the entire clathrin-coated pit and also distal, uncoated regions of the plasma membrane. This finding is contrary to the first model (figure 1.3 A). However this study used an 'unroofing' strategy that likely removes much of the cellular interior including HIP1R, potentially restricting immunogold labelling artificially to the rim of the clathrin-coated pit (Engqvist-Goldstein et al., 2001). Though, this paper does support our observation that HIP1R is found in distal regions, bound to actin cytoskeleton. Whilst our localization data more closely matches model 3 (figure 1.3 C), we also observe conformational differences in HIP1R that are reported in model 2 (figure 1.3 B). We show HIP1R localises more closely to plasma membrane at distal, uncoated regions of the membrane compared to when bound at the pit. From this data we propose the N-terminal ANTH domain of HIP1R associates with the plasma membrane and the C-terminal region THATCH domain binds actin. At distal, uncoated regions of the plasma membrane HIP1R exists in its closed confirmation. Whilst interaction with clathrin encourages it to adopt its extended confirmation providing a link between the clathrin coat and the actin cytoskeleton (Figure 4.10 A and B). This arrangement allows the coat to be anchored against the cytoskeleton while

polymerizing actin provides the force needed to push the clathrin-coated vesicle away from the membrane during maturation. To further confirm this hypothesis, it would be beneficial to also be able to visualise actin to discern its localisation in relation to HIP1R also. This could be achieved using cryo-tomography and a duel labelling experiment where HIP1R is labelled by FerriTag and actin is labelled with metallothionein (Methodology discussed in section 5). Furthermore, to prove this model absolutely and provide a definitive answer to the conformational state of HIP1R, FerriTagging should be performed at another place on the molecule. Ideally the N-terminal ANTH domain of HIP1R would be FerriTagged which would demonstrate that this domain is closer to the membrane around the clathrin-coated pit. However, labelling HIP1R at its N-terminal has the potential to disrupt it normal localisation as it may interfere with its membrane binding properties. If this is the case, it may be possible to incorporate an FKBP domain internally in HIP1R, after the ANTH domain but before the C-terminal and still be able to detect conformational changes using FerriTag.
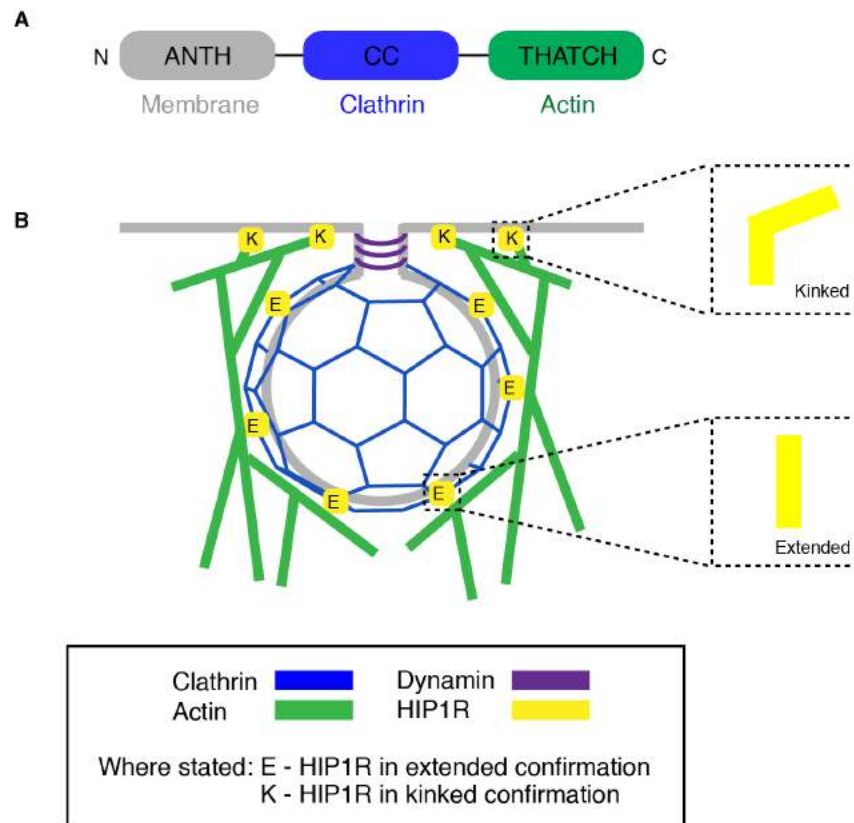
Figure 4.10 Proposed model for HIP1R localization during clathrin mediated endocytosis.
A) Schematic diagram of HIP1R, a rod-shaped molecule with interaction domains for membrane (grey), clathrin (blue) and actin (green).
B) Proposed model of HIP1R arrangement during clathrin-meditated endocytosis to explain our data: HIP1R is in an extended conformation when interacting with membrane, clathrin and actin, and is in a shorter/ kinked conformation when not bound to clathrin at distal regions.

Discussion

This thesis has outlined the initial development of FerriTag as a genetically-encoded tag for *correlative* light electron microscopy, as well as its utility to answer a long-standing question in clathrin-mediated endocytosis.

FerriTag is ready for use in various areas of cell biology. An example would be discovering new proteins that function as inter-microtubule bridge proteins in the mitotic spindle. Currently only the TACC3/ ch-TOG/ clathrin complex has been confirmed, leaving at least 3 more populations with mean lengths ranging from 21.8, to 53.3 nm to be identified (Booth et al., 2011). Previously this task has been challenging, as the only way to directly visualise these structures is by electron microscopy. Immuno-gold labelling can then be performed to localise proteins-of-interest at high-resolution. However, weak fixation is usually necessary to preserve antigenicity, often resulting in compromised ultrastructure and poor microtubule preservation (Section 1.1.1.1). As FerriTag is genetically encoded, no permabilisation of the cell membrane is necessary. Furthermore, it is compatible with high-pressure freezing which would ensure optimal ultrastructual preservation. This would require an optimised methodology which is discussed later. FerriTag therefore provides the ideal method to label candidate proteins and localise them at high resolution to determine whether they are apart of inter-microtubule bridge structures. Another project FerriTag will be useful for is the nanoscale mapping of other clathrin-mediated endocytic proteins, as HIP1R has been shown in this thesis (Section 4.9). This would provide high-resolution contextual insight to where each protein resides, potentially giving novel insight to how they function. Eventually this would create a complete model of all proteins involved in

clathrin-mediated endocytosis.

Whilst the use of FerriTag has the potential to be useful for questions such as these in its current form, there are a number of improvements that could be made. Furthermore, like other genetically-encoded tags for CLEM, FerriTag is not without its limitations.

Improvements

To date, we have only explored the use of FerriTag in cells that transiently express the GFP-FKBP tagged protein-of-interest. Whilst this has not been a problem in our experiments, transient overexpression, in some cases, can create complications with gene dosage, protein folding, complex assembly and downstream regulation (Gibson et al., 2013). To circumvent these issues and enable FerriTagging of proteins at endogenous levels, we plan to use gene-editing technologies to generate cell lines that encode GFP-FKBP tagged proteins (Cox et al., 2015). As proteins are expressed at lower levels in gene-edited cells compared to overexpressed, a foreseeable obstacle will be to optimize heterodimerization using rapamycin, as discussed in section 3.8.

It may be possible to further improve various aspects of FerriTag itself. It is clear we are not labelling all target protein within the cell i.e. there is much more clathrin present on respective structures than what is actually being labelled with FerriTag. This may be due to several factors including, amount of FerriTag made and how much GFP-FKBP target protein is being expressed. Whilst it may be difficult to control the amount of FerriTag made within the cell, more efficient labelling may be achieved by concentrating FerriTagging to a specific area of the cell. In its current form, we are unable to spatially control FerriTagging due to the diffusive nature of the dimerizer (rapamcyin or AP21967). To provide more localised activation we could design an optogentic compatible FerriTag. A candidate system to do this with is UVR8-COP1 as dimerization is irreversible (Huang et al., 2014). However, activation is initiated by UV-B (280 nm) which induces photodamage. Tunable light-inducible dimerisation tags (TULIPs) has been extensively used as an optogenetic dimerizing tool (Strickland

et al., 2012). Briefly, LOVpep, a modified phototrophin 1 light oxygen voltage (LOV) domain can dimerize with an engineered PDZ domain following exposure to blue light (<500 nm). However, LOVpep rapidly dissociates from the PDZ domain which isn't ideal for FerriTag experiments, as a more stable interaction is needed to hold it at the target protein. The CRY2-CIB system would be better suited, due to its slower dissociation rate (around 5 minutes). Here, cryptochrome 2 (CRY2), a light-sensitive photosensory protein can bind cytochromes-interacting basic helix-loop-helix protein 1 (CIB1) following exposure to blue light (470 nm) (Taslimi et al., 2016). As FerriTagging occurs within seconds (Section 3.5), fixation would occur well before the CRY2/CIB domains dissociate from one another, ensuring FerriTag remains bound to the target protein. In addition to improving labelling efficiency it may be possible to further improve the labelling resolution of FerriTag. This could be achieved by redesigning FerriTag and making it smaller. By removing the fluorescent protein i.e. GFP, from the candidate protein, it potentially reduces the labelling resolution by 4.9 nm (Figure 4.5). As we can directly visualise FerriTagging itself, the protein-of-interest does not have to be directly visualised also. In its current form, FerriTag has only been shown to bind iron to generate its electron density. This electron density could be improved by enhancing the iron-loading properties of FerriTag by expressing a mutant form that has been recently shown to bind up to threefold more iron than wildtype mammalian heavy chain ferritin (Matsumoto et al., 2015). In addition, the expression of divalent metal ion transferase 1 (DMT1) could also increase the efficiency of iron import into cells for FerriTag to bind and potentially increase its contrast. (Tabuchi et al., 2002). FerriTag could also be engineered to bind other, more electron dense metal ions including cadmium (Iwahori et al., 2006), silver (Kasyutich et al., 2010) and gold (Fan et al., 2010) which would provide better contrast by electron microscopy.

Further improvement to sample processing and protocol design will enable better visualization of both FerriTag and cellular ultrastructure. Our current processing protocol for CLEM with FerriTag uses an osmium only heavy-metal staining approach following chemical fixation. We are yet to try alternative *en bloc* reagents, concentra-

tions and times of staining or other methods of fixation that could maximize the SNR of FerriTag and improve contrast of ultrastructure in electron micrographs. In addition, we could perform post-staining with heavy metals following initial imaging by electron microscopy to increase the contrast of samples. The same sample would be re-imaged and the tag position correlated across both images. The use of electron tomography may also increase the SNR of FerriTag as well as further improve resolution. This may be performed on section using the current protocol outlined here or under cryo conditions whereby thin whole-cells are directly imaged following cryo-immobilisation (Medalia et al., 2002). To improve preservation of ultrastructure, high-pressure freezing can be performed immediately after FerriTagging. This is something that cannot be achieved by DAB-based probes such as APEX and miniSOG as reaction conditions to generate their precipitate cannot occur under cryo temperatures. This is predicted to not be a problem with FerriTag as iron-loading to generate its electron density is performed before fixation. Following cryo-immobilisation frozen cells can then freeze-substituted and embedded in acrylic resin at low temperature. Samples prepared in this way produce high contrast images of completely unstained resin sections, potentially increasing the SNR of FerriTag. In order to image an individual event by light microscopy and localise the same exact spot by electron microscopy, *correlated* protocols must be performed (section 1.1.2). We could apply the protocol outlined by Kukulski et al. 2011 to do this with FerriTag. The labelling resolution of this protocol using fluorescent proteins alone is on the order of 100 nm. Using this protocol combined with FerriTag would dramatically improve this, resulting in ultra-precise *correlated* electron microscopy. The further addition of super-resolution microscopy to this approach would further increase the precision of correlation (Johnson et al., 2015; Peddie et al., 2017). In addition, other imaging modalities such as Scanning Transmission Electron Microscopy (STEM) or High Angle Annular Dark Field (HAADF) imaging, have not yet been tested which may improve the detection of FerriTag particles in electron micrographs.

As discussed in section 4.10, much more improvement has to made to the automatic

detection workflow (Section 4.8 and this cannot currently be reliably used to determine real from false FerriTag particles. Whilst it may be clear to experienced users that real FerriTag particles can be easily ascertained from electron micrographs, it would be advantageous this was made clear to all. In the fist instance, control experiments could be set up as in section 4.5, which would hopefully make it obvious. If this does not help, the ideal approach would be to create an elemental map using electron energy loss spectroscopy (EELS) or Energy-dispersive X-ray spectroscopy (EDX) which would result in iron-loaded particles being detected. The elemental map can then be overlaid onto the electron micrograph so real iron-loaded FerriTag particles can be easily observed. Combining this data to detect true particles with the automatic detection software would also allow false positive to be excluded from the software pipeline (Figure 4.8), giving a much more accurate dataset to calculate FerriTagging efficiency from (Section 4.8.

Limitations

Despite the many benefits over other genetically-encoded tags for CLEM, FerriTag is not without its limitations. The main one being that it is not possible to tag proteins located inside organelles, as the FRB domain of FerriTag must be able to bind the FKBP domain of the target protein following rapamycin addition. Nevertheless, the user can determine whether successful FerriTagging can be achieved first by light microscopy, before deciding whether to process samples for electron microscopy. This limitation is not a problem for other genetically-encoded tags such as APEX as it is directly fused to the protein-of-interest (Martell et al., 2012).

Another limitation is that FerriTagging may not be compatible for systems that are sensitive to enhanced levels of iron. As FerriTag needs an excess of iron to be visualized readily by electron microscopy, iron-loading needs to be performed. Currently, this is achieved by incubating samples in media supplemented with 1mM $FeSO_4$ for 16 hours. In the future, it may be possible to overcome this live-cell incubation step and instead bind iron to FerriTag following fixation. It has recently been shown Metallothionein can

bind gold following cryo-imobilisation by adding gold salts to the freeze substitution medium (Morphew et al., 2015). Likewise, iron-loading of FerriTag during freeze substitution will be tested. Furthermore, iron-loading may also be achieved on-section by incubating them in solution containing iron, similarly to how post-staining is routinely performed.

Iron-loading and rapamycin treatment may have the potential to induce ultrastructural changes in cells. To date, all work with FerriTag has been performed on ultra-thin sections and whilst no obvious ultrastructural defects are apparent, large volume imaging of whole of cells processed for FerriTagging has not been completed. It would be important to address this potential issue in the future by using large volume techniques such as serial block-face scanning electron microscopy (SBF-SEM) or focussed ion-beam scanning electron microscopy and comparing the effects of iron-loading and rapamycin treated cells with controls.

FerriTag may not be suitable for labelling all proteins, especially those involved in highly dynamic events. Whilst initial FerriTagging occurs quickly following rapamycin addition ($T_{1/2} < 20$ seconds), full labelling is not achieved until around 5 minutes following rapamycin application (Section 3.5). It is therefore likely that FerriTag may not be able to performed on proteins involved in events that occur within a few seconds. To circumvent this issue, it may be possible to perform FerriTagging and fix the sample once the event is captured by live-cell imaging, as colocalisation between FerriTag and the protein-of-interest will be seen. This does rely on the protein-of-interest retaining its normal function, which would have to be assessed case-by-case.

Other applications

FerriTag can also be combined with other genetically-encoded probes including DAB-based and metal-ligand based tags. This will enable multiple protein localization within the same cell, allowing "multicolour" electron microscopy. DAB-based tags create a cloud of electron dense precipitate and will therefore be easily distinguished from FerriTag particles. Discerning FerriTag when in combination with metal-ligand based tags

such as metallothionein, will be more difficult, as both create tightly-focussed particles. However, as FerriTag binds iron and metallothionein binds gold, electron energy loss spectroscopy (EELS) or Energy-dispersive X-ray spectroscopy (EDX) can be performed on-section to create a map of elements within the sample and thus distinguish each tag from one another. Careful controls will need to be put in place to ensure each FerriTag and metallothionein selectively bind a specific electron dense ion, only. As metallothionein can bind an array of different metals, it should be loaded with gold first and then iron-loading of FerriTag, can then proceed. An important consideration to make is how feasible the loading of two heavy metals would be in these experiments as gold salts such as AuCl are particularly unstable in aqueous solutions. Instead more soluble compounds such as AuCl3, KAuCl4 or AuTM (Aurothiomalate) can be tested.

In addition to its role as a genetic tag for CLEM, FerriTag has the potential to be used as a purification tag. Ferritin is superparamagnetic (Jutz et al., 2015). As proteins do not exhibit superparamagnetic behaviour, protein–metal complexes such as ferritin could be used to separate Ferritagged proteins or complexes from other cellular constituents. By harnessing these magnetic properties, it may also be possible to perform direct magnetic manipulation of proteins in living cells. However, the physical limits of the magnetic properties of ferritin have recently been discussed, prompting concern that magnetic manipulation using FerriTag may not be possible (Meister, 2016).

Final conclusions

The motivation behind this thesis aimed to engineer a new CLEM probe that could meet all the criteria set out in section 1.3. Whilst improvements still can be made, FerriTag has already come close to meeting these.

Genetically encoded and non-invasive

FerriTag is genetically-encoded and thus non-invasive (Section 3.4). This allows high-strength fixative to be used and no permabilisation of the cell membrane is required resulting in well preserved samples.

Non-toxic and non-disruptive to cellular processes

FeriTag has the potential to be toxic to cells in two areas of its protocol 1) iron-loading and 2) rapamycin treatment. Iron-loading during sample processing for FerriTag has been shown to be non-toxic to cell viability (Section 4.2). Although the use of rapamycin can induce autophagy related defects over prolonged incubation, rapalog-compatible FerriTag can be used instead if longer experiments are required (Section 3.7). FerriTagging also does not interfere with clathrin and is therefore non-disruptive to its normal function (Section 3.6). Though, this may not be true for all proteins and thus will have to be assessed case-by-case.

Fluorescent and electron-dense

FerriTag is visible by light microscopy as it fused to a fluorescent protein (Section 3.4). It is also electron-dense due to its iron-loaded core, so it can be distinguished again by electron microscopy (Section 4.4).

Tightly focused electron density and good signal:noise ratio

The electron density of FerriTag is tightly focussed which generates a circular particle that can be easily distinguished from background due to its high SNR (Section 4.7).

Robust and reliable methodology

DAB-based CLEM probes such as APEX and miniSOG rely on the user to optimise precipitation and staining conditions to generate their electron density. FerriTag is made in cells and does not rely on the user to optimise processing conditions to generate its electron density. The current CLEM protocol provides consistent results with good visualisation of both FerriTag and cellular ultrastructure (Section4.3). Although, there may be other untested processing workflows that provide much better results, which will be addressed in the future.

Compatible with high-pressure freezing

Currently, DAB-based CLEM probes are not compatible with high-pressure freezing. Although FerriTag has not yet utilized high-pressure freezing to cryo-immobilise the sample, it is predicted to be compatible, given the protocol outlined earlier in this discussion.

It is an exciting time in cell biology with many exciting technologies converging to understand protein function down to the nanoscale. My work has added FerriTag as a useful tool for characterising protein localisation and we hope that its use becomes widespread.

Bibliography

Amiry-Moghaddam, M. and Ottersen, O. P. Immunogold cytochemistry in neuroscience. *Nature Neuroscience*, 16(7):798–804, jun 2013. doi: 10.1038/nn.3418.

Ariotti, N., Hall, T., Rae, J., Ferguson, C., McMahon, K.-A., Martel, N., Webb, R., Webb, R., Teasdale, R., and Parton, R. Modular Detection of GFP-Labeled Proteins for Rapid Screening by Electron Microscopy in Cells and Organisms. *Developmental Cell*, 35(4):513–525, nov 2015. doi: 10.1016/j.devcel.2015.10.016.

Auckland, P., Clarke, N. I., Royle, S. J., and McAinsh, A. D. Congressing kinetochores progressively load Ska complexes to prevent force-dependent detachment. *The Journal of Cell Biology*, 216(6), 2017.

Avinoam, O., Schorb, M., Beese, C. J., Briggs, J. A. G., and Kaksonen, M. Endocytic sites mature by continuous bending and remodeling of the clathrin coat. *Science*, 348(6241):1369–1372, jun 2015. doi: 10.1126/science.aaa9555.

Ballister, E. R., Riegman, M., and Lampson, M. A. Recruitment of Mad1 to metaphase kinetochores is sufficient to reactivate the mitotic checkpoint. *The Journal of Cell Biology*, 204(6), 2014.

Baschong, W. and Stierhof, Y.-D. Preparation, use, and enlargement of ultrasmall gold particles in immunoelectron microscopy. *Microscopy Research and Technique*, 42(1):66–79, jul 1998. doi: 10.1002/(SICI)1097-0029(19980701)42:1<66::AID-JEMT8>3.0.CO;2-P.

Belshaw, P. J., Ho, S. N., Crabtree, G. R., and Schreiber, S. L. Controlling protein association and subcellular localization with a synthetic ligand that induces heterodimerization of proteins. *Proceedings of the National Academy of Sciences of the United States of America*, 93(10):4604–7, may 1996.

Betzig, E., Patterson, G. H., Sougrat, R., Lindwasser, O. W., Olenych, S., Bonifacino, J. S., Davidson, M. W., Lippincott-Schwartz, J., and Hess, H. F. Imaging Intracellular Fluorescent Proteins at Nanometer Resolution. *Science*, 313(5793):1642–1645, sep 2006. doi: 10.1126/science.1127344.

Booth, D. G., Hood, F. E., Prior, I. A., and Royle, S. J. A TACC3/ch-TOG/clathrin complex stabilises kinetochore fibres by inter-microtubule bridging. *The EMBO Journal*, 30(5):906–919, mar 2011. doi: 10.1038/emboj.2011.15.

Boulant, S., Kural, C., Zeeh, J.-C., Ubelmann, F., and Kirchhausen, T. Actin dynamics counteract membrane tension during clathrin-mediated endocytosis. *Nature Cell Biology*, 13(9):1124–1131, aug 2011. doi: 10.1038/ncb2307.

Brach, T., Godlee, C., Moeller-Hansen, I., Boeke, D., and Kaksonen, M. The Initiation of Clathrin-Mediated Endocytosis Is Mechanistically Highly Flexible. 2014. URL http://www.sciencedirect.com/science/article/pii/S0960982214000815.

Cardona, A., Saalfeld, S., Schindelin, J., Arganda-Carreras, I., Preibisch, S., Longair, M., Tomancak, P., Hartenstein, V., and Douglas, R. J. TrakEM2 Software for Neural Circuit Reconstruction. *PLoS ONE*, 7(6):e38011, jun 2012. doi: 10.1371/journal.pone.0038011.

Cheeseman, L. P., Harry, E. F., McAinsh, A. D., Prior, I. A., and Royle, S. J. Specific removal of TACC3-ch-TOG-clathrin at metaphase deregulates kinetochore fiber tension. *Journal of Cell Science*, 126(9):2102–2113, may 2013. doi: 10.1242/jcs.124834.

Clarke, N. I. and Royle, S. J. FerriTag: A Genetically-Encoded Inducible Tag for Correlative Light-Electron Microscopy. *bioRxiv*, 2016.

Cleyrat, C., Darehshouri, A., Steinkamp, M. P., Vilaine, M., Boassa, D., Ellisman, M. H., Hermouet, S., and Wilson, B. S. Mpl traffics to the cell surface through conventional and unconventional routes. *Traffic (Copenhagen, Denmark)*, 15(9):961–82, sep 2014. doi: 10.1111/tra.12185.

Cox, D. B. T., Platt, R. J., and Zhang, F. Therapeutic genome editing: prospects and challenges. *Nature medicine*, 21(2):121–31, feb 2015. doi: 10.1038/nm.3793.

Dannhauser, P. N., Platen, M., B?ning, H., Ungewickell, H., Schaap, I. A., and Ungewickell, E. J. Effect of Clathrin Light Chains on the Stiffness of Clathrin Lattices and Membrane Budding. *Traffic*, 16(5):519–533, may 2015. doi: 10.1111/tra.12263.

Das, S. C., Panda, D., Nayak, D., and Pattnaik, A. K. Biarsenical Labeling of Vesicular Stomatitis Virus Encoding Tetracysteine-Tagged M Protein Allows Dynamic Imaging of M Protein and Virus Uncoating in Infected Cells. *Journal of Virology*, 83(6):2611–2622, mar 2009. doi: 10.1128/JVI.01668-08.

Daumke, O., Roux, A., and Haucke, V. BAR Domain Scaffolds in Dynamin-Mediated Membrane Fission. *Cell*, 156(5):882–892, feb 2014. doi: 10.1016/j.cell.2014.02.017.

de Boer, P., Hoogenboom, J. P., and Giepmans, B. N. G. Correlated light and electron microscopy: ultrastructure lights up! *Nature Methods*, 12(6):503–513, may 2015. doi: 10.1038/nmeth.3400.

Deerinck, T. J., Giepmans, B. N. G., Smarr, B. L., Martone, M. E., and Ellisman, M. H. Light and Electron Microscopic Localization of Multiple Proteins Using Quantum Dots. In *Quantum Dots*, volume 374, pages 43–54. Humana Press, New Jersey, 2007. doi: 10.1385/1-59745-369-2: 43. URL `http://www.ncbi.nlm.nih.gov/pubmed/17237528http://link.springer.com/10.1385/1-59745-369-2:43`.

Diestra, E., Fontana, J., Guichard, P., Marco, S., and Risco, C. Visualization of proteins in intact cells with a clonable tag for electron microscopy. *Journal of Structural Biology*, 165(3):157–168, mar 2009. doi: 10.1016/j.jsb.2008.11.009.

Doherty, G. J. and McMahon, H. T. Mechanisms of Endocytosis. *Annual Review of Biochemistry*, 78 (1):857–902, jun 2009. doi: 10.1146/annurev.biochem.78.081307.110540.

Ellisman, M. H., Deerinck, T. J., Shu, X., and Sosinsky, G. E. Picking faces out of a crowd: genetic labels for identification of proteins in correlated light and electron microscopy imaging. *Methods in cell biology*, 111:139–55, 2012. doi: 10.1016/B978-0-12-416026-2.00008-X.

Engqvist-Goldstein, A. E. Y. and Drubin, D. G. Actin assembly and endocytosis: from yeast to mammals. *Annual review of cell and developmental biology*, 19(1):287–332, nov 2003. doi: 10.1146/annurev.cellbio.19.111401.093127.

Engqvist-Goldstein, s. E., Warren, R. A., Kessels, M. M., Keen, J. H., Heuser, J., and Drubin, D. G. The actin-binding protein Hip1R associates with clathrin during early stages of endocytosis and promotes clathrin assembly in vitro. *The Journal of Cell Biology*, 154(6):1209–1224, sep 2001. doi: 10.1083/jcb.200106089.

Fan, R., Chew, S. W., Cheong, V. V., and Orner, B. P. Fabrication of Gold Nanoparticles Inside Unmodified Horse Spleen Apoferritin. *Small*, 6(14):1483–1487, jul 2010. doi: 10.1002/smll.201000457.

Ferguson, S. M. and De Camilli, P. Dynamin, a membrane-remodelling GTPase. *Nature Reviews Molecular Cell Biology*, 13(2):75, jan 2012. doi: 10.1038/nrm3266.

Fernndez de Castro, I., Sanz-S?nchez, L., and Risco, C. Metallothioneins for Correlative Light and Electron Microscopy. In *Methods in cell biology*, volume 124, pages 55–70. 2014. doi: 10.1016/B978-0-12-801075-4.00003-3. URL `http://www.ncbi.nlm.nih.gov/pubmed/25287836http://linkinghub.elsevier.com/retrieve/pii/B9780128010754000033`.

Fulton, A. B. How crowded is the cytoplasm? *Cell*, 30(2):345–7, sep 1982.

Gaietta, G., Deerinck, T. J., Adams, S. R., Bouwer, J., Tour, O., Laird, D. W., Sosinsky, G. E., Tsien, R. Y., and Ellisman, M. H. Multicolor and Electron Microscopic Imaging of Connexin Trafficking. *Science*, 296(5567):503–507, apr 2002. doi: 10.1126/science.1068793.

Gibson, T. J., Seiler, M., and Veitia, R. A. The transience of transient overexpression. *Nature Methods*, 10(8):715–721, jul 2013. doi: 10.1038/nmeth.2534.

Giepmans, B. N. G., Deerinck, T. J., Smarr, B. L., Jones, Y. Z., and Ellisman, M. H. Correlated light and electron microscopic imaging of multiple endogenous proteins using Quantum dots. *Nature Methods*, 2(10):743–749, sep 2005. doi: 10.1038/nmeth791.

Godlee, C. and Kaksonen, M. From uncertain beginnings: Initiation mechanisms of clathrin-mediated endocytosis. *The Journal of Cell Biology*, 203(5), 2013.

Graham, L. and Orenstein, J. M. Processing tissue and cells for transmission electron microscopy in diagnostic pathology and research. *Nature Protocols*, 2(10):2439–2450, oct 2007. doi: 10.1038/nprot.2007.304.

Grassart, A., Cheng, A. T., Hong, S. H., Zhang, F., Zenzer, N., Feng, Y., Briner, D. M., Davis, G. D., Malkov, D., and Drubin, D. G. Actin and dynamin2 dynamics and interplay during clathrin-mediated endocytosis. *The Journal of Cell Biology*, 205(5), 2014.

Greener, T., Zhao, X., Nojima, H., Eisenberg, E., and Greene, L. E. Role of cyclin G-associated kinase in uncoating clathrin-coated vesicles from non-neuronal cells. *The Journal of biological chemistry*, 275(2):1365–70, jan 2000.

Griffin, B. A., Adams, S. R., and Tsien, R. Y. Specific covalent labeling of recombinant protein molecules inside live cells. *Science (New York, N.Y.)*, 281(5374):269–72, jul 1998.

Griffiths, G. and Lucocq, J. M. Antibodies for immunolabeling by light and electron microscopy: not for the faint hearted. *Histochemistry and cell biology*, 142(4):347–60, oct 2014. doi: 10.1007/s00418-014-1263-5.

Guan, R., Han, D., Harrison, S. C., Kirchhausen, T., and Kirchhausen, T. Structure of the PTEN-like Region of Auxilin, a Detector of Clathrin-Coated Vesicle Budding. *Structure*, 18(9):1191–1198, sep 2010. doi: 10.1016/j.str.2010.06.016.

Hanker, J. S. Osmiophilic reagents in electronmicroscopic histocytochemistry. *Progress in histochemistry and cytochemistry*, 12(1):1–85, 1979.

Heiligenstein, X., Heiligenstein, J., Delevoye, C., Hurbain, I., Bardin, S., Paul-Gilloteaux, P., Sengmanivong, L., R?gnier, G., Salamero, J., Antony, C., and Raposo, G. The CryoCapsule: Simplifying Correlative Light to Electron Microscopy. *Traffic*, 15(6):700–716, jun 2014. doi: 10.1111/tra.12164.

Heuser, J. Three-dimensional visualization of coated vesicle formation in fibroblasts. *The Journal of cell biology*, 84(3):560–83, mar 1980.

Hirst, J., Edgar, J. R., Borner, G. H. H., Li, S., Sahlender, D. A., Antrobus, R., and Robinson, M. S. Contributions of epsinR and gadkin to clathrin-mediated intracellular trafficking. *Molecular biology of the cell*, 26(17):3085–103, sep 2015. doi: 10.1091/mbc.E15-04-0245.

Hodgson, L., Tavaré, J., and Verkade, P. Development of a quantitative Correlative Light Electron Microscopy technique to study GLUT4 trafficking. *Protoplasma*, 251(2):403–416, mar 2014. doi: 10.1007/s00709-013-0597-5.

Huang, B., Bates, M., and Zhuang, X. Super-resolution fluorescence microscopy. *Annual review of biochemistry*, 78:993–1016, 2009. doi: 10.1146/annurev.biochem.77.061906.092014.

Huang, X., Yang, P., Ouyang, X., Chen, L., and Deng, X. W. Photoactivated UVR8-COP1 Module Determines Photomorphogenic UV-B Signaling Output in Arabidopsis. *PLoS Genetics*, 10(3): e1004218, mar 2014. doi: 10.1371/journal.pgen.1004218.

Hurtley, S. Location, Location, Location. *Science*, 326(5957):1205–1205, nov 2009. doi: 10.1126/science.326.5957.1205.

Iordanova, B., Robison, C. S., and Ahrens, E. T. Design and characterization of a chimeric ferritin with enhanced iron loading and transverse NMR relaxation rate. *Journal of biological inorganic chemistry : JBIC : a publication of the Society of Biological Inorganic Chemistry*, 15(6):957–65, aug 2010. doi: 10.1007/s00775-010-0657-7.

Iwahori, K., Morioka, T., and Yamashita, I. The optimization of CdSe nanoparticles synthesis in the apoferritin cavity. *physica status solidi (a)*, 203(11):2658–2661, sep 2006. doi: 10.1002/pssa.200669531.

Jauregui, H. O., Bradford, W. D., Arstila, A. U., Kinney, T. D., and Trump, B. F. Iron metabolism and cell membranes. III. Iron-induced alterations in HeLa cells. *The American journal of pathology*, 80(1):33–52, jul 1975.

Johnson, E., Seiradake, E., Jones, E. Y., Davis, I., Gr?newald, K., and Kaufmann, R. Correlative in-resin super-resolution and electron microscopy using standard fluorescent proteins. *Scientific Reports*, 5(1):9583, aug 2015. doi: 10.1038/srep09583.

Jutz, G., van Rijn, P., Santos Miranda, B., and Böker, A. Ferritin: a versatile building block for bionanotechnology. *Chemical reviews*, 115(4):1653–701, feb 2015. doi: 10.1021/cr400011b.

Kaksonen, M., Toret, C. P., and Drubin, D. G. Harnessing actin dynamics for clathrin-mediated endocytosis. *Nature Reviews Molecular Cell Biology*, 7(6):404–414, jun 2006. doi: 10.1038/nrm1940.

Kasyutich, O., Ilari, A., Fiorillo, A., Tatchev, D., Hoell, A., and Ceci, P. Silver Ion Incorporation and Nanoparticle Formation inside the Cavity of <i>Pyrococcus furiosus</i> Ferritin: Structural and Size-Distribution Analyses. *Journal of the American Chemical Society*, 132(10):3621–3627, mar 2010. doi: 10.1021/ja910918b.

Keen, J. H., Gaidarov, I., Santini, F., and Warren, R. A. Spatial control of coated-pit dynamics in living cells. *Nature Cell Biology*, 1(1):1–7, may 1999. doi: 10.1038/8971.

Kelly, B. T., Owen, D. J., Jodi Nunnari, b. M., and Nichols, B. Endocytic sorting of transmembrane protein cargo This review comes from a themed issue on Membranes and organelles Edited. *Current Opinion in Cell Biology*, 23:404–412, 2011. doi: 10.1016/j.ceb.2011.03.004.

Koning, R. I., Faas, F. G., Boonekamp, M., de Visser, B., Janse, J., Wiegant, J. C., de Breij, A., Willemse, J., Nibbering, P. H., Tanke, H. J., and Koster, A. J. MAVIS: An integrated system for live microscopy and vitrification. *Ultramicroscopy*, 143:67–76, aug 2014. doi: 10.1016/j.ultramic. 2013.10.007.

Kukulski, W., Schorb, M., Welsch, S., Picco, A., Kaksonen, M., and Briggs, J. A. Correlated fluorescence and 3D electron microscopy with high sensitivity and spatial precision. *The Journal of Cell Biology*, 192(1):111–119, jan 2011. doi: 10.1083/jcb.201009037.

Kukulski, W., Schorb, M., Welsch, S., Picco, A., Kaksonen, M., and Briggs, J. A. Precise, Correlated Fluorescence Microscopy and Electron Tomography of Lowicryl Sections Using Fluorescent Fiducial Markers. In *Methods in cell biology*, volume 111, pages 235–257. 2012. doi: 10.1016/ B978-0-12-416026-2.00013-3. URL http://www.ncbi.nlm.nih.gov/pubmed/22857932http:// linkinghub.elsevier.com/retrieve/pii/B9780124160262000133.

Kuzmich, A. I., Vvedenskii, A. V., Kopantzev, E. P., and Vinogradova, T. V. Quantitative comparison of gene co-expression in a bicistronic vector harboring IRES or coding sequence of porcine teschovirus 2A peptide. *Russian Journal of Bioorganic Chemistry*, 39(4):406–416, jul 2013. doi: 10.1134/S1068162013040122.

Lam, S. S., Martell, J. D., Kamer, K. J., Deerinck, T. J., Ellisman, M. H., Mootha, V. K., and Ting, A. Y. Directed evolution of APEX2 for electron microscopy and proximity labeling. *Nature Methods*, 12(1):51–54, nov 2014. doi: 10.1038/nmeth.3179.

Laplante, M. and Sabatini, D. M. mTOR signaling at a glance. *Journal of Cell Science*, 122(20), 2009.

Le Clainche, C., Pauly, B. S., Zhang, C. X., Engqvist-Goldstein, s. E. Y., Cunningham, K., and Drubin, D. G. A Hip1R/cortactin complex negatively regulates actin assembly associated with endocytosis. *The EMBO Journal*, 26(5):1199–1210, mar 2007. doi: 10.1038/sj.emboj.7601576.

Leeson, C. R. and Leeson, T. S. An Unusual Arrangement of Ribosomes in Mesenchymal Cells. *Journal of Chemical Biology*, 24(2):324–328, 1965.

Li, D., Shao, L., Chen, B.-C., Zhang, X., Zhang, M., Moses, B., Milkie, D. E., Beach, J. R., Hammer, J. A., Pasham, M., Kirchhausen, T., Baird, M. A., Davidson, M. W., Xu, P., and Betzig, E. Extended-resolution structured illumination imaging of endocytic and cytoskeletal dynamics. *Science*, 349(6251):aab3500–aab3500, aug 2015. doi: 10.1126/science.aab3500.

Licitra, E. J. and Liu, J. O. A three-hybrid system for detecting small ligand-protein receptor interactions. *Proceedings of the National Academy of Sciences of the United States of America*, 93(23): 12817–21, nov 1996.

Liu, J., Farmer, J. D., Lane, W. S., Friedman, J., Weissman, I., and Schreiber, S. L. Calcineurin is a common target of cyclophilin-cyclosporin A and FKBP-FK506 complexes. *Cell*, 66(4):807–815, aug 1991. doi: 10.1016/0092-8674(91)90124-H.

Loerke, D., Mettlen, M., Schmid, S. L., and Danuser, G. Measuring the Hierarchy of Molecular Events During Clathrin-Mediated Endocytosis. *Traffic*, 12(7):815–825, jul 2011. doi: 10.1111/j.1600-0854.2011.01197.x.

Ludwig, A., Howard, G., Mendoza-Topaz, C., Deerinck, T., Mackey, M., Sandin, S., Ellisman, M. H., and Nichols, B. J. Molecular Composition and Ultrastructure of the Caveolar Coat Complex. *PLoS Biology*, 11(8):e1001640, aug 2013. doi: 10.1371/journal.pbio.1001640.

Ma, H., Fu, R., Xu, J., and Liu, Y. A simple and cost-effective setup for super-resolution localization microscopy. *Scientific Reports*, 7(1):1542, dec 2017. doi: 10.1038/s41598-017-01606-6.

Magidson, V., He, J., Ault, J. G., O?Connell, C. B., Yang, N., Tikhonenko, I., McEwen, B. F., Sui, H., and Khodjakov, A. Unattached kinetochores rather than intrakinetochore tension arrest mitosis in taxol-treated cells. *The Journal of Cell Biology*, 212(3):307–319, feb 2016. doi: 10.1083/jcb.201412139.

Mahamid, J., Pfeffer, S., Schaffer, M., Villa, E., Danev, R., Kuhn Cuellar, L., Forster, F., Hyman, A. A., Plitzko, J. M., and Baumeister, W. Visualizing the molecular sociology at the HeLa cell nuclear periphery. *Science*, 351(6276):969–972, feb 2016. doi: 10.1126/science.aad8857.

Manna, P. T., Gadelha, C., Puttick, A. E., and Field, M. C. ENTH and ANTH domain proteins participate in AP2-independent clathrin-mediated endocytosis. *Journal of Cell Science*, 128(11), 2015.

Maranto, A. R. Neuronal mapping: a photooxidation reaction makes Lucifer yellow useful for electron microscopy. *Science (New York, N.Y.)*, 217(4563):953–5, sep 1982.

Martell, J. D., Deerinck, T. J., Sancak, Y., Poulos, T. L., Mootha, V. K., Sosinsky, G. E., Ellisman, M. H., and Ting, A. Y. Engineered ascorbate peroxidase as a genetically encoded reporter for electron microscopy. *Nature biotechnology*, 30(11):1143–8, nov 2012.

Martin, B. R., Giepmans, B. N. G., Adams, S. R., and Tsien, R. Y. Mammalian cell-based optimization of the biarsenical-binding tetracysteine motif for improved fluorescence and affinity. *Nature biotechnology*, 23(10):1308–14, oct 2005. doi: 10.1038/nbt1136.

Masuda, T., Goto, F., Yoshihara, T., and Mikami, B. The universal mechanism for iron translocation to the ferroxidase site in ferritin, which is mediated by the well conserved transit site. *Biochemical and biophysical research communications*, 400(1):94–9, sep 2010. doi: 10.1016/j.bbrc.2010.08.017.

Matsumoto, Y., Chen, R., Anikeeva, P., and Jasanoff, A. Engineering intracellular biomineralization and biosensing by a magnetic protein. *Nature Communications*, 6(1):8721, dec 2015. doi: 10.1038/ncomms9721.

McDonald, K. and Webb, R. Freeze substitution in 3 hours or less. *Journal of Microscopy*, 243(3): 227–233, sep 2011. doi: 10.1111/j.1365-2818.2011.03526.x.

McDonald, K. L., Morphew, M., Verkade, P., and M?ller-Reichert, T. Recent Advances in High-Pressure Freezing. In *Methods in molecular biology (Clifton, N.J.)*, volume 369, pages 143–173. 2007. doi: 10.1007/978-1-59745-294-6_8. URL `http://www.ncbi.nlm.nih.gov/pubmed/17656750http://link.springer.com/10.1007/978-1-59745-294-6{_}8`.

McMahon, H. T. and Boucrot, E. Molecular mechanism and physiological functions of clathrin-mediated endocytosis. *Nature Reviews Molecular Cell Biology*, 12(8):517–533, jul 2011. doi: 10.1038/nrm3151.

Medalia, O., Weber, I., Frangakis, A. S., Nicastro, D., Gerisch, G., and Baumeister, W. Macromolecular architecture in eukaryotic cells visualized by cryoelectron tomography. *Science (New York, N.Y.)*, 298(5596):1209–13, nov 2002. doi: 10.1126/science.1076184.

Meister, M. Physical limits to magnetogenetics. *eLife*, 5, aug 2016. doi: 10.7554/eLife.17210.

Miyamoto, T., DeRose, R., Suarez, A., Ueno, T., Chen, M., Sun, T.-p., Wolfgang, M. J., Mukherjee, C., Meyers, D. J., and Inoue, T. Rapid and orthogonal logic gating with a gibberellin-induced dimerization system. *Nature chemical biology*, 8(5):465–70, mar 2012. doi: 10.1038/nchembio.922.

Moor, H. Theory and Practice of High Pressure Freezing. In *Cryotechniques in Biological Electron Microscopy*, pages 175–191. Springer Berlin Heidelberg, Berlin, Heidelberg, 1987. doi: 10.1007/978-3-642-72815-0_8. URL `http://www.springerlink.com/index/10.1007/978-3-642-72815-0{_}8`.

Moor, H. and Mühlethaler, K. Fine Structure In Frozen-Etched Yeast Cells. *The Journal of cell biology*, 17(3):609–28, jun 1963.

Morphew, M., O'toole, E., Page, C., Pagratis, M., Meehl, J., Giddings, T., Gardner, J., Ackerson, C., Jaspersen, S., Winey, M., Hoenger, A., and Mcintosh, J. Metallothionein as a clonable tag for protein localization by electron microscopy of cells. *Journal of Microscopy*, 260(1):20–29, oct 2015. doi: 10.1111/jmi.12262.

Motley, A., Bright, N. A., Seaman, M. N., and Robinson, M. S. Clathrin-mediated endocytosis in AP-2–depleted cells. *The Journal of Cell Biology*, 162(5):909–918, sep 2003. doi: 10.1083/jcb.200305145.

Müller-Reichert, T. and Verkade, P. Introduction to correlative light and electron microscopy. In *Methods in cell biology*, volume 111, pages xvii–xix. 2012. doi: 10.1016/B978-0-12-416026-2.03001-6. URL `http://www.ncbi.nlm.nih.gov/pubmed/22857938`.

Myasnikov, A. G., Kundhavai Natchiar, S., Nebout, M., Hazemann, I., Imbert, V., Khatter, H., Peyron, J.-F., and Klaholz, B. P. Structure-function insights reveal the human ribosome as a cancer target for antibiotics. *Nature Communications*, 7:12856, sep 2016. doi: 10.1038/ncomms12856.

Nakatsu, F., Perera, R. M., Lucast, L., Zoncu, R., Domin, J., Gertler, F. B., Toomre, D., and De Camilli, P. The inositol 5-phosphatase SHIP2 regulates endocytic clathrin-coated pit dynamics. *The Journal of Cell Biology*, 190(3), 2010.

Nisman, R., Dellaire, G., Ren, Y., Li, R., and Bazett-Jones, D. P. Application of quantum dots as probes for correlative fluorescence, conventional, and energy-filtered transmission electron microscopy. *The journal of histochemistry and cytochemistry : official journal of the Histochemistry Society*, 52(1):13–8, jan 2004. doi: 10.1177/002215540405200102.

Nixon, F. M., Honnor, T. R., Clarke, N. I., Starling, G. P., Beckett, A. J., Johansen, A. M., Brettschneider, J. A., Prior, I. A., and Royle, S. J. Microtubule organization within mitotic spindles revealed by serial block face scanning electron microscopy and image analysis. *Journal of Cell Science*, 130(10), 2017.

Nunez, D., Antonescu, C., Mettlen, M., Liu, A., Schmid, S. L., Loerke, D., and Danuser, G. Hotspots Organize Clathrin-Mediated Endocytosis by Efficient Recruitment and Retention of Nucleating Resources. *Traffic*, 12(12):1868–1878, dec 2011. doi: 10.1111/j.1600-0854.2011.01273.x.

Olmos, Y., Hodgson, L., Mantell, J., Verkade, P., and Carlton, J. G. ESCRT-III controls nuclear envelope reformation. *Nature*, 522(7555):236–239, jun 2015. doi: 10.1038/nature14503.

Ormö, M., Cubitt, A. B., Kallio, K., Gross, L. A., Tsien, R. Y., and Remington, S. J. Crystal structure of the Aequorea victoria green fluorescent protein. *Science (New York, N.Y.)*, 273(5280):1392–5, sep 1996.

Paez-Segala, M. G., Sun, M. G., Shtengel, G., Viswanathan, S., Baird, M. A., Macklin, J. J., Patel, R., Allen, J. R., Howe, E. S., Piszczek, G., Hess, H. F., Davidson, M. W., Wang, Y., and Looger, L. L. Fixation-resistant photoactivatable fluorescent proteins for CLEM. *Nature Methods*, 12(3): 215–218, jan 2015. doi: 10.1038/nmeth.3225.

Paul-Gilloteaux, P., Heiligenstein, X., Belle, M., Domart, M.-C., Larijani, B., Collinson, L., Raposo, G., and Salamero, J. eC-CLEM: flexible multidimensional registration software for correlative microscopies. *Nature Methods*, 14(2):102–103, jan 2017. doi: 10.1038/nmeth.4170.

Peddie, C. J., Blight, K., Wilson, E., Melia, C., Marrison, J., Carzaniga, R., Domart, M. C., O'Toole, P., Larijani, B., and Collinson, L. M. Correlative and integrated light and electron microscopy of in-resin GFP fluorescence, used to localise diacylglycerol in mammalian cells. *Ultramicroscopy*, 143: 3–14, 2014. doi: 10.1016/j.ultramic.2014.02.001.

Peddie, C. J., Domart, M.-C., Snetkov, X., O'Toole, P., Larijani, B., Way, M., Cox, S., and Collinson, L. M. Correlative super-resolution fluorescence and electron microscopy using conventional fluorescent proteins in vacuo. *Journal of Structural Biology*, 199(2):120–131, aug 2017. doi: 10.1016/J.JSB.2017.05.013.

Porstmann, T. and Kiessig, S. T. Enzyme immunoassay techniques. An overview. *Journal of immunological methods*, 150(1-2):5–21, jun 1992.

Pucadyil, T. J. and Holkar, S. S. Comparative analysis of adaptor-mediated clathrin assembly reveals general principles for adaptor clustering. *Molecular biology of the cell*, 27(20):3156–3163, oct 2016. doi: 10.1091/mbc.E16-06-0399.

Putyrski, M. and Schultz, C. Protein translocation as a tool: The current rapamycin story. *FEBS Letters*, 586(15):2097–2105, jul 2012. doi: 10.1016/j.febslet.2012.04.061.

Rhee, H.-W., Zou, P., Udeshi, N. D., Martell, J. D., Mootha, V. K., Carr, S. A., and Ting, A. Y. Proteomic Mapping of Mitochondria in Living Cells via Spatially Restricted Enzymatic Tagging. *Science*, 339(6125):1328–1331, mar 2013. doi: 10.1126/science.1230593.

Risco, C., Sanmart?n-Conesa, E., Tzeng, W.-P., Frey, T., Seybold, V., and De?Groot, R. Specific, Sensitive, High-Resolution Detection of Protein Molecules in Eukaryotic Cells Using Metal-Tagging Transmission Electron Microscopy. *Structure*, 20(5):759–766, may 2012. doi: 10.1016/j.str.2012.04.001.

Rivera, V. M., Clackson, T., Natesan, S., Pollock, R., Amara, J. F., Keenan, T., Magari, S. R., Phillips, T., Courage, N. L., Cerasoli, F., Holt, D. A., and Gilman, M. A humanized system for pharmacologic control of gene expression. *Nature Medicine*, 2(9):1028–1032, sep 1996. doi: 10.1038/nm0996-1028.

Robinson, C. V., Sali, A., and Baumeister, W. The molecular sociology of the cell. *Nature*, 450(7172): 973–982, dec 2007. doi: 10.1038/nature06523.

Robinson, M. S., Sahlender, D. A., and Foster, S. D. Rapid inactivation of proteins by rapamycin-induced rerouting to mitochondria. *Developmental cell*, 18(2):324–31, feb 2010. doi: 10.1016/j.devcel.2009.12.015.

Roth, T. F. and Porter, K. R. Yolk Protein Uptake in the Oocyte of the Mosquito Aedes Agypti. L. *The Journal of cell biology*, 20:313–32, feb 1964.

Royle, S. J. Protein adaptation: mitotic functions for membrane trafficking proteins. *Nature Reviews Molecular Cell Biology*, 14(9):592–599, aug 2013. doi: 10.1038/nrm3641.

Schnitzbauer, J., Strauss, M. T., Schlichthaerle, T., Schueder, F., and Jungmann, R. Super-resolution microscopy with DNA-PAINT. *Nature Protocols*, 12(6):1198–1228, may 2017. doi: 10.1038/nprot.2017.024.

Schorb, M., Gaechter, L., Avinoam, O., Sieckmann, F., Clarke, M., Bebeacua, C., Bykov, Y. S., Sonnen, A. F.-P., Lihl, R., and Briggs, J. A. New hardware and workflows for semi-automated correlative cryo-fluorescence and cryo-electron microscopy/tomography. *Journal of Structural Biology*, 197(2):83–93, feb 2017. doi: 10.1016/j.jsb.2016.06.020.

Shaner, N. C., Steinbach, P. A., and Tsien, R. Y. A guide to choosing fluorescent proteins. *Nature Methods*, 2(12):905–909, dec 2005. doi: 10.1038/nmeth819.

Shu, X., Lev-Ram, V., Deerinck, T. J., Qi, Y., Ramko, E. B., Davidson, M. W., Jin, Y., Ellisman, M. H., and Tsien, R. Y. A Genetically Encoded Tag for Correlated Light and Electron Microscopy of Intact Cells, Tissues, and Organisms. *PLoS Biology*, 9(4):e1001041, apr 2011. doi: 10.1371/journal.pbio.1001041.

Shvets, E., Bitsikas, V., Howard, G., Hansen, C. G., and Nichols, B. J. Dynamic caveolae exclude bulk membrane proteins and are required for sorting of excess glycosphingolipids. *Nature communications*, 6:6867, apr 2015. doi: 10.1038/ncomms7867.

Singer, S. J. Preparation of an electron-dense antibody conjugate. *Nature*, 183(4674):1523–4, may 1959.

Sochacki, K. A., Shtengel, G., van Engelenburg, S. B., Hess, H. F., and Taraska, J. W. Correlative super-resolution fluorescence and metal-replica transmission electron microscopy. *Nature Methods*, 11(3):305–308, jan 2014. doi: 10.1038/nmeth.2816.

Sochacki, K. A., Dickey, A. M., Strub, M.-P., and Taraska, J. W. Endocytic proteins are partitioned at the edge of the clathrin lattice in mammalian cells. *Nature cell biology*, 19(4):352–361, apr 2017. doi: 10.1038/ncb3498.

Sosinsky, G. E., Giepmans, B. N., Deerinck, T. J., Gaietta, G. M., and Ellisman, M. H. Markers for Correlated Light and Electron Microscopy. In *Methods in cell biology*, volume 79, pages 575–591. 2007. doi: 10.1016/S0091-679X(06)79023-9. URL http://www.ncbi.nlm.nih.gov/pubmed/17327175http://linkinghub.elsevier.com/retrieve/pii/S0091679X06790239.

Spencer, D. M., Wandless, T. J., Schreiber, S. L., and Crabtree, G. R. Controlling signal transduction with synthetic ligands. *Science (New York, N.Y.)*, 262(5136):1019–24, nov 1993.

Srinivasan, S., Dharmarajan, V., Reed, D. K., Griffin, P. R., and Schmid, S. L. Identification and function of conformational dynamics in the multidomain GTPase dynamin. *The EMBO Journal*, 35(4):443–457, feb 2016. doi: 10.15252/embj.201593477.

Strickland, D., Lin, Y., Wagner, E., Hope, C. M., Zayner, J., Antoniou, C., Sosnick, T. R., Weiss, E. L., and Glotzer, M. TULIPs: tunable, light-controlled interacting protein tags for cell biology. *Nature Methods*, 9(4):379–384, mar 2012. doi: 10.1038/nmeth.1904.

Tabuchi, M., Tanaka, N., Nishida-Kitayama, J., Ohno, H., and Kishi, F. Alternative Splicing Regulates the Subcellular Localization of Divalent Metal Transporter 1 Isoforms. *Molecular Biology of the Cell*, 13(12):4371–4387, dec 2002. doi: 10.1091/mbc.E02-03-0165.

Takizawa, T. and Robinson, J. M. FluoroNanogold Is a Bifunctional Immunoprobe for Correlative Fluorescence and Electron Microscopy. *Journal of Histochemistry & Cytochemistry*, 48(4):481–485, apr 2000. doi: 10.1177/002215540004800405.

Takizawa, T., Powell, R. D., Hainfeld, J. F., and Robinson, J. M. FluoroNanogold: an important probe for correlative microscopy. *Journal of Chemical Biology*, 8(4):129–142, oct 2015. doi: 10. 1007/s12154-015-0145-1.

Taslimi, A., Zoltowski, B., Miranda, J. G., Pathak, G. P., Hughes, R. M., and Tucker, C. L. Optimized second-generation CRY2-CIB dimerizers and photoactivatable Cre recombinase. *Nature chemical biology*, 12(6):425–30, 2016. doi: 10.1038/nchembio.2063.

Taylor, M. J., Perrais, D., and Merrifield, C. J. A high precision survey of the molecular dynamics of mammalian clathrin-mediated endocytosis. *PLoS biology*, 9(3):e1000604, mar 2011. doi: 10.1371/ journal.pbio.1000604.

Taylor, M. J., Lampe, M., and Merrifield, C. J. A Feedback Loop between Dynamin and Actin Recruitment during Clathrin-Mediated Endocytosis. *PLoS Biology*, 10(4):e1001302, apr 2012. doi: 10.1371/journal.pbio.1001302.

Tokuyasu, K. T. A technique for ultracryotomy of cell suspensions and tissues. *The Journal of cell biology*, 57(2):551–65, may 1973.

van Weering, J. R. T., Brown, E., Sharp, T. H., Mantell, J., Cullen, P. J., and Verkade, P. Intracellular membrane traffic at high resolution. *Methods in cell biology*, 96:619–48, 2010. doi: 10.1016/ S0091-679X(10)96026-3.

Wang, Q., Mercogliano, C. P., and Löwe, J. A ferritin-based label for cellular electron cryotomography. *Structure (London, England : 1993)*, 19(2):147–54, feb 2011. doi: 10.1016/j.str.2010.12.002.

Wang, W. and Malcolm, B. A. Two-stage PCR protocol allowing introduction of multiple mutations, deletions and insertions using QuikChange Site-Directed Mutagenesis. *BioTechniques*, 26(4):680–2, apr 1999.

Wilbur, J. D., Chen, C.-Y., Manalo, V., Hwang, P. K., Fletterick, R. J., and Brodsky, F. M. Actin Binding by Hip1 (Huntingtin-interacting Protein 1) and Hip1R (Hip1-related Protein) Is Regulated by Clathrin Light Chain. *Journal of Biological Chemistry*, 283(47):32870–32879, nov 2008. doi: 10.1074/jbc.M802863200.

Wilkinson, J., Di, X., Schönig, K., Buss, J. L., Kock, N. D., Cline, J. M., Saunders, T. L., Bujard, H., Torti, S. V., Torti, F. M., and Torti, F. M. Tissue-specific expression of ferritin H regulates cellular iron homoeostasis in vivo. *The Biochemical journal*, 395(3):501–7, may 2006. doi: 10.1042/BJ20060063.

Willox, A. K. and Royle, S. J. Stonin 2 is a major adaptor protein for clathrin-mediated synaptic vesicle retrieval. *Current biology : CB*, 22(15):1435–9, aug 2012. doi: 10.1016/j.cub.2012.05.048.

Wong, M. and Munro, S. The specificity of vesicle traffic to the Golgi is encoded in the golgin coiled-coil proteins. *Science*, 346(6209):1256898–1256898, oct 2014. doi: 10.1126/science.1256898.

Wood, L. A., Clarke, N. I., Sarkar, S., and Royle, S. J. Hot-wiring clathrin-mediated endocytosis in human cells. *bioRxiv*, 2016.

Wood, L. A., Larocque, G., Clarke, N. I., Sarkar, S., and Royle, S. J. New tools for 'hot-wiring' clathrin-mediated endocytosis with temporal and spatial precision. *The Journal of cell biology*, 216 (12):4351–4365, dec 2017. doi: 10.1083/jcb.201702188.

Zoncu, R., Perera, R. M., Sebastian, R., Nakatsu, F., Chen, H., Balla, T., Ayala, G., Toomre, D., and De Camilli, P. V. Loss of endocytic clathrin-coated pits upon acute depletion of phosphatidylinositol 4,5-bisphosphate. *Proceedings of the National Academy of Sciences of the United States of America*, 104(10):3793–8, mar 2007. doi: 10.1073/pnas.0611733104.

Appendix

5.1 Published Work

1) Auckland, P., **Clarke, N. I.,** Royle, S. J., McAinsh, A.D. Congressing kinetochores progressively load Ska complexes to prevent force-dependant detachment. Journal Cell Biology (2017): doi: 10.1083/jcb.201607096

Overview

In this work I used *correlated* light microscopy movies with serial block face scanning electron microscopy (SBF-SEM) to track congressing sister kinetochore pairs that were orientated and breathing. As sample processing for electron microscopy had been optimized to enable clear visualization of microtubules, we could demonstrate congressing pairs were bi-oriented at high resolution (Figure 1). We also discovered that aligned kinetochores have a 50% increase in bound microtubules compared to those that have not yet congressed (Figure 6). This data provided strong evidence that supported the model for how increasing pulling forces could be generated at kinetochores during congression.

2) Nixon, F.M., Honnor, T.R., **Clarke, N.I.,** Starling, G.P., Beckett, A.J., Johansen, A.M., Brettschneider, J.A., Prior, I.A., Royle, S. J. Microtubule organization within mitotic spindles revealed by serial block face scanning EM and image analysis. J Cell Sci (2017): doi: 10.1242/jcs.203877

Overview

For this paper, I used *correlative* light SBF-SEM to visualize microtubules within the mitotic spindle. Acquired datasets were segmented and rendered in 3D to provide information on microtubule organization. Specifically, my data contributed to the further quantification of the number of microtubules that terminate at kinetochores using this method (Figure 2). Furthermore, I provided 3D rendered images that show single microtubules could be resolved (Figure 2) and gave the idea for volumetric analysis of kinetochores (Figure 6).

3) Wood, L.A., Larocque, G., **Clarke, N. I.,** Sarkar, S., Royle, S. J. New tools for "hot-wiring" clathrin-mediated endocytosis with temporal and spatial precision. Journal Cell Biology (2017): doi: 10.1083/jcb.201702188

Overview

In this work I used *correlative* light-electron microscopy to locate synthetic endocytic vesicles made by this system. Live-cell uptake of fluoronanogold bound to CD8α was tracked following the chemical induction of endocytosis, cells where processed for electron microscopy and gold particles where located in resin sections (figure 2). This experiment provided key ultrastructural information about the created vesicles, 1) It supported and confirmed they were clathrin-coated and, 2) The synthetic vesicles where structurally different to normal clathrin-coated vesicles.